



Proceedings of
ISUD
2023

14th International Symposium on
Ultrasonic Doppler Methods for
Fluid Mechanics and Fluid Engineering

23-25 OCTOBER 2023
@ KOBE UNIVERSITY, KOBE, JAPAN

Proceedings of the 14th International Symposium on
Ultrasonic Doppler Methods for
Fluid Mechanics and Fluid Engineering (ISUD 2023)
23-25 October 2023, Kobe University, Kobe, Japan

Editors:

H. Murakawa, Kobe University

T. Ihara, Tokyo University of Marine Science and Technology

Y. Tasaka, Hokkaido University

Y. Oishi, Muroran Institute of Technology

Organizing Committee:

H. Murakawa, Chair, Kobe University

T. Ihara, Secretary, Tokyo University of Marine Science and Technology

N. Furuichi, Advanced Industrial Science and Technology

D. Ito, Kyoto University

T. Kawaguchi, Tokyo Institute of Technology

H. Kikura, Tokyo Institute of Technology

M. Motozawa, Shizuoka University

Y. Oishi, Muroran Institute of Technology

H.J. Park, Hokkaido University

K. Sugimoto, Kobe University

H. Takahashi, Tokyo Institute of Technology

Y. Tasaka, Hokkaido University

Y. Ueki, Osaka University

T. Yoshida, Advanced Industrial Science and Technology

N. Shoji, Muroran Institute of Technology

Scientific Committee:

- G. De Cesare, Chair, Ecole Polytechnique Federale de Lausanne (EPFL), Switzerland
- S. Eckert, Helmholtz-Zentrum Dresden-Rossendorf, Germany
- S. Fischer, Ubertone, France
- D. Hurther, Universite Grenoble Alpes, Laboratoire des Ecoulements Geophysiques et Industriels
- T. Ihara, Tokyo University of Marine Science and Technology, Japan
- H. Kikura, Tokyo Institute of Technology, Japan
- O. Mariette, Met-Flow, Switzerland
- H. Murakawa, Kobe University, Japan
- C. Rennie, University of Ottawa, Canada
- Y. Tasaka, Hokkaido University, Japan
- J. Wiklund, Incipientus Ultrasound Flow Technologies, Sweden
- J. Windhab, Swiss Federal Institute of Technology Zurich (ETH), Switzerland
- Y. Takeda, Hokkaido University, Japan

Copyright © 2023 by The Visualization Society of Japan
All rights reserved

Cover was designed by Taiki Yoshida

Proceedings of the 14th International Symposium on Ultrasonic Doppler Methods for
Fluid Mechanics and Fluid Engineering (ISUD 2023)

Table of Contents

Keynote lecture 1:

Development of low aspect ratio Taylor vortex bioreactor and flow analysis with ultrasonic measurement

H. Kawai and Y. Oishi 1

Rheologies & Non-Newtonian Fluid Flows:

Applications of ultrasonic spinning rheometry

Y. Tasaka, K. Ohie, H. Chin, A. Takano, T. Yoshida and Y. Murai 5

Flow prediction of complex fluids using rheometry coupled with ultrasonic velocity profiler

K. Ohie, T. Yoshida, Y. Tasaka and Y. Murai 9

Evaluation of viscous characteristics of Newtonian and non-Newtonian fluids by falling head flow tests with an ultrasonic velocity profiler

R. Obinata, S. Nomura, K. Tani, M. Kyoji and T. Ihara 13

Advanced Measurements & Fundamental Flows:

Transient flowrate measurement and evaluation for dynamic response of flowmeters

N. Furuichi and T. Yoshida 17

The OpenUVP is ready to launch eUVP

Y. Takeda, N. Shoji, H. Kikura and E. Windhab 21

Analysis of flow behavior and evaluation of agitation performance by impeller using UVP

H. Okumura, K. Takasaka, N. Ohmura and A. Ishihata 23

Measurement of silica-sand behavior around rotating square cylinder in a circular container by ultrasound velocity profiler	
Y. Oishi, S. Osanai, H. Kawai, H. Kikura and K. Kusumoto	27
Investigation of flow characteristics induced by vertical heated rod using ultrasound velocity profiler	
T. T. Duong, C. T. Tran, T. T. Nguyen and H. Kikura	31
Nonlinear large-scale flow transition in a processing cylinder and its potential for hydromagnetic dynamo action	
T. Gundrum, V. Kumar, F. Pizzi, A. Giesecke, F. Stefani and S. Eckert	35

Novel Methodologies:

Monitoring of Liquid-solid two-phase pipe flow using ultrasonic pulses	
H. J. Park, T. Hayashi, D. Yoon, Y. Tasaka, Y. Murai, S. Takano and S. Masanobu	39
A novel idea of methodology for evaluating spatial propagation characteristics of ultrasound pulse-echo	
T. Yoshida, S. Wada and N. Furuichi	43
Implementation of autocorrelation algorithm in VHDL for UVP instrumentation	
I. F. Z. Schmidt, F. R. Coutinho, A. L. Stakowian, C. Y. Ofuchi, M. J. da Silva, F. Neves Jr and R. E. M. Morales	47
Investigation of the influence of the background ocean current on flow measurements using the UVP method	
S. Ueno and T. Ihara	51
Fundamental study of superimposed image flow visualization using UVP	
Y. Namiki, T. Nakada, N. Shoji, H. Takahashi and H. Kikura	55

Integration of time-resolved sensors and line measurements to improve the time resolution of the ultrasonic velocity profiler based on data-driven technique	
N. Tiwari	59

Keynote lecture 2:

Coupling of in-line UVPPD rheometry and USDMA for process control in polymorph crystallization processing of chocolate confectionery masses	
E. Windhab, K. Mishra and L. Grob	63

Multiphase Flows 1:

Classification of flow regimes in bubble column using the integration of ultrasound and KNN algorithm	
W. Wongsaroj, J. Pulsawat, N. Shoji, N. Thong-Un, W. Treenusorn and H. Kikura	67
Effect of transverse magnetic field on rising bubble behavior in gallium eutectic alloy	
S. Maeda, H. Murakawa, K. Sugimoto and S. Eckert	71
Measurements of bubble rising velocity using ultrasonic tomography	
H. Murakawa, Y. Kubo, S. Maeda and K. Sugimoto	75

Multiphase Flows 2:

Ultrasound pulse measurement of air-lift multiphase pipe flow in an inclined pipe	
Y. Murai, T. Hayashi, D. Yoon, H. J. Park, Y. Tasaka, S. Takano and S. Masanobu	79
Measurement of solid-gas-liquid three-phase flow using pulsed ultrasound	
N. Shoji, H. Kikura, H. Takahashi, K. Teramoto and H. Kawai	83

Study on ultrasonic echo measurement for vertical pipe gas-liquid multiphase flow containing large bubbles

R. Obana, I. Watanabe, K. Maehara, K. Shimizu and S. Takagi 87

Environmental Flows:

Influence of the shear stress on fine sediment exchanges with the substrate using UVP measurements

R. Dubuis and G. De Cesare91

Characterization of thruster-induced turbulence for fine sediment suspension

M. Marshall, A. Amini, G. De Cesare and A. L. Stakowian95

Physical modeling and UVP monitoring yield an efficient protection of a lake reedbed from erosion

V. Zsolt, A. Nicolas, W. Florent, G. Karine, J. Amandine and V. André99

Sediment dynamics by bistatic ultrasonic Doppler under real waves

N. Fritsch, G. Fromant, F. Floc'h, S. Fischer, Y. Cobac, C. Poitou, C. Prunier, S. Bertin, E. Augereau, M. Jaud and J. Tanrin 103

Rock-flow cell parameters evaluation using ultrasound Doppler velocimetry

A. L. Stakowian, G. N. D. Dextre, L. F. Botton, E. N. Dos Santos, F. R. Coutinho, C. Y. Ofuchi, M. J. Da Silva, G. De Cesare, R. E. M. Morales and O. Mariette 107

Ultrasonic sediment flux profiling with ACVP technology: application to sediment-laden boundary layer flows

D. Hurther and G. De Cesare 111

Special Lecture:

Nondestructive testing and condition monitoring techniques based on multi-wavelength infrared measurements

T. Sakagami 115

Author Index:

A

- Amandine, J., 99
Amini, A., 95
André, V., 99
Augereau, E., 103

B

- Bertin, S., 103
Botton, L.F., 107

C

- Chin, H., 5
Cobac, Y., 103
Coutinho, F.R., 47, 107

D

- Da Silva, M.J., 47, 107
De Cesare, G., 91, 95, 107, 111
Dextre, G.N.D., 107
Dos Santos, E.N., 107
Dubuis, R., 91
Duong, T.T., 31

E

- Eckert, S., 35, 71

F

- Fischer, S., 103
Floc'h, F., 103
Florent, W., 99
Fritsch, N., 103
Fromant, G., 103
Furuichi, N., 17, 43

G

- Giesecke, A., 35
Grob, L., 63
Gundrum, T., 35

H

- Hayashi, T., 39, 79
Hurther, D., 111

I

- Ihara, T., 13, 51
Ishihata, A., 23

J

- Jaud, M., 103

K

- Karine, G., 99
Kawai, H., 1, 27, 83
Kikura, H., 21, 27, 31, 55, 67, 83
Kubo, Y., 75
Kumar, V., 35
Kusumoto, K., 27
Kyoi, M., 13

M

- Maeda, S., 71, 75
Maehara, K., 87
Marianne, O., 107
Marshall, M., 95
Masanobu, S., 39, 79
Mishra, K., 63
Morales, R.E.M., 47, 107

Murai, Y., 5, 9, 39, 79
Murakawa, H., 71, 75

N

Nakada, T., 55
Namiki, Y., 55
Neves Jr, F., 47
Nguyen, T.T., 31
Nicolas, A., 99
Nomura, S., 13

O

Obana, R., 87
Obinata, R., 13
Ofuchi, C.Y., 47, 107
Ohie, K., 5, 9
Ohmura, N., 23
Oishi, Y., 1, 27
Okumura, H., 23
Osanai, S., 27

P

Park, H.J., 39, 79
Pizzi, F., 35
Poitou, C., 103
Prunier, C., 103
Pulsawat, J., 67

S

Sakagami, T., 115
Schmidt, I.F.Z., 47
Shimizu, K., 87
Shoji, N., 21, 55, 67, 83
Stakowian, A.L., 47, 95, 107
Stefani, F., 35
Sugimoto, K., 71, 75

T

Takagi, S., 87
Takahashi, H., 55, 83
Takano, A., 5
Takano, S., 39, 79
Takasaka, K., 23
Takeda, Y., 21
Tani, K., 13
Tanrin, J., 103
Tasaka, Y., 5, 9, 39, 79
Teramoto, K., 83
Thong-Un, N., 67
Tiwari, N., 59
Tran, C.T., 31
Treenusorn, W., 67

U

Ueno, S., 51

W

Wada, S., 43
Watanabe, I., 87
Windhab, E., 21, 63
Wongsaroj, W., 67

Y

Yoon, D., 39, 79
Yoshida, T., 5, 9, 17, 43

Z


Zsolt, V., 99

Technical Program of ISUD 2023

Oct. 23 Mon. (Day-1)

9:00	Conference Registration
10:00	Opening Session; Prof. H. Murakawa
10:20	Keynote Lecture 1, Chair: H. Kikura
	Development of low aspect ratio Taylor vortex bioreactor and flow analysis with ultrasonic measurement Prof. H. Kawai and Y. Oishi
11:00	Rheologies & Non-Newtonian Fluid Flows, Chair: H. Murakawa
	Applications of ultrasonic spinning rheometry Y. Tasaka, K. Ohie, H. Chin, A. Takano, T. Yoshida and Y. Murai Flow prediction of complex fluids using rheometry coupled with ultrasonic velocity profiler K. Ohie*, T. Yoshida, Y. Tasaka and Y. Murai Evaluation of viscous characteristics of Newtonian and non-Newtonian fluids by falling head flow tests with an ultrasonic velocity profiler R. Obinata*, S. Nomura, K. Tani, M. Kyoji and T. Ihara
12:00	Lunch Break
13:20	Advanced Measurements & Fundamental Flows, Chair: H. Kikura & Y. Tasaka
	Transient flowrate measurement and evaluation for dynamic response of flowmeters N. Furuichi and T. Yoshida The OpenUVP is ready to launch eUVP Y. Takeda, N. Shoji, H. Kikura and E. Windhab Analysis of flow behavior and evaluation of agitation performance by impeller using UVP H. Okumura*, K. Takasaka, N. Ohmura and A. Ishihata Measurement of silica-sand behavior around rotating square cylinder in a circular container by ultrasound velocity profiler Y. Oishi, S. Osanai, H. Kawai, H. Kikura and K. Kusumoto Investigation of flow characteristics induced by vertical heated rod using ultrasound velocity profiler T. T. Duong, C. T. Tran, T. T. Nguyen and H. Kikura Nonlinear large-scale flow transition in a precessing cylinder and its potential for hydromagnetic dynamo action T. Gundrum, V. Kumar, P. Federico, A. Giesecke, F. Stefani and S. Eckert
15:20	Coffee Break
15:50	Novel Methodologies, Chair: T. Ihara & H. J. Park
	Monitoring of Liquid-solid two-phase pipe flow using ultrasonic pulses H. J. Park, T. Hayashi, D. Yoon, Y. Tasaka, Y. Murai, S. Takano and S. Masanobu A novel idea of methodology for evaluating spatial propagation characteristics of ultrasound pulse-echo T. Yoshida, S. Wada and N. Furuichi Implementation of autocorrelation algorithm in VHDL for UVP instrumentation I. F. Z. Schmidt, F. R. Coutinho, A. L. Stakowian, C. Y. Ofuchi, M. J. da Silva, F. Neves Jr and R. E. M. Morales Investigation of the influence of the background ocean current on flow measurements using the UVP method S. Ueno* and T. Ihara Fundamental study of superimposed image flow visualization using UVP Y. Namiki*, T. Nakada, N. Shoji, H. Takahashi and H. Kikura Integration of time-resolved sensors and line measurements to improve the time resolution of the ultrasonic velocity profiler based on data-driven technique N. Tiwari
18:00	Welcome Reception
20:00	

Oct. 24 Tue. (Day-2)

9:30	Conference Registration
10:00	Keynote Lecture 2 , Chair: Y. Takeda Coupling of in-line UVPPD rheometry and USDMA for process control in polymorph crystallization processing of chocolate confectionery masses <u>Prof. E. Windhab</u> , K. Mishra and L. Grob
10:40	Short Break
10:50	Multiphase Flows 1 , Chair: Y. Murai Classification of flow regimes in bubble column using the integration of ultrasound and KNN algorithm <u>W. Wongsaroj</u> , J. Pulsawat, N. Shoji, N. Thong-Un, W. Treenusorn and H. Kikura Effect of transverse magnetic field on rising bubble behavior in gallium eutectic alloy <u>S. Maeda*</u> , H. Murakawa, K. Sugimoto and S. Eckert Measurements of bubble rising velocity using ultrasonic tomography <u>H. Murakawa</u> , Y. Kubo, S. Maeda and K. Sugimoto
11:50	Lunch Break
13:10	Multiphase Flows 2 , Chair: H. Murakawa Ultrasound pulse measurement of air-lift multiphase pipe flow in an inclined pipe <u>Y. Murai</u> , T. Hayashi, D. Yoon, H. J. Park, Y. Tasaka, S. Takano and S. Masanobu Measurement of solid-gas-liquid three-phase flow using pulsed ultrasound <u>N. Shoji</u> , H. Kikura, H. Takahashi, K. Teramoto and H. Kawai Study on ultrasonic echo measurement for vertical pipe gas-liquid multiphase flow containing large bubbles <u>R. Obana*</u> , I. Watanabe, K. Maehara, K. Shimizu and S. Takagi
	Excursion & Met-Flow Dinner 

Oct. 25 Wed. (Day-3)

9:30	Conference Registration
10:00	Environmental Flows , Chair: G. De Cesare & S. Fischer Influence of the shear stress on fine sediment exchanges with the substrate using UVP measurements R. Dubuis and <u>G. De Cesare</u> Characterization of Thruster-Induced Turbulence for Fine Sediment Suspension M. Marshall, A. Amini, <u>G. De Cesare</u> and A. L. Stakowian Physical modeling and UVP monitoring yield an efficient protection of a lake reedbed from erosion <u>Z. Vecsernyes</u> , N. Andreini, F. Wohlwend, K. Gobat, A. Jaeger and A. Venturi Sediment dynamics by bistatic ultrasonic Doppler under real waves N. Fritsch, G. Fromant, F. Floc'H, <u>S. Fischer</u> , Y. Cobac, C. Poitou, C. Prunier, S. Bertin, E. Augereau, M. Jaud and J. Tanrin Rock-flow cell parameters evaluation using ultrasound Doppler velocimetry A. L. Stakowian, G. N. D. Dextre, L. F. Botton, E. N. Dos Santos, <u>F. R. Coutinho</u> , C. Y. Ofuchi, M. J. Da Silva, G. De Cesare, R. E. M. Morales, O. Mariette Ultrasonic sediment flux profiling with ACVP technology: application to sediment-laden boundary layer flows D. Hurther and <u>G. De Cesare</u>
12:00	Conference Photo
12:20	Lunch Break
13:40	Special Lecture , Chair: H. Murakawa Nondestructive testing and condition monitoring techniques based on multi-wavelength infrared measurements <u>Prof. T. Sakagami</u>
14:20	Closing Session , Prof. H. Murakawa
	Lab. Tour

Presenters are underlined in the program and names indicated by asterisk are nominated to Ubertone Student Award.

Supported by **UBERTONE**

Evaluation of viscous characteristics of Newtonian and non-Newtonian fluids by falling head flow tests with an ultrasonic velocity profiler

Ryou Obinata¹, Shun Nomura¹, Kazuo Tani¹, Minori Kyoj¹, Tomonori Ihara²

¹ Dep. of Marine Resources and Energy, Tokyo University of Marine Science and Technology, 4-5-7 Konan, Minato-ku, Tokyo 108-8477, Japan

² Dep. of Marine Electronics and Mechanical Engineering, Tokyo University of Marine Science and Technology, 2-1-6 Etchujima, Koto-ku, Tokyo 135-8533, Japan

The purpose of this study is to investigate the flow velocity profile in the pipe of falling head flow test (FHFT) with an ultrasonic velocity profiler (UVP). FHFT was proposed to evaluate the viscous characteristics of Bingham fluids. Its application was extended to varieties of non-Newtonian fluids. In the FHFT, the viscosity parameters such as the plastic viscosity and the yield stress can be derived by measuring the falling head process in the apparatus composed of the vertical and horizontal pipes. If the yield stress, $\tau_y > 0$, a plug flow is theoretically considered to develop in the central region of the flow. In the experiment, UVP was placed along the horizontal pipe to measure the velocity profile. Two FHFTs were conducted using Glycerin as the Newtonian fluid, and CMC solution as the non-Newtonian fluid, respectively. By the UVP measurement, a parabolic profile was observed in Glycerin, while a semi-parabolic profile representing a plug flow in the middle was observed in CMC solution. The velocity profiles postulated from the viscosity characteristics obtained by FHFT were consistent with those measured by UVP. Thus, this FHFT is applicable to evaluate the viscous characteristics of both Newtonian and non-Newtonian fluids.

Keywords: Flow test, Viscous characteristic, Viscosity measurement, Pipe flow

1. Introduction

Marine mineral resources such as polymetallic nodules exist on the seabed around Japan. To lift up ores of these mineral resources from the seabed to the sea surface, Tani et al. [1] proposed to use a viscous fluid with yield stress as a carrier material (CM). To study the lifting efficiency of the relevant systems, it is important to evaluate the viscous characteristics of CMs (i.e., the relationship between the shear stress, τ , and the shear rate, $\dot{\gamma}$). At present, rotational viscometers such as the B type viscometer are commonly used for viscosity measurements. However, they are not suitable for fluids containing sand particles and can only measure the apparent relationship between shear stress and shear rate for non-Newtonian fluids. To overcome these problems, Kyoj et al. [2] proposed the falling head flow test (FHFT) as a novel method to measure the viscosity characteristics of both Newtonian and non-Newtonian fluids.

In this study, FHFTs were conducted using Glycerin as a Newtonian fluid and CMC solution as a non-Newtonian fluid. The applicability of this test method was examined through the investigation of the flow velocity profile in the pipe of FHFT with an ultrasonic velocity profiler (UVP).

2. Method of Falling Head Flow Test

2.1 Principle of falling head flow test

Figure 1 shows the principle of FHFT and the laminar flow of a non-Newtonian fluid in the pipe. In this test, the fluid (density ρ) flows down in the pipe (radius R). This pipe is composed of the vertical and horizontal sections with the height, h , and the length, L , respectively. The viscous characteristics are obtained by optically analyzing the

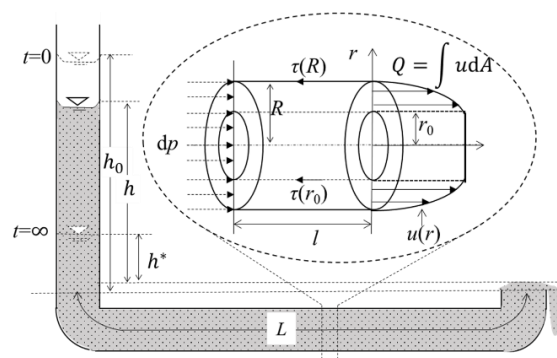


Figure 1: Principle of the falling head flow test.

change of the elevation difference, h , with time, t . The initial condition is set as $h = h_0$ at $t = 0$.

Eq.1 shows the equilibrium condition for the small section with the length, l , in the pipe. Eq.2 shows the relationship between the shear stress τ and the shear rate $\dot{\gamma}$ of a non-Newtonian fluid by Herschel-Bulkley model which express as shear thinning and yield stress effectively in the pipe where k is the consistency index, n is the flow index, and τ_y is the yield stress. Considering $dp = \rho gh$ and $l = L + h$, the mean velocity U was obtained as Eq.3 using the ratio of plug flow radius r_0 to R as Eq.4 from Eq.1 and Eq.2. Each parameter to present U can be defined from the test setting except k , n , and the terminal head loss, h^* , at $t = \infty$. τ_y is derived by Eq.5. Eq.6 defines the theoretical head loss $h_{the(t+dt)}$ at $t = t + dt$ with $U_{obs(t)}$ derived from $h_{obs(t)}$ obtained through FHFT. Then, as Eq.7, the appropriate combination of k , n and h^* are derived by minimizing the sum of the squares of the difference between $h_{obs(t)}$ and $h_{the(t)}$.

$$\pi r^2 dp = 2\pi r l \tau_{(r)} \quad (1)$$

$$\tau_{(r)} = \tau_y + k\dot{\gamma}_{(r)}^n \quad (2)$$

$$U = \frac{Q}{\pi R^2} \quad (3)$$

$$= \left(\frac{R\rho g}{2k} \frac{h}{L+h} \right)^{\frac{1}{n}} \frac{R}{1+\frac{1}{n}} \left(1 - \frac{r_0}{R} \right)^{1+\frac{1}{n}}$$

$$\left\{ 1 - \frac{2}{2+\frac{1}{n}} \left(1 - \frac{r_0}{R} \right) + \frac{2}{\left(2 + \frac{1}{n} \right) \left(3 + \frac{1}{n} \right)} \left(1 - \frac{r_0}{R} \right)^2 \right\}$$

$$\frac{r_0}{R} = \left(\frac{h^*}{L+h^*} \right) \left(\frac{L+h}{h} \right) \quad (4)$$

$$\tau_y = \frac{\rho g h^*}{L+h^*} \quad (5)$$

$$h_{the(t+dt)} = h_{the(t)} - U_{obs(t)} dt \quad (6)$$

$$h_{(t=0)} = h_0$$

$$\sum_{t=0}^t \{ h_{obs(t)} - h_{the(t)}(k, n, h^*) \}^2 = \min. \quad (7)$$

2.2 Setting of FHFTS

Two kinds of fluids were used in FHFT; Glycerin (Glycerol $\geq 95.0\%$, Hayashi Pure Chemical Ind., Ltd) and CMC (Carboxymethyl Cellulose, CMC HP-80, Daicel Miraizu., Ltd) solution which was diluted with water to the mass concentration of 1.0%, respectively. In addition, to improve the visibility of the flow, food coloring (Food coloring red, KENIS Co., Ltd) was mixed with not higher than 0.01% solution mass.

Figure 2 shows the experimental apparatus. Table 1 shows the densities of fluids and the test conditions of the experimental apparatus. R was 20.4 mm. The initial heads, h_0 , and the length of the horizontal section, L , were determined so that the liquid level at the downstream end was quasi-static and stable. The temperature of fluids was from 20.0 °C to 21.0 °C. Here, h was measured from the recorded movie through the image analysis every 0.1 s for Glycerin and 1.0 s for CMC 1%, respectively.

Table 1: Condition of FHFT.

Fluid	ρ (Mg/m ³)	h_0 (m)	L (m)
Glycerin	1.220	0.879	2.360
CMC 1.0%	1.020	1.835	1.330

2.3 Setting of UVP

Figure 2 and Figure 3 show the experimental apparatus and concept of UVP measurement, respectively. A laboratory built UVP setup was used, which consists of a pulser/receiver, A/D converter and signal processing software. The UVP was fixed with the jig and installed in

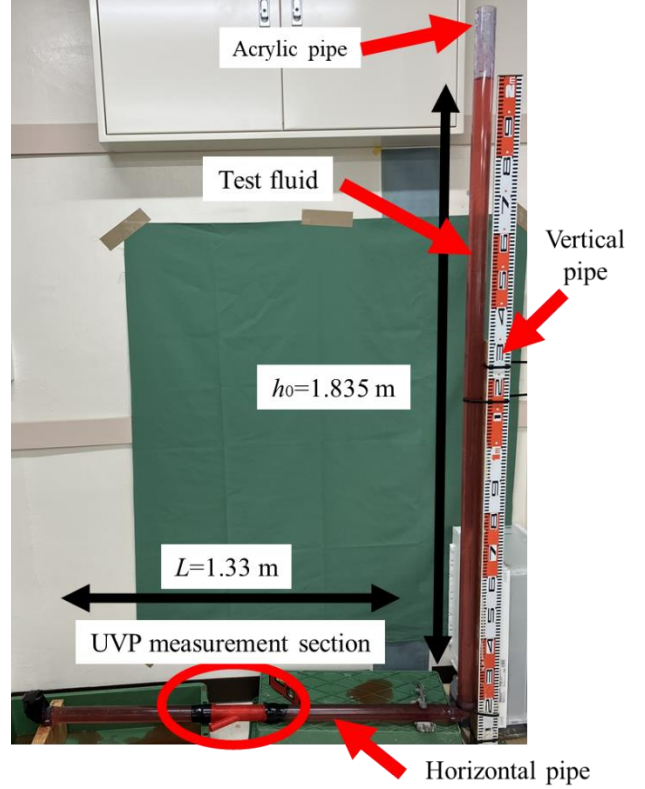


Figure 2: Experimental apparatus.

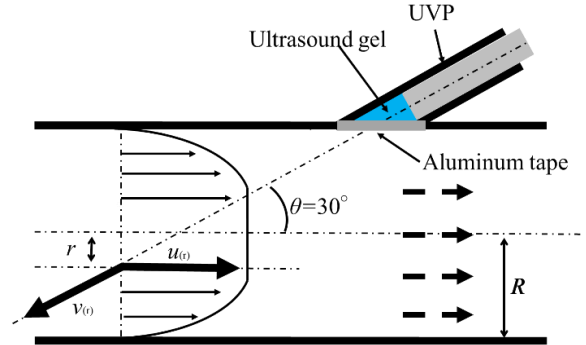


Figure 3: Concept of UVP measurement.

the middle section of the horizontal pipe. The inclination angle θ of ultrasound beam was set 30 degrees from the flow direction. The velocity profile $v_{(r)}$ in the ultrasonic beam direction is transformed into the flow direction $u_{(r)}$ by Eq.8. Table 2 shows the parameters of UVP measurement. The measurements were conducted with the transducer whose diameter is 16mm. The emitting frequency is 1 MHz.

$$u_{(r)} = -\frac{v_{(r)}}{\cos 30^\circ} \quad (8)$$

Table 2: Parameters of UVP measurement.

Parameters	Glycerin	CMC
Pulse repetition frequency PRF (Hz)	800	100
Sound velocity of the fluid (m/s)	2000	1710
Sampling rate (Hz)	10	5

3. Test Results and Discussions

Figure 4 shows h - t relationships and mean velocities $U = dh/dt$ of Glycerin by FHFT at the representative points, G1: $t = 2.0$ s, G2: $t = 5.0$ s and G3: $t = 10.0$ s. Figure 5 shows those of CMC 1% at the representative points, C1: $t = 10$ s, C2: $t = 70$ s, C3: $t = 150$ s. In the case of Glycerin, the h falls down rapidly, $\Delta h > 0.7$ m for $t < 10$ s, whereas in CMC, it falls slowly even after $t = 1000$ s.

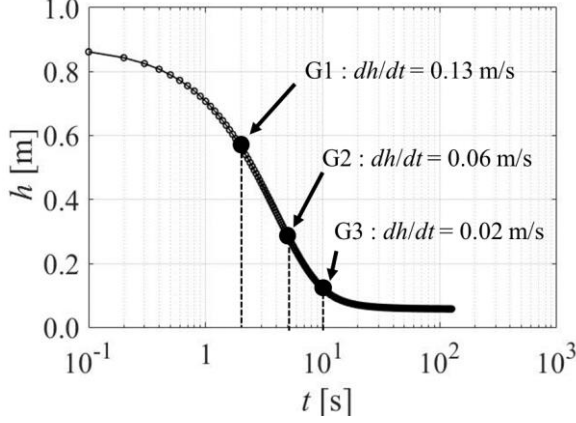


Figure 4: h - t relationship and U of Glycerin at G1, G2, G3.

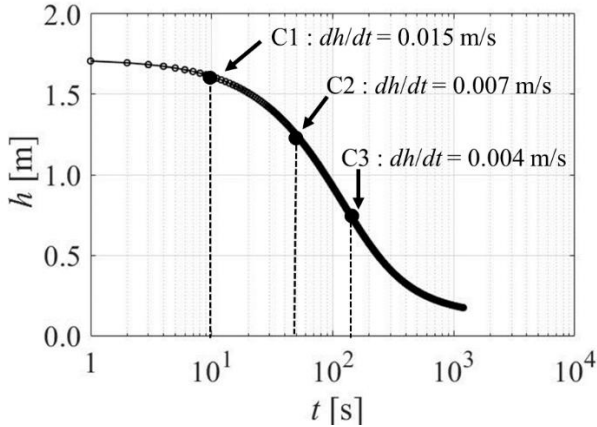


Figure 5: h - t relationship and U of CMC 1% at C1, C2, C3.

Table 3 shows the viscosity parameters, k , n , and τ_y , measured by FHFT and B type viscometer (DV-II+pro-LV, Brookfield). It should be noted that τ_y could not be obtained by the B type viscometer, thereby shown as NA. In Herschel-Bulkley equation (Eq.2), it's well known that $n = 1$ and $\tau_y = 0$ for a Newtonian fluid such as Glycerin, and $n < 1$ for a pseudoplastic fluid such as CMC solution. It is found that the FHFT can evaluate reasonable values of n for both Newtonian and non-Newtonian fluids.

Using these parameters in Table 3, the velocity profiles were assumed by Eq.9 and Eq.10 as well by Benslimane A. et al. [3]. In the pipe, the laminar flow area ($\tau_{(r)} > \tau_y$) and the plug flow area ($0 < \tau_{(r)} \leq \tau_y$) are presented in Eq.9 and Eq.10, respectively. Figure 6 and Figure 7 show non-dimensional velocity profiles of Glycerin and CMC at the representative points, respectively. Those profiles were obtained according to the sampling rate in Table 2.

Table 3: Comparison of viscosity parameters by FHFT and B

Viscosity parameter	Glycerin		CMC 1%	
	FHFT	B type	FHFT	B type
k [Pa·s]	0.79	0.80	26	26
n [-]	1.0	1.2	0.44	0.29
τ_y [Pa]	3.1	NA	6.4	NA

$$u_{(r)} = \frac{R}{\tau_{(r)} k^{\frac{1}{n}} \frac{1}{n} + 1} \left\{ \begin{aligned} &(\tau_{(r)} > \tau_y) \\ &\left(\tau_{(r)} - \tau_y \right)^{\frac{1}{n}+1} \\ &- \left(\tau_{(r)} \frac{r}{R} - \tau_y \right)^{\frac{1}{n}+1} \end{aligned} \right\} \quad (9)$$

$$(0 < \tau_{(r)} \leq \tau_y) \quad (10)$$

$$u_{(r)} = \frac{R}{\tau_{(r)} k^{\frac{1}{n}} \frac{1}{n} + 1} \left(\tau_{(r)} - \tau_y \right)^{\frac{1}{n}+1}$$

In those figures, a comparison was made with the predicted profile by FHFT and the fitted profile for measured data by UVP using the least squares method with the range of $-1 \leq r/R \leq 0.7$ as assuming the velocity of 0 m/s on the pipe wall. From Figure 6, it was found that the profiles obtained by UVP of Glycerin present parabolic profiles and are consistent with the predicted profiles by FHFT for high and middle flow velocities (referring to G1 and G2). While, it is less consistent for the lowest flow velocity when the plug flow develops (referring to G3). This means that the dh/dt was larger than the predicted profiles by FHFT compared with G1 and G2. It suggests that the fluid was slipping on the pipe wall. At low velocities, the assumed boundary conditions at the pipe wall might be inconsistent due to fluid flow does not have enough shear stress for deformation at the pipe wall.

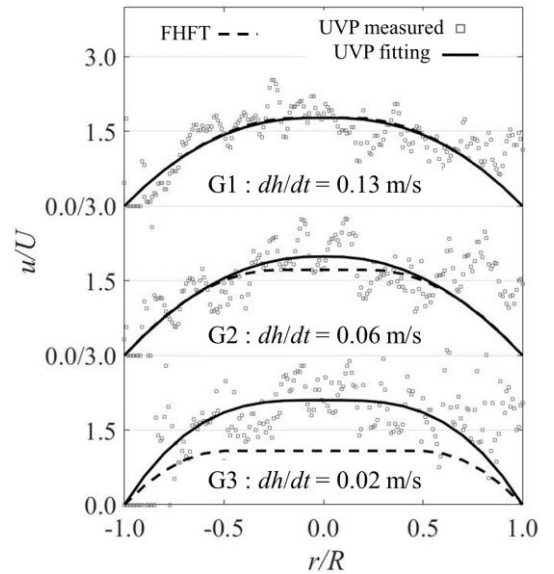


Figure 6: Velocity profiles of Glycerin at G1, G2, and G3.

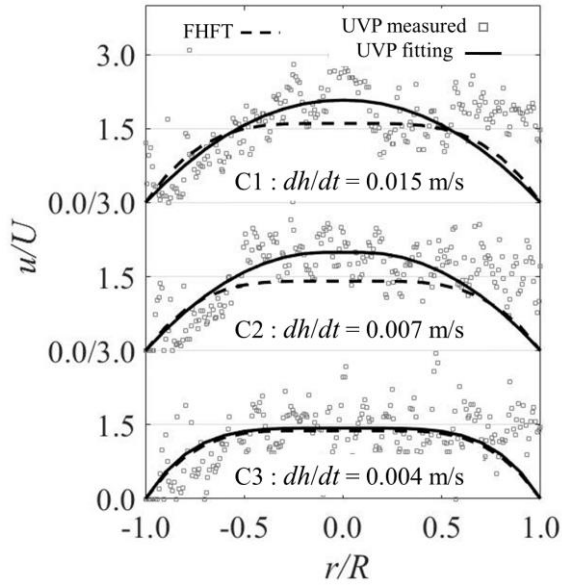


Figure 7: Velocity profiles of CMC 1% at C1, C2, and C3.

From Figure 7, it is concluded that the velocity profiles measured by both methods are consistent with each other. Those obtained by UVP show that the plug flow presents around the central region in the pipe (referring to C2 and C3). However, the difference between the measured profiles by UVP and the predicted profiles by FHFT is larger than that for Glycerin around $r/R = 0$. This is because CMC solutions have thickening structures made by polysaccharides in the fluid. As a result, it presents more non-linear characteristics to theoretical flow than Newtonian fluid.

Table 4: Comparison of viscosity parameters of Glycerin and CMC 1% by FHFT and UVP

Glycerin Viscosity parameter	FHFT	UVP		
		G1	G2	G3
k [Pa·s]	0.79	1.6	1.3	2.2
n [-]	1.00	0.81	0.91	0.55
τ_y [Pa]	3.1	1.0	0.4	0.4
CMC 1% Viscosity parameter	FHFT	UVP		
		C1	C2	C3
k [Pa·s]	26	18.1	25.5	28.0
n [-]	0.44	0.99	1.00	0.30
τ_y [Pa]	6.4	0.60	4.10	0.60

In Table 4, a comparison is made between the viscosity parameters obtained by FHFT and those obtained by UVP. For Glycerin, the parameters obtained by UVP exhibit Newtonian fluid characteristics at G1 and G2. Additionally, at C3, where the plug flow was most developed, the parameters obtained by UVP represent non-Newtonian fluid characteristics similar to those obtained by FHFT. However, the combination of n , k , and τ_y affect each other even the shape of the velocity profiles. As a result, it is found that a more appropriate method and reasonable solution to determine the parameter in Eq.2 is needed. Furthermore, influence of slip at the pipe wall may induce inconsistency of FHFT and UVP profile. Thereby, we need the confirmation of the boundary condition and more detailed observations near the pipe wall.

4. Conclusions

By FHFT, the viscosity parameters were measured of Glycerin and CMC 1% solutions, respectively. In these tests, velocity profiles in the pipe were measured using UVP at the same time to study the applicability of the FHFTs.

The results demonstrate that the velocity profiles derived from the viscosity parameters obtained through FHFT agreed well with those fitted from UVP measurement. Thus, it's justified to conclude that FHFT test is applicable to evaluate viscous characteristics of both Newtonian and non-Newtonian fluids.

References

- [1] Tani K., *et al.*: Method and devices for lifting valuable seafloor materials using carrier material, Japan Patent No. 6570000, (2018). (in Japanese)
- [2] Kyoji M., *et al.*: Falling head flow test to study pipe flow and viscous characteristics of carrier materials used for ore lifting from deep seafloor. ICPMG. pp.538-541, (2022).
- [3] Benslimane A., *et al.*: Laminar and turbulent pipe flow of bentonite solutions. Journal of Petroleum Science and Engineering, (2015).

The OpenUVP is ready to launch eUVP

Yasushi Takeda¹, Naruki Shoji^{2,3}, Hiroshige Kikura², and Erich J. Windhab⁴

¹ Hokkaido University, Japan

² Tokyo Institute of Technology, Japan

³ Muroran Institute of Technology, Japan

⁴ Federal Institute of Technology, Zurich, Switzerland

OpenUVP is preparing for a set of unit to be used for educational purpose and named *eUVP*. It consists of hardware-Pulsar/Receiver and software eUVP-TIT. As a whole set of educational equipment, two sets of desktop flow stand are prepared; pipe flow and a short column Taylor Couette Flow.

Keywords: OpenUVP, eUVP, desktop flow of Pipe flow and TCF.

1. Introduction

Activity of OpenUVP is progressed to prepare for the educational version of UVP – eUVP. Targeting its use in higher schools as technical school or engineering school on university level, simplicity of hardware and its use with standard PC is the most important factor for developing the system. Hardware to be developed consists of Pulsar /Receiver with ADC integrated and to be combined with PC. It was also designed to facilitate it for demonstration in the class room, not only in the flow lab, so that two standard flow configurations are prepared to be used on the class room table.

2. eUVP construction

2.1 Hardware – Pulsar/Receiver

Only hardware except transducers is a box with all necessary electronics integrated to work as UVP. It has two channels of Pulsar-Receiver system with ADC integrated. The system can be used for A and B mode operation of echo signal application. Raw echo signals are sampled and transferred to external PC with USB line.



2.2 Specification

The specification of the Pulsar/Receiver electronics is listed in the table below.

It can be operated with basic frequency from 0.5 to 10MHz.

All parameters can be controlled by the eUVP software externally. It has external triggering capability to be synchronized with PRF signal.

Parameter	Detail
Power source	100 to 230 VAC
Communication	USB 3.0
Interface	USB 3.0 (PC – TIT-eUVP) Transducer (BNC) × 2 CH. Echo signal (BNC, 2 V _{pp}) × 2 CH. PRF trigger signal (BNC, 5 V TTL)
Number of transducer connection	2
Pulse voltage	150 V _{pp}
Basic frequency	0.5 to 10 MHz (square burst wave)
Number of cycles	Up to 10
PRF	Up to 10 kHz
Echo signal gain	0 dB ~ 50 dB
Signal bandwidth	30 kHz to 12 MHz
A/D sampling speed / resolution	50 MS/s / 12 bit

2.3 Software – eUVP

eUVP software is prepared for using the PR exclusively for educational purpose using OpenUVP concept. It has two parameter panels – Parameter control panel and Measurement panel and three operational panels – Echo

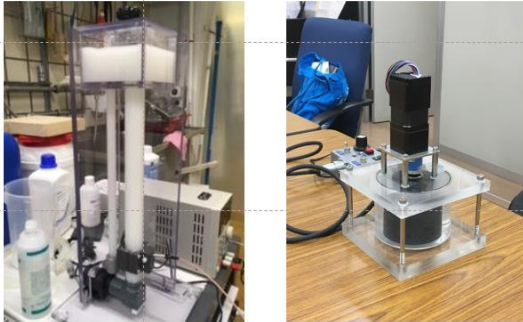


panel, Velocity profile panel and Color density panel – which are used to demonstrate a working style of UVP. Data set is stored in CSV format for reviewing and

analyzing measured results using any of external standard spread sheet applications.

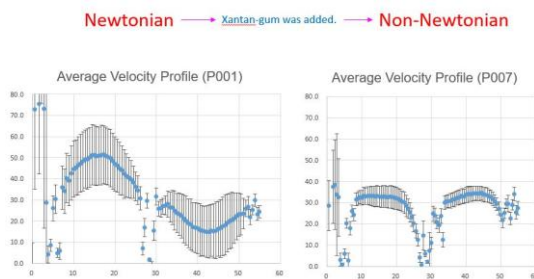
2.4 Desktop Flow models

In order for the apparatus to be used in normal class rooms, two sets of tabletop flow configurations are prepared – pipe flow and short column Taylor column.



2.4.1 Pipe flow

As UVP measures instantaneous velocity profile, pipe flow can be simple without flow development as is needed for standard pipe flow experiment. It consists of two straight pipe lines, one for measurement and another for return flow. The upper reservoir is easy to access to modify flow characteristics. By adding any viscous fluid a flow of Newtonian and non-Newtonian flow behavior can be tested. It can obviously catch data set for time averaged velocity profile to compare it with theory. By varying pump speed it is possible to show a change of velocity profile from laminar to turbulence.

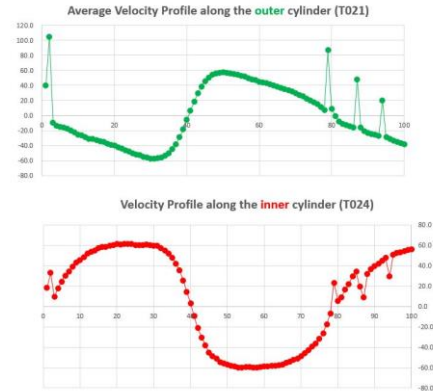


2.4.2 TCF

A short column Taylor Couette Flow (rotating double cylinder with only inner cylinder rotation) is prepared with aspect ratio of 2. This configuration is adequate to show that the flow velocity is vector. Measurement of z-component of vertical velocity as a function of z; $V_z(z,t)$, at the inner and outer wall shows positive and negative velocity on one profile, which flips (change the sign) on the opposite wall position.

3. Lecturing eUVP with demonstration

As described above, eUVP is designed to be used in a class room environment by giving demonstration to students. Therefore eUVP software has the Echo panel to show the



echo signal as if on the oscilloscope screen. This is important since one shall know echography of ultrasound wave propagation, by which student shall see a beam behavior since it is invisible.

The main velocity profile panel is a movie screen where instantaneous profile is refreshed every measurement to show a movie. This could impress ones how real flow behavior is different from prior knowledge of fluid mechanics. In order to overview the total spatio-temporal behavior of the flow field, color density plot panel is provided so that typical characteristics of velocity field is visualized for better understanding and comparing with theoretical knowledge.

Flow models chosen here are designed so that student can play with it by themselves with monitoring the flow on the eUVP screen, This kind of interactive practice is the most effective way of teaching not only for understanding the most recent development of the experimental technique - UVP - but also learning the nature of flow of liquid in various configurations.

4. Summary

The OpenUVP is ready to launch eUVP. Hardware is a Pulsar/Receiver designed for educational purpose. Software eUVP is prepared designed for classroom usage.

Two flow models are designed which needs no large equipment to make typical flow fields.

The units will be taken into the market in due course.

References

[1] Takeda Y: Measurement of velocity profile of mercury flow by ultrasound Doppler shift method, Nucl. Technol. 79 (1987), 120-124.
 [2] Takeda Y. Ed. Ultrasonic Doppler Velocity Profiler for Fluid Flow, 2012, Springer

Analysis of Flow Behavior and Evaluation of Agitation Performance by Impeller Using UVP

Hiroya Okumura¹, Kohei Takasaka¹, Naoto Ohmura¹, A Ishihata²

¹ Department of Chemical Science and Engineering, Kobe University

² Sanko Astec, Inc.

Mixing is an industrial process that promotes reaction and heat transport. Flow velocity profile is an important indicator for estimating mixing performance. Because many industrial processes deal with opaque fluids with non-Newtonian properties, optical measurements are not suitable when measuring the velocity of such fluids. This study, therefore, used a cloudy aqueous CMC solution, which is difficult for light to penetrate, and the flow velocity profile was obtained by a UVP measuring system. The mixing performance of two types of impeller (Parallel Paddle® (PP) and disk turbine impeller (DT)) was examined. The velocity profile measurements by UVP successfully identified isolated mixing regions (IMRs) in which intermixing does not occur between the IMR and its surrounding active mixing region in a laminar mixing field. It was also found that the PP exhibited good mixing performance with relatively smaller IMRs than the disk turbine.

Keywords: mixing, stirrer, Parallel Puddle®, UVP

1. Introduction

Mixing is an important unit operation in chemical industries to enhance not only homogenization but also heat and mass transfer by adding appropriate flow motion in a mixing device. Improved mixing performance contributes to lower costs of production processes and higher quality products. Impellers are widely used equipment in the stirring process, mainly to convert the power of rotation into mixing and other effects in the tank. The mixing characteristics, which are the primary and most important aspects of impeller performance, depend on the flow pattern in a mixing device. For example, if there are multiple circulating flows, each independent of the others, the overall mixing performance can be poor. Conversely, if there is interaction among these circulating flows through well-developed turbulent flow motions, the overall mixing can be assumed to be good.

PIV (Particle Image Velocimetry) is a powerful method for determining flow patterns by measuring the velocity field.^[1] However, it requires the fluid to be transparent due to its optical nature. As an alternative method, the UVP (Ultrasonic Velocity Profiler) utilizes the Doppler effect of ultrasonic waves to measure particle velocity,^[2] making it suitable for both transparent and non-transparent fluids. In this experiment, an aqueous CMC (carboxy-methyl-cellulose) solution was used as a typical example of a cloudy and non-Newtonian fluid to investigate the effectiveness of UVP measurements.

Due to the shear-thinning properties of the CMC solution, the fluid near the impeller experiences strong

shear, resulting in lower viscosity and increased fluidization. In contrast, the fluid farther away from the impeller retains high viscosity and exhibits poor fluidization. As a result, a phenomenon occurs where the flow is divided into active and inactive flow regions.^[3]

The purpose of this study is to evaluate the performance of two types of impellers, PP and DT, on a highly viscous CMC solution using UVP measurement. Both impellers employed in this study generate radial discharge flow. Figure 1 (a) illustrates the PP, developed by Sanko Astec, Inc., which is a medium-sized impeller with relatively large blades and a large passing area. Figure 1 (b) shows the DT, a commonly used small agitation blade in various industries. In this study, a standard six-bladed DT was utilized.

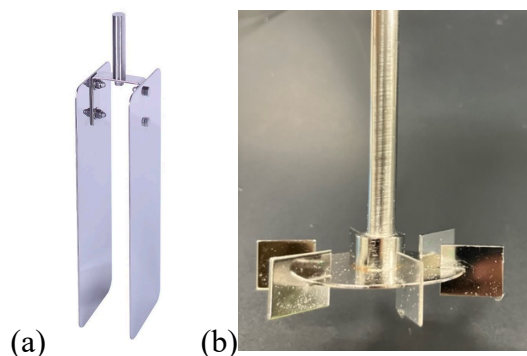


Figure 1: (a) PP, (b) six-bladed DT

2. Material and Methods

To prepare a 3 wt% CMC solution, dissolve 20.76 g of CMC in 6.92 L of tap water and fill an acrylic vessel

with an inner diameter of 0.210 m as the operating fluid. CMC has a molecular structure with numerous branched chains resulting shear-thinning rheological properties. The PP and DT were positioned at the center of the container, as depicted in Figure 2, and rotated at specified rotational speeds. The PP operated at 120 rpm, while the DT operated at 780 rpm, providing equivalent power. Table 1 displays the key dimensions for the agitation tank and agitator blades geometry. A UVP-DUO-Mx (Met-Flow S. A.) was utilized to measure the flow velocity. A 4 MHz transducer was employed, and the main measurement parameters included a sound velocity of 1500 m/s and a sampling interval of 36 ms.

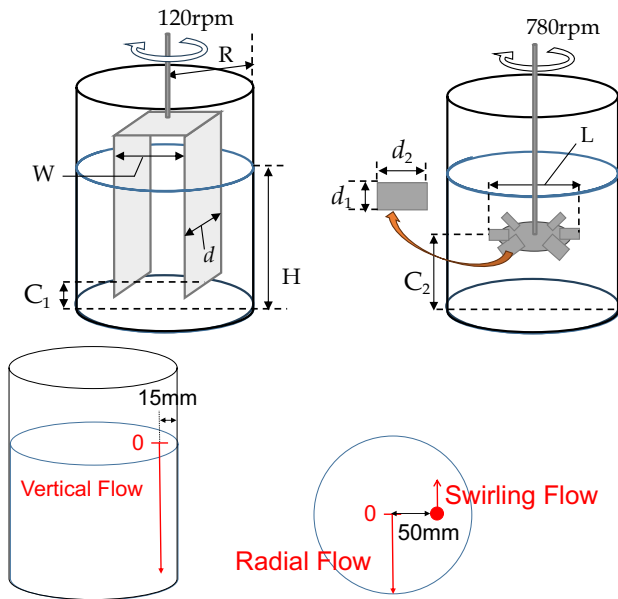


Figure 2: Schematics of experimental equipment

Table 1: Geometrical dimensions of experimental apparatus in mm

R	H	W	d	C ₁	L	d ₁	d ₂	C ₂
105	200	44	70	40	72	18	14	100

Particles of Copolyamid with a particle size ranging from 80 - 200 μm and a density of 1.07 g/m^3 were added to the working fluid at a concentration of 0.1 wt% and well dispersed. Due to the small Stokes number of these particles, which is much smaller than 1, they can be considered to move precisely along the streamlines.

3. Results and Discussion

3.1 Radial Flow

Figure 4 shows the time-averaged radial distribution of radial velocity for the PP. The tops of the agitator blades are out of the liquid surface, so the agitator blades are located 40-200 mm from the bottom of the agitator tank.

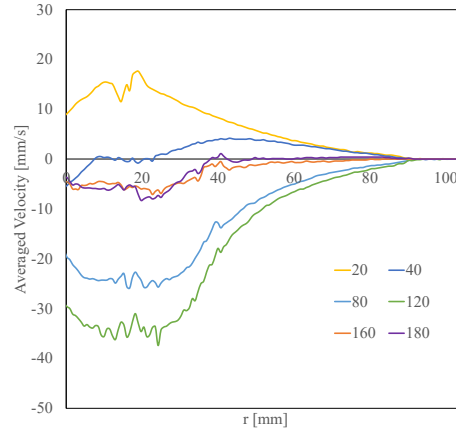


Figure 4: Radial flow velocity profile of the PP

From Figure 4, it can be read that a large outward flow, or discharged flow, exists in the region where the agitation blade is present. Inward flow was observed in the area below the impeller blades at a height of 20 mm, indicating a large circulation. At 160 and 180 mm, which are located at the top of the tank, the velocity was close to zero, indicating a mixture of both outward and inward flow. Figure 5 shows the detailed time-averaged radial distribution of radial velocity at height near the impeller blade tip. The location where the averaged velocity is zero is thought to be where the center of the secondary circulating flow is located.

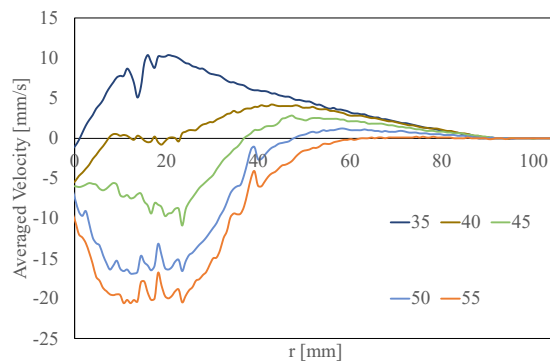


Figure 5: Radial flow velocity profile near the tip of the PP

Figure 6 shows the radial distribution of time-averaged radial velocity on the disk turbine blade. Although there are regions where the velocity exceeds the measurement limit, the discharge flow at a height of

100 mm and the circulating flow seen above and below the discharged flow can be seen, confirming the general features of flow.

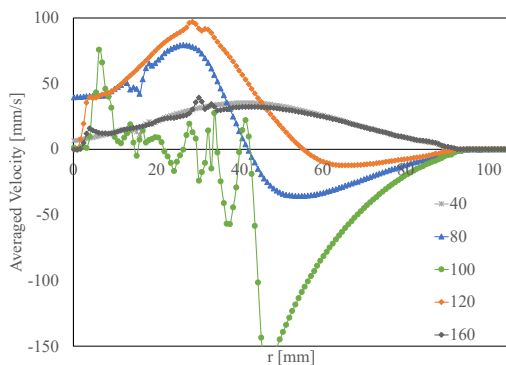


Figure 6: Radial flow velocity profile of the DT

3.2 Swirling Flow

Figure 7 compares the averaged velocity (V_{θ}) of the circumferential flow at different heights at $r=50$ for the two kinds of impellers under the same power consumption. It can be seen that the PP has a higher velocity at the top where the agitator blade is present, which is naturally due to its close to the rotating impeller blade and therefore sufficient momentum transport. The disc turbine blades show higher values in all regions, simply due to the higher rotational speed of the agitator blades under the same power consumption conditions.

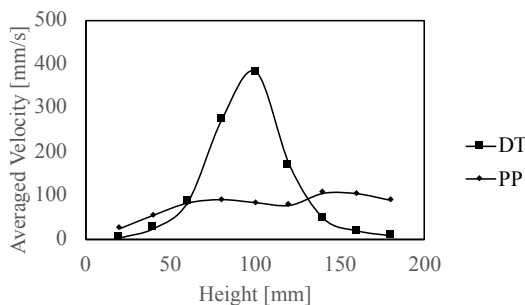


Figure 7: Swirling flow velocity profile of the two impellers

Figure 8 shows the nondimensional time averaged circumferential velocity (V_{θ}) averaged by the radial direction, which is divided by the rotational speed of the impeller and the tank inner diameter. This dimensionless velocity of the PP is greater than that of the disk turbine blade over the entire region. This means that the PP is stronger than the turbine blade in swirl flow formation.

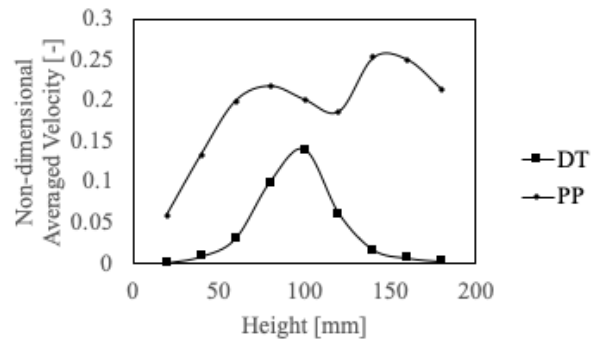


Figure 8: Swirling flow non-dimensional velocity profile of the two impellers

3.3 Vertical Flow

Figure 9 compares the time-averaged axial velocity (V_z) in each height at $r=90$ mm with the two impellers. Here the upward flow is positive. PP has downward flow throughout the tank, but its value is small. On the other hand, the disk turbine blades show vertical flow separation originating from the discharged flow from the blades. PP have relatively little vertical fluid motion.

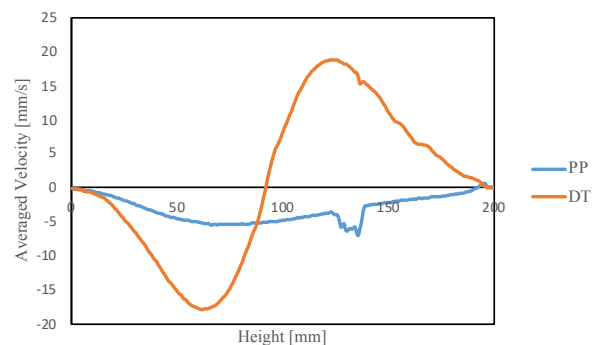
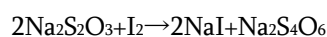


Figure 9: Vertical flow velocity profile of the two impellers

A characteristic behavior can be observed in the mixing of CMC, as depicted in the decolorization experiment presented in Figure 3. The decolorization experiment is based on the oxidation-reduction of iodine, which proceeds according to the following chemical reaction equation.



Decolorization experiments are one of the most effective methods for mixing behavior and evaluation and are frequently used.^[4]

Iodine is dissolved in the fluid at 0.001 mol/L, and 1.5 times the amount of $\text{Na}_2\text{S}_2\text{O}_3$, a decolorizing reagent, is added near the surface of the fluid to achieve chemical equilibrium.

This behavior is believed to result from the division of

the fluid into regions of low viscosity and active flow, as well as regions of high viscosity and mild flow. The region near the impeller blade corresponds to the former, where the decolorization process occurs rapidly. The presence of a wide area of active flow contributes to process efficiency, which is an essential requirement for an impeller. Quantitative analysis of this region serves as an evaluation of the impeller performance as revealed through flow analysis.

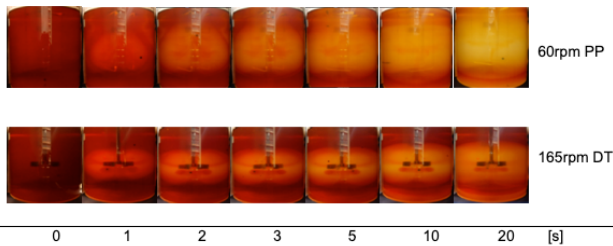


Figure 3: Results of CMC decolorization experiment

Finally, the size of the isolated mixing region (IMR) was estimated from the flow conditions.

The results for the radial and vertical flows indicate that the DT has relatively strong and large vortex flow at the top and bottom. This is not significantly different from the flow behavior in a Newtonian fluid,^[5] and a stable IMR is considered to exist at the two locations. On the other hand, for PP, the discharge flow is generated from the entire paddle, but at the same time, the same amount is drawn into the center from the lower region of the paddle. The PP has a relatively small vortex flow area.

As for the magnitude of the IMR, specific values could not be determined in this experiment. The same can be said for the PP, which has an IMR of about 15 mm in the vertical direction. Similarly, PP is considered to have an IMR of about 10 mm in the height direction. The volume of the IMR in DT is estimated to be roughly 4 times that of PP. It can be concluded that under the conditions of this experiment, PP has a smaller IMR than DT due to the relatively small vortex flow, resulting in better mixing performance.

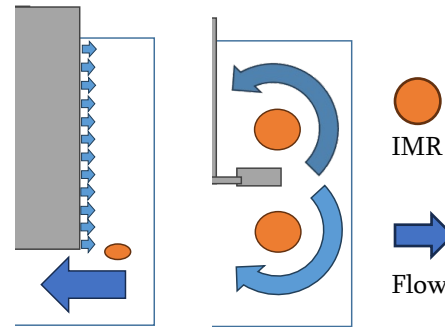


Figure 10: Schematic diagram of half of a tank with IMR and flow conditions

4. Conclusions

It was found that PP has a relatively strong influence on the swirling flow, while the DT has a relatively strong influence on the vertical flow in the flow domain. Since the agitation of the PP strongly forms a swirling flow, it is thought that converting the flow into a vertical flow will improve the mixing property. In the future, we intend to try to improve the mixing using the PP by inserting baffles.

References

- [1] Ramin Z, et al.: A mixing study in a double-Rushton stirred tank, *Computers & Chemical Engineering*, July (2009), 1240-1246.
- [2] Madhavi V, et al.: Solid suspension in stirred tanks: UVP measurements and CFD simulations, *The Canadian Journal of Chemical Engineering*, October (2011), 1112-1121.
- [3] Arratia, P.E., et al.: Mixing of shear-thinning fluids with yield stress in stirred tanks, *AIChE Journal*, July(2006), 2310-2322
- [4] Etchells, A. W., et al.: Blending in unbaffled and baffled mechanically agitated vessels – Effect of Reynolds number and liquid height, *Chemical Engineering Research and Design*, August (2023), 599-605
- [5] Yek, W. M., et al.: Enhanced mixing of Newtonian fluids in a stirred vessel using impeller speed modulation, *The Canadian Journal of Chemical Engineering*, November (2009), 839-845

INVESTIGATION OF FLOW CHARACTERISTICS INDUCED BY VERTICAL HEATED ROD USING ULTRASOUND VELOCITY PROFILER

Thanh Tung Duong¹, Chi Thanh Tran², Tat Thang Nguyen³, Hiroshige Kikura⁴

¹Nuclear Training Center, Vietnam Atomic Energy Institute, 140 Nguyen Tuan, Thanh Xuan, Hanoi, Vietnam

²Vietnam Atomic Energy Institute, 59 Ly Thuong Kiet, Hoan Kiem, Hanoi, Vietnam

³Posts and Telecommunications Institute of Technology, Km10, Nguyen Trai, Ha Dong, Hanoi, Vietnam

⁴Laboratory for Zero-Carbon Energy, Institute of Innovation Research, Tokyo Institute of Technology, 2-12-1 Ookayama, Meguro-ku, Tokyo 152-8550, Japan

Natural convection is a fundamental phenomenon that occurs in numerous areas of application in the industry, nuclear energy, power generation, and electronics cooling. In a nuclear reactor, natural convection is used for residual decay heat removal in case of an incident or accident after reactor shutdown. The design of fuel elements and fuel assembly could influence flow rate and therefore affect nature circulation. One of the most important parameters to understand natural convection is the spatio-temporal velocity profile. Hence, Ultrasonic Velocity Profiler (UVP) is appropriate to observe the natural convection flow behavior. The vertical heated rod with a diameter of 12 mm and length of 225 mm is immersed at the center of a vertical pipe made of acrylic with a diameter of 145.8 mm and height of 500 mm. The ultrasonic transducer is placed outside of the pipe to measure the long-term flow behavior. Using the UVP technique, the one-dimensional horizontal velocity distribution inside the pipe is observed. Accordingly, the velocity profile of UVP is confirmed with PIV method.

Keywords: Natural convection, UVP, PIV, nuclear reactor, heater rod

1. Introduction

The flow driven by natural convection is very important in geophysics, astrophysics, and nuclear engineering, such as residual decay heat removal of nuclear fuel in case of an incident or accident. The natural convection flow behavior is conventionally induced by different temperatures and driven by buoyancy force. In a nuclear reactor, the fuel element is placed sufficiently far, allowing residual heat removal. Furthermore, advanced nuclear power plant has now developed various passive cooling system types. For example, heat is removed from the steam generator by connecting it with the cooled water on the top of the reactor building. Thus, understanding the natural convection flow is significant to optimize and verifying the safety design system. In Vietnam, a new multiple purposes nuclear research reactor (MPRR) is introducing by using the hexagonal fuel element which include various layers (6-8). The distance between the layers is 2 mm, so-called narrow gap. In order to ensure the safety operation of new research reactor, the heat removal from the residual heat of narrow gap fuel need to be investigated.

Choi et al. [1] has reviewed the passive heat remove system of the advanced design of nuclear reactor and recommended that several characteristics of natural convection need to be clarified. Park et al. [2] has conducted the experiment with a single horizontal heater rod to clarified the large vortex and energy dissipation using LIF/PIV. Bazoz et al. [3] provided the simulation of natural convection with adding the temperature dependence of physical variables. However, the mentioned works have been observed the natural convection shortly and do not provide the heat transfer behavior of heated object. Therefore, for MPRR, the computational fluid Dynamic (CFD) is recommended to applied to understand the heat transfer and heat removal for each fuel element in

case of normal or incident/accident scenario. However, the CFD simulation results including the turbulence model need to be validated with experimental data. Therefore, a simplified natural convection using a single heater rod is conducted. Regarding to the flow measurement, the Ultrasonic Velocity Profiler is used by giving the spatio-temporal velocity profile. Besides, the spike-excitation ultrasonic pulse has widely used in Non-destructive Testing was applied. The equipment used for the UVP measurement was in-house development including hardware and software. The UVP system comprises an Ultrasonic transducer (emitting the ultrasound pulse) and the pulser/receiver which has highspeed digitizer and a signal processing algorithm developed by Labview. On the other hand, the sound speed is a function of temperature that effect on the measurement accuracy. Therefore, the flow measurement using UVP method need to be confirmed with PIV.

2. Experimental setup

2.1 Experimental apparatus of natural

The main test section is the vertical heated rod with a diameter of 12 mm and length of 22.5 mm. The heated rod was immersed at the center of a vertical pipe made of transparent acrylic with an inner diameter of 144 mm and a height of 500 mm. The transparent acrylic has a thickness of 3 mm for illumination and image acquisition. The ultrasonic transducer was placed outside of the pipe to measure the long-term behavior of flow behavior. The working fluid is water and the initial temperature (T_{in}) was kept at room temperature (27 °C). The power set to heater rod is 100 W corresponding to heat flux of 11864 W/m². The UVP measurements require the suspension of US (ultrasonic) wave-reflecting particles in the fluid. Nylon powder ($d=80 \mu\text{m}$; $\rho = 1020 \text{ kg/m}^3$) was dispersed in

working fluid as reflector particles for both UVP and PIV (Particle Image Velocimetry) measurements (Figure 1 and Figure 2). A camera with 60 fps was used to record the movement of particles illuminated by a laser sheet. This data allows one to analyze the 2-dimensional velocity distribution using the PIV method.

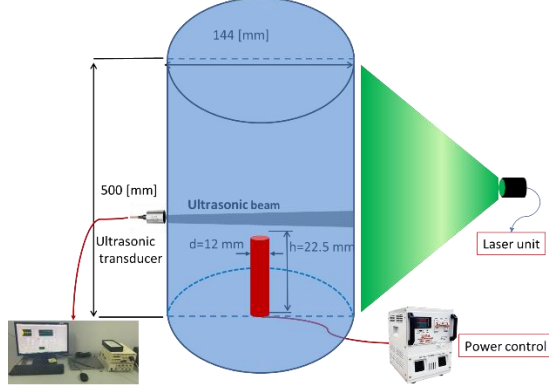


Figure 1: Sketch of vertical heated rod natural convection and test section for measurement. Number shows the length in mm.

The Rayleigh number (Ra) is defined as follows:

$$Ra = \frac{g\beta\Delta TL^3}{\alpha\nu} \quad (1)$$

Where L is characteristic length, $\Delta T = (T_{bulk} - T_{in})$, g is the coefficient of acceleration, β is the thermal expansion coefficient, α is the thermal diffusivity, and ν is the kinematic viscosity of the fluid. The $Ra = 2.3 \times 10^{10}$ and is supposed to be convective natural turbulent flow.

2.2 Principle of UVP technique

The flow behavior in the test was observed using the ultrasound technique. The principle of the UVP method is based on the echography of ultrasound [5].

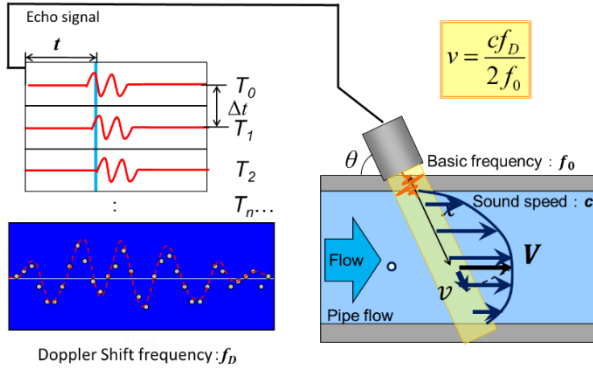


Figure 2: Principle of UVP technique

Table 1: Condition for UVP measurement

Basic frequency	4 MHz
Effective diameter	4 mm
Sound velocity	$c = 1480$ (m/s) at 26 °C
Pulse repetition frequency	4 kHz
Temporal resolution	51 ms
Velocity resolution	0.21 (mm/s)
Chanel distance	0.74 mm
Pulse type	Spike-excitation pulse

The transducer emitted a pulse and receives the echo signal reflected from the particle suspended in the liquid. The information of position in each channel was extracted from the time delay τ_{prf} or pulse repetition frequency $f_{prf} = 1/\tau_{prf}$ as follows:

$$x = \frac{c \times \tau_{prf}}{2} \quad (2)$$

where c is sound speed in the medium.

By analyzing the echo signal such that the instantaneous frequencies at various instants after the emission was computed (called Doppler frequency). The instantaneous local velocity, $V_{UVP}(x)$ was derived from Doppler shift frequency (f_D) at the time and position as:

$$V_{UVP}(x) = \frac{c \times f_D}{2f_0} \quad (3)$$

where f_0 is the basic ultrasonic frequency.

The basic frequency of ultrasound was 4 MHz using a transducer of 4 mm in effective diameter. The spatial, temporal and velocity resolution of UVP measurement were 0.74 mm, 51 ms, and 0.21 mm/s, respectively. In this measurement, the transducer is put outside the pipe and make an angle of 45 °C with the pipe and located 5 cm away from the top of heater rod.

3. Results

3.1 Experimental data

The horizontal component of velocity in the direction of the ultrasonic beam was measured. The figure 3 show the average horizontal velocity profile. Figure 4 shows the vertical velocity component by the UVP for the natural convection induced by a single heated rod. The vertical axis means the distance from the transducer, and the horizontal axis is the time elapsed from starting measurement (500 s in this case). The most advantage for using the UVP is that we can get the spatiotemporal velocity profile. The magnitude of the vertical velocity along the measurement line is displayed in color scale: yellow to red ($0 < \text{velocity} < -0.025$) indicates the velocity moving toward from the transducer (upward in the figure), and green to blue ($0.025 < \text{velocity} < 0$) is the velocity moving away the transducer (downward in the figure) and black color indicates velocity is zeros. The spatio-temporal velocity profile using UVP technique shows clearly that the upward flow is occurred at the center of pipe where the heater rod is located. Flow near the pipe wall is very low. This result is confirmed by 2-dimensional velocity distribution using PIV method in figure 5.

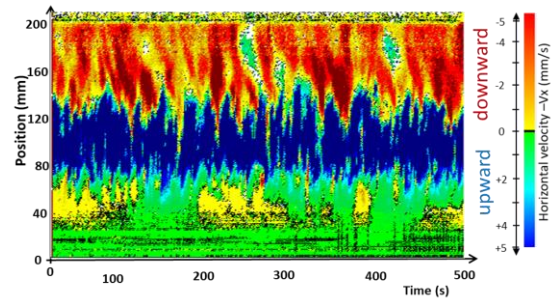
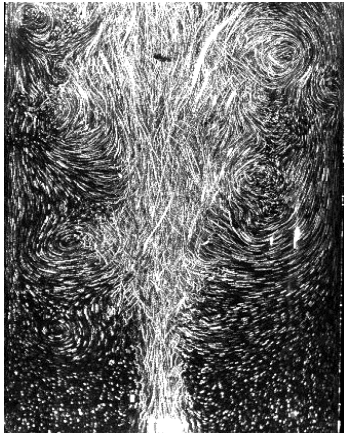
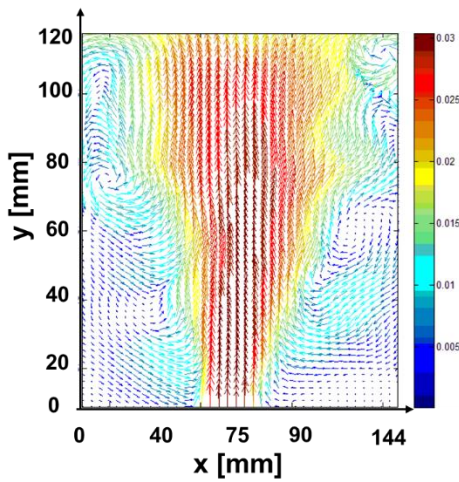


Figure 3: The spatio-temporal of horizontal velocity

profile using UVP method



(a)



(b)

Figure 4: Flow visualization (a) and mean flow field using PIV method

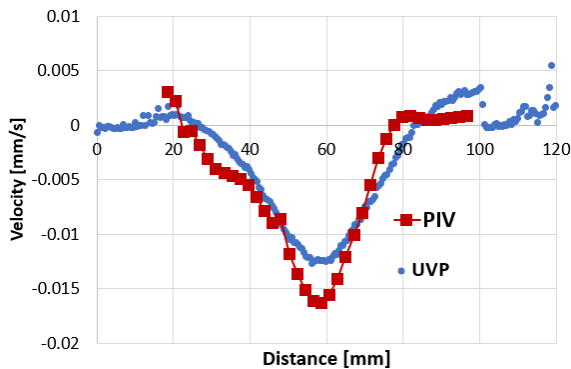


Figure 5: The comparison of UVP and PIV method.

The Figure 5 shows the confirmation of UVP and PIV method. This result shows very good agreement between 02 methods and the error is less than 5%.

The figure 4 shows the typical natural flow induced by heater rod. The upward flow along the heater rod is very clearly observed. The density of water close to the heater rod is decreased and went to the colder region due to the buoyancy force. The water descends when reaching the

upper wall. Therefore, in the upper region of heater rod and the upper part of the container, the upward and downward flow induce a very complicate flow behavior in which the energy dissipation and transfer is need to be investigated. The results show clearly that the plume is mainly concentrated on the region close to the heater rod.

3.2 Simulation results

The Ansys/Fluent was applied to simulate the natural convection induced by single heater rod. Since the flow was turbulence, the realizable k-ε was chosen and coupled algorithm was applied for solution. And the four physical properties blow were modeled as a function of temperature as follows [4]:

- Dynamic viscosity (Pa.s)

$$\mu = [-0.00018567 \times T^3 + 0.19712 \times T^2 - 70.15 \times T + 1801.04]/100000$$

- Specific heat (J/kg.K)

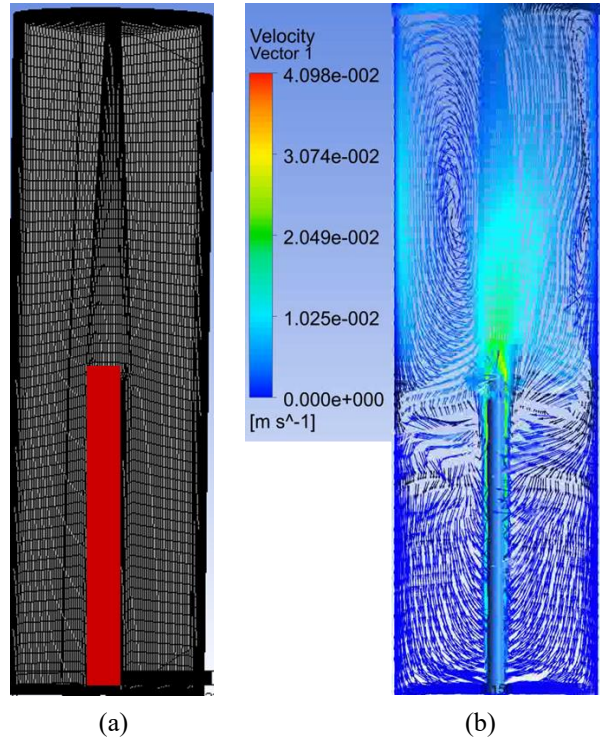
$$c_p = 0.0092 \times T^2 - 5.6859 \times T + 5058.24$$

- Thermal conductivity (W/m.K)

$$\kappa = -0.00000905 \times T^2 + 0.007048 \times T - 0.6893$$

- Thermal expansion coefficient (1/K)

$$\beta = -0.000000029783 \times (T - 273.15)^2 + 0.0000103247 \times (T - 273.15) + 0.00000755683$$

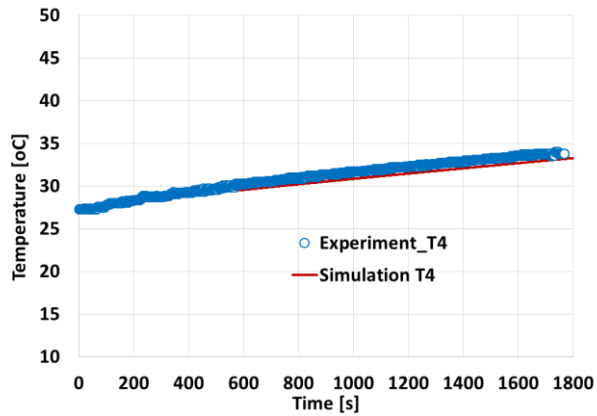


(a)

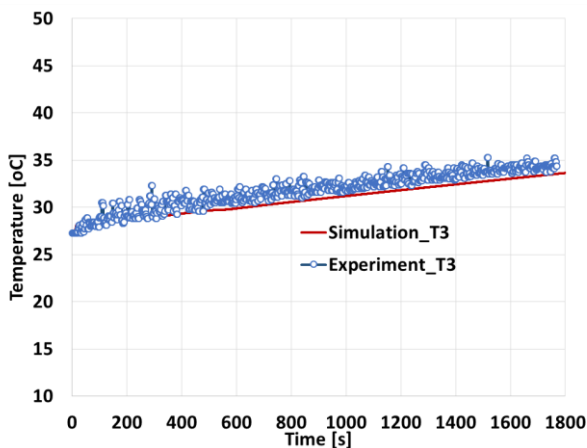
(b)

Figure 6: The mesh used for simulation (a) and the simulation result at 600 s using ANSYS/Fluent (b)

In order to compare the simulation results as well as the turbulence model, the flow behavior and temperature history were selected. The pointwise temperature at $(x^*=-72, y^*=7.5, z^*=0)$ (T4) and $(x^*=-72, y^*=7.5, z^*=0)$ (T3) were measured using k-type couple.



(a)



(b)

Figure 7: The comparison of temperature history between simulation and experimental data (a) at $x^*=-72, y^*=7.5, z^*=0$ and (b) at $(x^*=-72, y^*=7.5, z^*=0)$

The figure 7 show very good agreement between the experimental data and simulation result. That could conclude that the realizable k- ϵ is suitable for natural convection simulation.

4. Summary

The experiment of natural convection flow for a single rod is built up. The experimental data show that the flow behavior is significant for understanding heat transfer in natural convection. The advanced UVP technique is applied to measure the spatial-temporal velocity profile, supplemented with PIV and Image processing techniques for flow characteristics.

The thermal plumes are observed by 2-D visualization in which the middle-upper part of the vertical pipe is the competitiveness of small and large-scale circulation induced by upward flow (buoyancy flow) and downward flow from the upper container part.

Ultrasound technique is useful to observe instantaneously natural convection flow by giving a spatiotemporal velocity profile which is easy set up along the pipe. Therefore, this technique is very helpful to understand the flow characteristic in the given region where the effect of buoyancy or large/small scale circulation is determined. For simulation of natural convection induced by vertical

heated rod, the realizable k- ϵ was suitable for simulation.

References

- [1] Choi JH, Cleveland J, and Aksan N: Improvement in understanding of natural circulation phenomena in water cooled nuclear power plants. *Nuclear Engineering and Design* 241 (2011), 4504- 4514.
- [2] Park H, Park J, Jung S.Y: Measurements of velocity and temperature fields in natural convective flows, *Int. Journal of Heat and Mass Transfer* 139 (2019), 293–302.
- [3] Foroozani N, Krasnov D & Jörg Schumacher: Turbulent convection for different thermal boundary conditions at the plates, *J. Fluid Mech.* 907 (2021), A27
- [4] Boz Z, Erdogdu F & Mustafa Tutar: Effects of mesh refinement, time step size and numerical scheme on the computational modeling of temperature evolution during natural-convection heating, *Journal of Food Engineering* 123 (2014), 8–16.
- [5] Takeda Y: Velocity profile measurement by ultrasonic doppler method, *Exp. Thermal and Fluid Sci.* (10) 4, (1995), 444-453.

Nonlinear large-scale flow transition in a precessing cylinder and its potential for hydromagnetic dynamo action

Thomas Gundrum¹, Vivaswat Kumar, Federico Pizzi, André Giesecke, Frank Stefani, Sven Eckert.

Helmholtz-Zentrum Dresden-Rossendorf, Bautzner Landstraße 400, 01328 Dresden, Germany

In this paper, we present an experimental investigation that centers on exploring the fluid dynamics within a precessing cylinder. Our research is part of the DRESHDYN project at Helmholtz-Zentrum Dresden-Rossendorf, specifically focusing on the precession dynamo experiment. The primary objective of our study is to examine how different rotation configurations influence the dominant flow modes inside the precessing cylinder, specifically considering the prograde and retrograde rotations. Our main focus lies on two significant flow modes: the directly forced mode ($m1, k1$) and the non-geostrophic axisymmetric mode ($m0, k2$). These modes hold substantial potential for precession-driven dynamo action. By analyzing the outcomes between the prograde and retrograde configurations, we gain valuable insights into the prevailing flow patterns within the precessing cylinder.

Keywords: Precession, DRESHDYN, modes, dynamo

1. Introduction

Rotational flows are present in diverse environments, including the rotation of fuel payloads in spacecraft, atmospheric phenomena like tornadoes and hurricanes, bodies of water such as oceans and lakes, as well as in astrophysical and numerous technical applications. The presence of rotation in a system allows for the existence of inertial waves, which arise due to the restorative influence of the Coriolis force. One method of exciting inertial waves is through a phenomenon known as precession, which involves simultaneous rotation around two axes, as depicted in Figure 1. Previous studies have demonstrated that precession can efficiently drive flow in a rotating container without the need for a propeller or pump [1]. In this context, there has been some debate [2] regarding whether the Earth's magnetic field was generated primarily through precession-driven flow rather than, or in addition to, convection. Several numerical studies have shown that precession-driven flows can indeed generate magnetic fields [3, 4, 5].

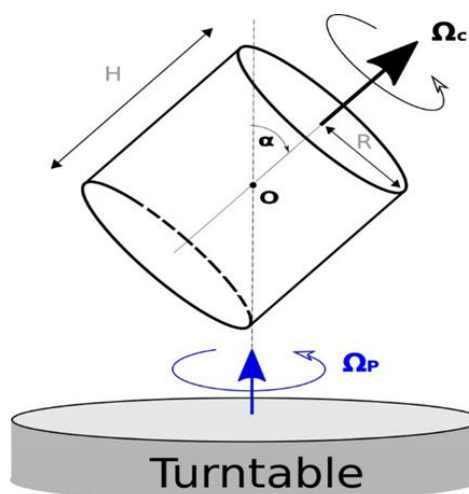


Fig. 1. Schematic representation of precessional motion. [6]

In 1971, Gans conducted a precession-driven liquid metal experiment, achieving a three-fold amplification of the magnetic field [7]. This experiment served as the basis for the development of a larger precession dynamo experiment as part of the DRESHDYN project, currently being constructed at Helmholtz-Zentrum Dresden-Rossendorf (HZDR). The experiment involves a cylinder with a radius of $R = 1$ m and a height of $H = 2$ m. The cylinder rotates around its symmetry axis at frequencies up to $f_c = 10$ Hz and precesses around another axis at frequencies up to $f_p = 1$ Hz. Liquid sodium will be used as the working fluid in this experiment to induce dynamo action [8].

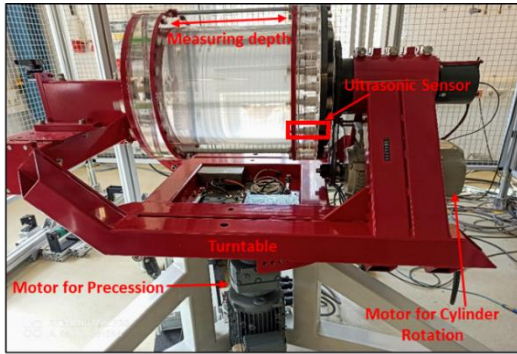
In order to gain a better understanding of the flow dynamics in the large-scale precession dynamo experiment planned within the DRESHDYN project, a downscaled 1:6 water mock-up experiment with identical aspect ratio and rotation rates has been constructed. By conducting this downscaled experiment, valuable insights can be obtained regarding the flow behavior and the most influential factors in preparation for the forthcoming large-scale precession dynamo experiment. The primary objective of this water experiment is to identify the optimal operating parameters in the context of the future large-scale experiment. There are many parameters influencing the flow inside the precessing cylinder [9]. These include four key parameters: (i) geometric aspect ratio – height (H) to radius (R) ratio of the container; (ii) precession ratio (Po) – precession frequency (f_p) to rotation frequency (f_c) ratio; (iii) nutation angle - angle between precession and rotation axis and; (iv) Reynolds number ($Re = \Omega_c R^2 / \nu$) - Coriolis force to viscosity ratio, where ν is the kinematic viscosity. This study expands the work of Kumar et al. [10] where the influence of nutation angle with different configuration of cylinder rotation is presented (i.e. prograde or retrograde). Prograde precession takes place when the projection of the turntable rotation on the cylinder rotation is positive, while retrograde precession occurs when the

projection is negative. In this paper we present the preliminary experimental results at nutation angle, $\alpha = 80^\circ$.

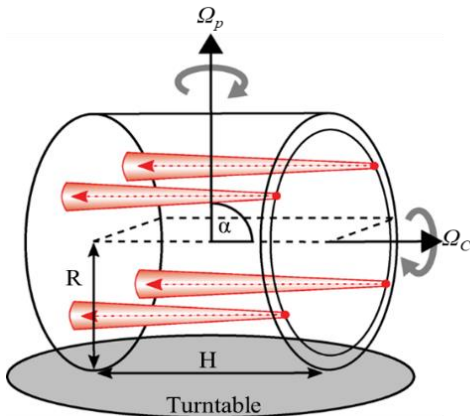
2. Downscaled water precession experiment

2.1 Setup

Figure 2(a) presents the downscaled water precession experiment, scaled at a ratio of 1:6. The experimental setup consists of a cylindrical vessel with a radius of 163 mm (R) and a height of 326 mm (H). The vessel is filled with water and undergoes rotation around its symmetry axis utilizing an asynchronous 3 kW motor connected via a transmission chain. This entire structure is mounted on a turntable, which is driven by a second asynchronous 2.2 kW motor. The maximum rotation rate achievable for the cylinder is $f_{c_{max}} = 10$ Hz, while the maximum rotation rate for the turntable is $f_{p_{max}} = 1$ Hz. The rotation rates of both the cylinder and the turntable are continuously monitored using two tachometers and recorded by a data acquisition system. For the purpose of analyzing the flow patterns within the cylinder, Ultrasonic Doppler Velocimetry (UDV) sensors are positioned at one end cap, as depicted in Figure 2(b). These sensors are oriented parallel to the central axis and capture the instantaneous axial velocity distribution between the two end caps of the cylinder.



(a)



(b)

Figure 2: (a) Setup of 1:6 downscaled water precession experiment. (b) Sketch of the water experiment with four ultrasound probes mounted at one end cap of the cylinder.[8]

2.2 Flow measurement procedure

In order to determine the flow characteristics inside the cylinder, ultrasonic transducers are positioned at one end cap of the cylinder, as shown in Figure 2(a). These transducers are connected to an ultrasound Doppler velocimeter (UDV), which measures the velocity with a temporal resolution of 0.47 Hz.

Before commencing the experimental run, the water undergoes vigorous mixing at a high rotation rate to ensure uniform distribution of tracer particles throughout the cylindrical vessel. Once achieved, the vessel is set into rotation at a frequency of f_c until the fluid co-rotates with the vessel. This co-rotation is indicated by a negligible velocity reading on the UDV channel. Subsequently, the turntable is set in motion at a frequency of f_p after a certain waiting period, and data recording is initiated. After approx. every 45 rotations of the cylinder, the rotational rate of the turntable is increased. The Poincaré number is varied within the range of 0.028 (i.e., $f_p = 0.0021$ Hz) and 0.19 ($f_p = 0.011$ Hz). Furthermore, the precession angle, which is the angle between Ω_p and Ω_c , is maintained at a constant value of 80° . Note that the considered rotation rate of cylinder (i.e. $f_c = 0.06$ Hz) corresponds to $Re = 10^4$.

3. Results

In this section, we present the outcomes of the water precession experiment and the flow pattern derived from the measurement of Ultrasonic Doppler Velocimetry (UDV). The contour plot in Fig. 3 displays the obtained flow structures. The plot demonstrates the temporal and spatial evolution of the axial velocity profile u_z , as it varies with time t and depth z (indicating the distance along the axis of the transducer). The prevailing oscillatory pattern of the velocity profile, characterized by the rotational frequency of the cylinder, represents the standing inertial mode with $(m1, k1)$, as recorded by the UDV sensor attached to the rotating vessel wall.

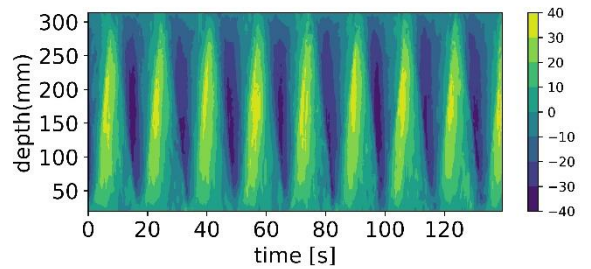


Figure 3: Axial velocity component at sensor 9 (located 150 mm from the centre of cylinder) for a rotation rate of 0.06 Hz and $Po = 0.093$. The $m=1$ Kelvin mode is fixed to the turntable frame.

In a quantitative analysis, the mode amplitudes are determined through the decomposition of the axial velocity field u_z into (m, k) modes. To achieve this, a discrete sine transformation (DST) is initially applied to the axial velocity at each time step during the experiments. A more detailed explanation of the calculation of inertial

mode amplitudes can be found in Ref. 10. In our analysis, we focused on specific modes, namely (m1, k1) and (m0, k2), which exhibit significant amplitudes and hold particular relevance for dynamo action.

Figure 4 depicts the temporal changes in the amplitudes of the dominant modes as the Poincaré number (Po) increases for both prograde and retrograde cases. The analysis was conducted at a precession angle of 80° and a Reynolds number (Re) of 10^4 . For prograde case, we observe an increase in the amplitude of (m1, k1) mode up to a Po of approximately 0.093. However, beyond this threshold value, there is an abrupt shift (within some revolutions) in the flow state caused by the breakdown of the (m1, k1) mode. This breakdown marks the transition from a laminar to a turbulent state. Concurrently, within a narrow range of Po , an emergence of the axially symmetric mode (m0, k2) has been seen (cf. Fig. 4 (a)). This mode corresponds to a double-roll structure, which has previously been identified as highly relevant for dynamo action [11]. On the other hand, the data obtained for the retrograde case do not exhibit a distinct breakdown of the directly forced mode, i.e. (m1, k1), the amplitude of this mode gradually decreases. However, a smoother behaviour of the amplitude of the axially symmetric mode (m0, k2) within the range of considered Po has been noticed (see Fig. 4 (b)). The potential of retrograde precession to generate a more robust large-scale flow amplitude without causing a sharp breakdown of the directly forced mode (m1, k1) is intriguing for dynamo applications. This characteristic could be significant for dynamo applications since it permits the injection of more energy into the flow without disrupting the base flow. In comparison to the prograde case, the critical values of Poincaré number (Po^c) are shifted towards larger values for the retrograde case. Power measurements of the cylinder manifest the same tendency [12] and will be analysed for present measurements in the near future.

5. Summary

This study focuses on examining the impact of 80° nutation angle on a precession-driven flow in a cylindrical geometry, considering both prograde and retrograde rotation directions. Experimental measurements using the UDV sensor mounted on the cylinder's end cap were conducted, and these measurements were then analyzed by decomposing the axial velocity fields into various (m, k) modes. Specifically, we considered the (m1, k1) and (m0, k2) modes due to their significant amplitudes and relevance to dynamo studies.

For the prograde cases, a transition from a laminar to a turbulent regime was observed. In contrast, the retrograde motion did not show a clear breakdown of the directly forced mode (m1, k1), but instead exhibited a smoother behaviour of the non-geostrophic axisymmetric mode (m0, k2). Notably, the retrograde cases are of particular interest for dynamo studies as the absence of a breakdown in the directly forced mode allows for increased energy injection into the flow without disrupting the base flow. In future investigations, we plan to extend this experimental work

to higher Reynolds numbers.

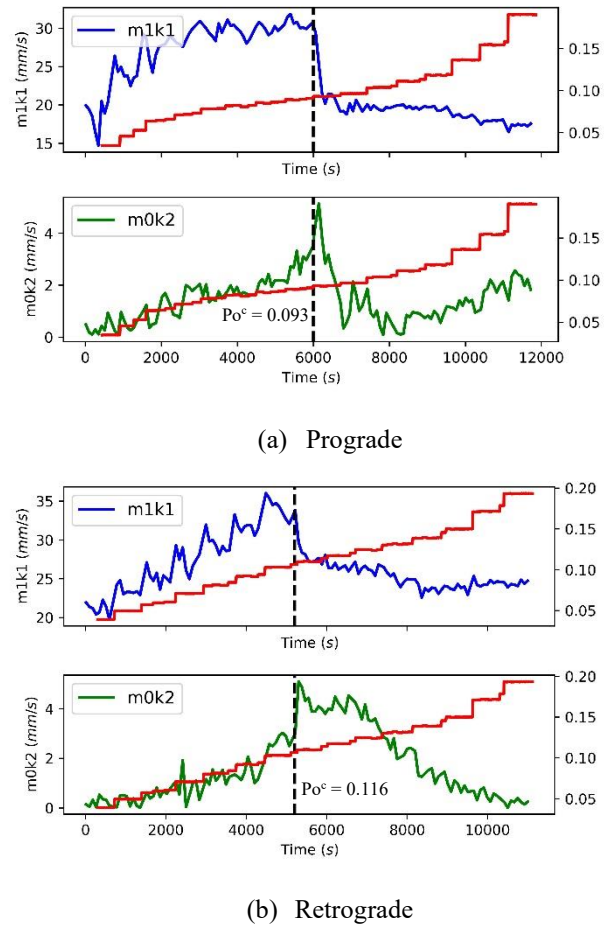


Figure 4: Amplitudes of the directly forced mode (m1,k1) and the axisymmetric mode (m0,k2) for the precession angle of 80° at $Re = 10^4$. The red lines show the Poincaré number.

References

- [1] Leorat J. et al. Dissipation in a flow driven by precession and application to the design of a MHD wind tunnel. *Magnetohydrodynamics*, vol. 39 (2003), pp. 321-326.
- [2] Malkus W. Precession of the earth as the cause of geomagnetism: Experiments lend support to the proposal that precessional torques drive the earth's dynamo. *Science*, vol. 160 (1968), pp. 259-264.
- [3] Tilgner A. Precession driven dynamo. *Phys. Fluids*, vol. 17 (2005), Art. No. 034104.
- [4] Nore C. et al. Nonlinear dynamo action in a precessing cylindrical container. *Phys. Rev. E.*, vol. 84 (2011), Art. No. 016317.
- [5] Wu C. C. and Roberts P. H. On a dynamo driven topographically by longitudinal libration. *Geophys. Astrophys. Fluid Dyn.*, vol. 107 (2013), pp. 20-44.
- [6] Pizzi F. et al. Ekman boundary layers in a fluid filled precessing cylinder. *AIP Advances*, 11 (2021), Art. No. 035023.
- [7] Gans R. On hydromagnetic precession in a cylinder. *Journal of Fluid Mechanics*, vol. 45 (1971), pp. 111-130.
- [8] Stefani F. et al. DRESHDYN - A new facility for MHD experiments with liquid sodium. *Magnetohydrodynamics*,

vol. 40 (2004), pp. 1-10.

- [9] Pizzi F. et al. Prograde and retrograde precession of a fluid-filled cylinder. *New J. Phys.*, vol. 23 (2021), Art. No. 123016.
- [10] Kumar V. et al.; The effect of nutation angle on the flow inside a precessing cylinder and its dynamo action. *Phys. Fluids*, vol. 35 (2023), 014114.
- [11] Giesecke A. et al. Nonlinear large-scale flow in a precessing cylinder and its ability to drive dynamo action. *Phys. Rev. Lett.*, vol. 120 (2018), Art. No. 024502.
- [12] Gundrum T. et al. Ultrasonic flow measurements in a downscaled water mockup of a large scale precession driven dynamo experiment. ISUD8, Helmholtz Zentrum Dresden Rossendorf, Germany, Sept. (2012).

Monitoring of Liquid-solid two-phase pipe flow using ultrasonic pulses

Hyun Jin Park¹, Takumi Hayashi¹, Dongik Yoon¹, Yuji Tasaka¹, Yuichi Murai¹,
Satoru Takano², and Sotaro Masanobu³

¹Laboratory for Flow Control, Division of Mechanical and Aerospace Engineering, Faculty of Engineering, Hokkaido University, N13-W8, Kita-ku, Sapporo 060-8628, Japan

²Ocean Engineering Department, National Maritime Research Institute, 6-38-1, Mitaka, Tokyo 181-0004, Japan

³Offshore Advanced Technology Department, National Maritime Research Institute, 6-38-1, Mitaka, Tokyo 181-0004, Japan

Acoustic measurement using ultrasonic pulses emitted from outside the pipe wall was tried to measure a solid–liquid two-phase pipe flow. The two-phase flow is generated by adding 4 mm alumina spheres into a base liquid flow in a pipe with a 26 mm inner diameter. We emitted 4 MHz ultrasonic pulses with 4 cycles into the pipe and received echo signals reflected from solid particles. Particles were detected using a high intensity of their echo signals and their velocity was measured from the Doppler effect on the signals. Particles farther from the transducer are less detectable because particles farther from the transducer are hidden behind particles closer to the transducer. We tried to restore a particle existence probability distribution by two assumptions: linearly decreased detection rate and the statistical axial symmetry of the distribution on the measurement line. We also tried to estimate the size of particles using the phase of signals. The echoes at the solid-liquid interface and the liquid-solid interface on particles have opposite phases because of the difference in acoustic impedance of each phase. It is possible to estimate the particle size by detecting the phase-reversed pair of echoes and evaluating their time difference.

Keywords: Liquid-solid two-phase pipe flow, Particle velocity distribution, Particle size estimation, Particle existence probability distribution

1. Introduction

Energy storage and conversion technologies are essential technologies to realize a sustainable society and use energy with high efficiency. Most of them are supported by rare metals, and a stable supply of rare metals is necessary for the operation of these technologies. A huge amount of mud containing rare metals is buried in the deep seabed, and its mining is expected as one of the solutions for the stable supply [1]. The slurry [2] and airlift [3] methods have been used to continuously transport a large amount of excavated mud from the seabed to the sea surface. Since the inside of the transport pipe whose length is several kilometers long cannot be monitored, the amount of mining can only be grasped after the transportation. As a result, we know whether the mining site was appropriate only after a considerable amount of time has passed since mining in the deep sea. If it is possible to monitor solid particles near the inlet of the pipe, the amount of mining can be estimated immediately at the start of pumping and without pumping the particles to the surface.

Although already many methods for measuring liquid–solid two-phase flow have been developed and used [4], considering abrasion caused by the particles and pressure drop in the transportation pipe, an ultrasonic measurement which is non-invasive and has high durability is suitable as a monitoring method of this pipe. We have already performed ultrasonic measurements in various multiphase pipe flows, and have experience in detecting the velocity profiling in the liquid-phase from the Doppler effect contained in the echo signal and the gas-liquid interface from the intensity of the echo [5–7]. For evaluating the transport volume of mined mineral

resources, first, in this paper, we try to obtain the solid phase information such as particles' size, velocity distribution and existence probability distribution, necessary for estimating the transport volume from ultrasonic echo signals.

2. Experimental facility

Fig. 1 shows a schematic diagram of the experimental facility. The facility was constructed with two vertical pipes whose diameter and length were 26 mm and about 10 m respectively, a slurry pump, a mixing tank, a particle feeder and four water jackets. The feeder continuously injected a constant supply of 4 mm size aluminum spheres near an inlet of flow pass in the tank, and this liquid–solid two-phase fluid was sucked and sent into the pipe by the pump. A net was installed inside the mixing tank to prevent the particles from circulating again and therefore only water was circulated. In the experiment, the liquid flow rate and particle volume fraction were $Q_L = 6.0 \text{ m}^3/\text{s}$ and $\alpha_S = 8\%$, respectively. These values were obtained by measuring the weight of each phase of the two-phase flow returning to the mixing tank in a period. Two water jackets for the ultrasonic measurement were installed at a 4 m distance on each of the updraft and downdraft pipes. A 4 MHz transducer (TDX) for emitting and receiving ultrasonic pulses, and a mirror for visually observing the flow inside the pipe were placed in each jacket. TDXs were connected with an ultrasonic pulser (JPR-600C, Japan probe) and a data logger (PicoScope 6000 series, Pico Technology). The setting parameters of these instruments are summarized in Table 1. By use of the mirror in the jacket, stereo pictures taken from two different viewing directions were obtained by a camera (HAS-L1, Ditect)

working simultaneously with the data logger. Camera's frame rate was 500 fps and the difference between the two viewings was 90°.

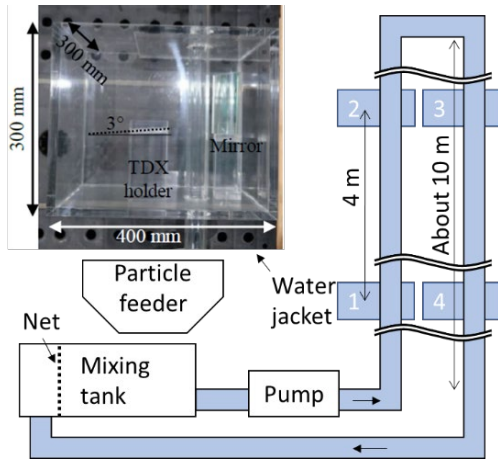


Figure 1: Schematic diagram of the experimental facility and a picture of a water jacket, where a TDX is installed with 3° to measure particle velocity in the streamwise direction and a mirror is set to take stereo pictures by a camera. The number in each jacket indicates a label of measurement points and a TDX number.

Table 1: Parameters for ultrasonic measurement

Ultrasonic pluser (JPR-600C)	
Basic frequency	4 MHz
Pulse repetition frequency	4 kHz
Cycles of pulse	4
Emission voltage	150 V
Data logger (PicoScope 6000 series)	
Voltage range	±1 or ±2 V
Voltage resolution	8 bit
Sampling frequency	52 MHz
Recording time	5 s

3. Results and discussions

3.1 Original data: optical image and echography

Before performing the ultrasonic measurement, first, we show a sample of stereo pictures taken around TDX2 to understand the state of solid particles in the pipe flow. The alumina spheres are visualized as black circles in the picture. Although some of the particles are densely packed and appear to form clusters, they do not appear so when viewed from a 90-degree angle at the same height in the picture. It suggests that they were distributed almost randomly in the pipe and their time-averaged distribution is uniform.

Fig. 3 shows a sample of the time-space echography. The distance x on the horizontal axis in the figure is calculated by multiplying the time of flight of the ultrasonic pulse and the speed of sound in water. The pipe wall near TDX is visible on the echography at $x = 0$ mm. The opposite side wall at $x = 26$ mm, unlike the other side

wall, appears to be interrupted on the time axis. This is because when many particles cross the measurement line, the ultrasonic pulse is scattered by them and weakened. When the echo intensity weakening occurs, it is confirmed that high echo intensities from the particles suddenly appear between the two walls. We extracted the echo from particles using high echo intensities over a threshold and analyzed only these echoes. A value exceeding 2σ of its average at each position on echo intensity profiles was taken as the threshold.

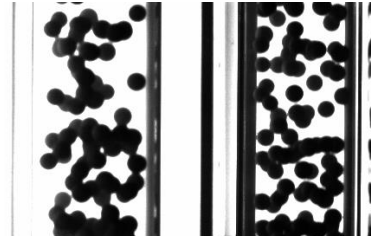


Figure 2: Sample stereo picture taken by a camera, where black circles are alumina spheres.

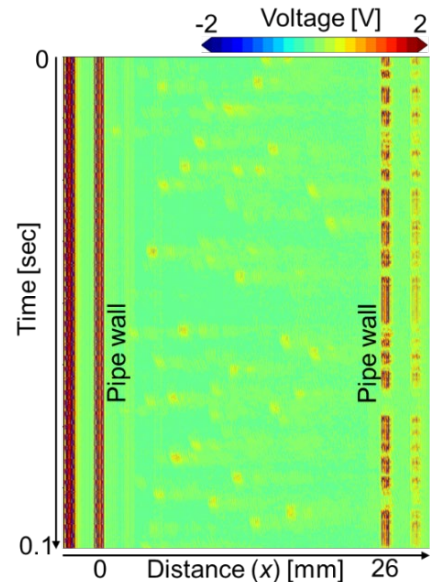


Figure 3: Sample of echography, where high amplitudes between two walls indicate alumina spheres.

3.2 Particle velocity distribution

The velocity of each particle was calculated from its echo, detected from the threshold, using quadrature demodulation [8] and autocorrelation [9]. Fig. 4 shows the average velocity distribution of the particles measured in 5 seconds. The velocity distribution is asymmetrical because the velocity in $x < 3$ mm is not measured correctly due to multiple reflections of the wall. Compared with the average particle velocities obtained from images, that obtained by the ultrasonic measurement is an appropriate result except for this region. The falling velocity of the aluminum sphere in the static water is about 0.4 m/s, but there is almost no difference in the particle velocity distribution between the updraft and downdraft pipes. And particle velocities are totally about 1 m/s lower than the

bulk flow velocity of the two-phase flow in the experiment, 3.4 m/s. This difference in velocities is the slip velocity between the two phases. These results suggest that the particle velocity is mainly determined by the liquid-phase velocity and the slip velocity, regardless of the direction of flow, in the case of such a high-velocity pipe flow.

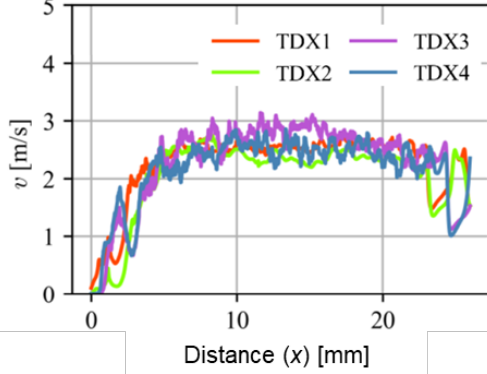


Figure 4: Average velocity distributions of particles.

3.3 Particle existence probability distribution

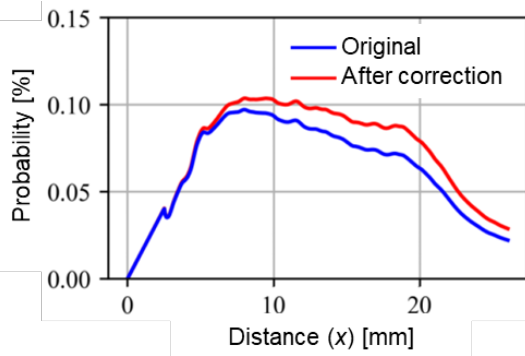


Figure 5: Particle existence probability distribution obtained from TDX2.

The blue line in Fig. 5 shows the ratio of the time when the echo from the particle is detected using the threshold during the measurement time for each position. Note that particle detection in $x < 3$ mm was not performed correctly due to multiple reflections and, therefore, linear interpolation was performed in this region as the zero probability of particle existence at the wall. In ultrasonic measurement, generally, the echo intensity from the particle becomes weaker as the distance from TDX increases. It is caused by the attenuation of the ultrasonic pulse in the medium and the reflection of the pulse by the particles on the front side. Even if the particle existence distribution is the same at all positions, the probability of particle detection decreases as the distance from the TDX increases due to the reasons described above. Therefore, a kind of correction is necessary to obtain the actual particle existence probability from the echography. We used two assumptions for the correction. One is that the probability of particle detection failure increases constantly with the distance from TDX. The other is that the existence distribution of particles is symmetrical with respect to the axis of the pipe. The red line in the figure shows the result

of correction using these assumptions and the echography. The corrected distribution is flatter than the existing distribution near the axis of the pipe. And since the values in this region are similar to $\alpha_S = 8\%$, it is supposed that this method is overall effective. However, the asymmetry still remains in spite of the correction. The reason of this is that the effect of multiple reflections near the wall could not be eliminated in the preprocessing, and the existence probability of particles near the wall decreased sharply.

3.4 Particle size distribution

Focusing on the particle echo in the echography as Fig. 6(a), we can find two echoes from one particle on one ultrasonic pulse emission. This is because the ultrasonic pulse was reflected at the front and back interfaces of the particle, respectively. What is interesting about these two echoes is that their phases are reversed as shown in Fig. 6(b), where C_C is the calculated value of the cross-correlation between the emitted ultrasonic pulse and each echo. When acoustic waves move from a medium with high acoustic impedance to a medium with low acoustic impedance, the phase of echo reflected at the interface is reversed because of a negative reflection rate $R < 0$ at the interface as shown in (c). In the opposite case, i.e. when a sound wave moves from a medium with a low acoustic impedance to a medium with a high acoustic impedance, the echo from their interface has the same phase as the Incident wave. Since the acoustic impedance of aluminum is higher than that of water, the echo from the back interface has the reversed phase and its C_C is negative.

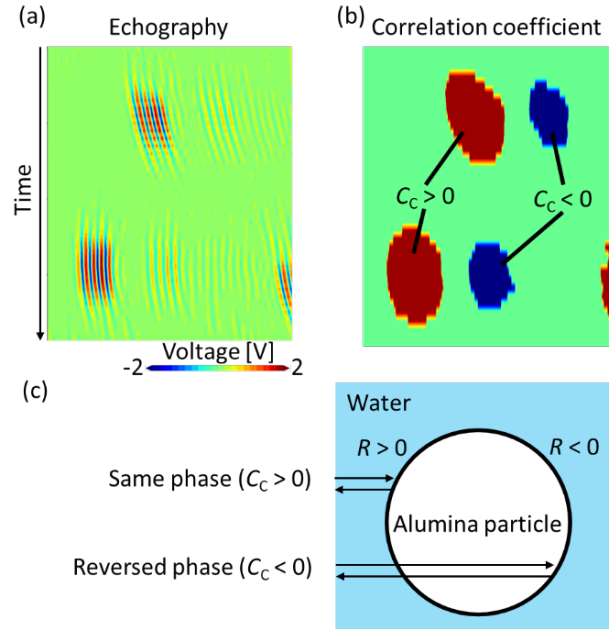


Figure 6: (a) echography zooming up near the echoes from particles, (b) cross-correlation between the emitted ultrasonic pulse and each echo, where values are ternarized, and (c) illustration of why one particle produces two echoes with different phases.

Fig. 7(a) shows a method to estimate each particle's diameter d . It is founded on the longest time interval between the start times of the phase-reversed pair Δt for

the estimation. In this experiment, since we already know the material of all particles is alumina, the particle diameter is possible to calculate from time interval by multiplying the speed of sound in alumina, i.e., $d = c_A \Delta t$. The distribution of particle diameter obtained from the estimation is shown in Fig. 7(b). Since phase-reversal pairs were not detected in all particles, the particle size distribution is shown here only for those in which pairs were detected. Although all particles injected in the fluid have actually the same diameter, 4 mm, the range of estimated diameters is in $d \leq 6$ mm. First, smaller diameters than 4 mm are caused by two reasons. One is that the center of the particle does not always pass through the axis of the measurement line. The effective diameter of the TDX used in this experiment is 5 mm, and if the particle's center passes within 4.5 mm from the axis, the particle is detected and its diameter is estimated. In principle, the particle diameter is estimated by this estimation method to be smaller as the particle center is farther from the axis. The reason for the overestimated particle diameter, i.e., $d > 4$ mm, is under investigation and a clear explanation cannot be given at this time. This underestimation is expected to reduce using statistics if we can grasp what kind of diameter distribution appears for a single particle size [10]. Since the cause of the overestimation is unknown, it is necessary to investigate the cause and the correction method in the future. Even though over- and under-estimations exist in this method, it is possible to grasp the order of particle size.

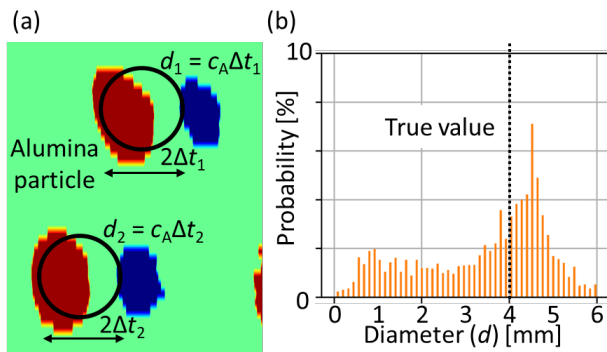


Figure 7: (a) a method to estimate a particle diameter and (b) a distribution of the estimated particle diameter.

Summary

In this paper, for the purpose of estimating the solid-phase flow rate in a solid-liquid two-phase pipe flow by the ultrasonic pulse echography, we tried to obtain solid phase information necessary for flow rate estimation from the echography. The information that was successfully acquired is the average advection velocity distribution, existence probability distribution and diameter distribution of the solid particles. First, only the echoes from the particles were extracted in the echography using a threshold for the echo intensity and we analyzed only those echoes. The particle velocities were calculated from the Doppler effect contained in the echoes. Although the flow velocity near the pipe wall could not be obtained due to multiple reflections on the wall, reasonable flow velocity

distribution was obtained in the other region. Also, when obtaining the existence probability distribution of particles, the probability of detecting particles far from the transducer decreases due to shadows of particles located near the transducer. To prevent this decrease, the distribution was corrected by assuming that the decrease occurs more in proportion to the distance and that the distribution is symmetrical to the pipe axis. The particle existence probability near the wall was lost due to the multiple reflection mentioned when obtaining the velocity distribution, and therefore it was not possible to correct it to be axially symmetrical. In spite of this asymmetry of the corrected distribution, since the existence probability obtained near the pipe center and the particle volume fraction given as the initial condition were almost the same. From this, it suggests that this measurement method is effective although there is a problem with the accuracy. The last, for particles whose front and back interfaces were detected in the echography, the diameter of each particle was calculated using the time of flight and speed of sound inside the particle. The measured diameter was obtained as a distribution from 0 to 1.5 times the actual diameter, and the peak in the diameter distribution appeared at a 13% larger diameter than the actual diameter. It means that this method can roughly estimate the particle diameter.

Acknowledgment

This work was supported by JSPS KAKENHI Grant No. JP21H04590.

References

- [1] Hein J, *et al.*: Deep-ocean mineral deposits as a source of critical metals for high- and green-technology applications: comparison with land-based resources, *Ore Geol. Rev.*, 51 (2013), 1–14.
- [2] Wang R, *et al.*: Slurry pumps in deep-sea mining: A review of numerical and experimental studies, *Ocean Eng.*, 251 (2022), 111150.
- [3] Shimizu K & Takagi S: Study on the performance of a 200 m airlift pump for water and highly-viscous shear-thinning slurry, *Int. J. Multiphase Flow*, 142 (2021), 103726.
- [4] Oddie G & Pearson JRA: Flow-rate measurement in two-phase flow, *Annu. Rev. Fluid Mech.*, 36 (2004), 149–172.
- [5] Hitomi J, *et al.*: Ultrasound Flow-monitoring and flow-metering of air-oil-water three-layer pipe flows, *IEEE Access*, 5 (2017), 15021–15029.
- [6] Murai Y, *et al.*: Ultrasound Doppler measurement of air-lift two-phase and particulate three-phase pipe flows, *Exp. Fluids*, 63 (2022), 126.
- [7] Yoon D, *et al.*: Ultrasound measurement of large bubbles rising in angled slug pipe flows, *Flow Meas. Instrum.*, 91 (2023), 102357.
- [8] Murakawa H, *et al.*: Effects of the number of pulse repetitions and noise on the velocity data from the ultrasonic pulsed Doppler method with different algorithms, *Flow Meas. Instrum.*, 40 (2014), 9–18.
- [9] Kasai C, *et al.*: Real-time two-dimensional blood flow imaging using an autocorrelation technique, *IEEE Trans. Sonics Ultrasonics*, 32 (1985), 458–464.
- [10] Park HJ, *et al.*: Spatial development of single void pulse in a horizontal turbulent bubbly channel flow investigated by a time-resolved two-laser measurement, *Int. J. Multiphase Flow*, 146 (2022), 103867.

Implementation of autocorrelation algorithm in VHDL for UVP instrumentation

Isadora Fernanda Zappe Schmidt¹, Fabio Rizental Coutinho¹, Andre Luis Stakowian², Cesar Yutaka Ofuchi², Marco Jose da Silva³, Flavio Neves Jr², and Rigoberto Eleazar Melgarejo Morales⁴

¹ Dep. of Electronics Engineering, Federal Univ. of Technology - Paraná (UTFPR), R. Cristo Rei 19, Vila Becker, Toledo, Parana, 85902-490, Brazil

² Graduate School of Electrical Engineering and Computer Science (CPGEI), Federal University of Technology - Paraná (UTFPR), Av. 7 de Setembro 3165, Curitiba, 80230-901, Parana, Brazil

³ Institute of Measurement Technology, Johannes Kepler University Linz, Altenberger Str. 69, 4040, Linz, Austria

⁴ Mechanical & Materials Engineering Postgraduate Program (PPGEM), Federal University of Technology - Paraná (UTFPR), Av. 7 de Setembro 3165, 80230-901, Curitiba, Parana, Brazil

Ultrasound velocity profiler (UVP) instrument can be applied in a variety of applications from industrial (oil, food processing, etc.), to environmental (hydrology, sewer, etc.) to energy (nuclear, hydropower plants, etc.). UVP equipment measures flow velocity using an autocorrelation method or phase-shift method. This method is established on the phase estimation for sequential ultrasonic pulses of a complex demodulated signal. The present work aims to implement in VHSIC Hardware Description Language (VHDL) a velocity estimation algorithm based on the autocorrelation method. First, the method was implemented in MATLAB® to be used as a reference. Then, the algorithm was implemented in VHDL in a MAX10 Field Programmable Gate-Array (FPGA) using the DE10-Lite Board from Terasic. The VHDL implementation process digitalized data using IEEE 754 standard floating-point number representation with single precision. Validation was performed using previous data acquired from a one-phase horizontal pipe flow. The algorithm implemented in VHDL presented a relative estimated velocity error below 0.00003%, consuming 4,623 total logic elements and 28 embedded multiplier elements from MAX10 FPGA.

Keywords: Ultrasound, Doppler effect, Flow measurement, Field programmable gate array, Phase-shift estimation

1. Introduction

Ultrasound Velocity Profiler (UVP) is a well-established method for liquid velocity measurements. It consists of measuring the Doppler effect observed in the echoes returned by a pulsed ultrasound wave [1]. The next step in the evolution of this technique is the use of multiple transducers for two-dimension velocity measurements or transducer arrays for velocity imaging applications. A field-programmable gate array (FPGA) is an integrated circuit capable of computing a high density of data with low latency. It is also very efficient for performing parallel processing of several channels. And it is also flexible enough to be applied at lower or higher computational demand applications. The phase shift or the use of an autocorrelator for estimating the Doppler velocity is the main computational demand of a UVP instrument. This work aims to describe the implementation of an autocorrelation method in VHSIC Hardware Description Language (VHDL) for use in a MAX10 Field Programmable Gate-Array (FPGA).

1.1 Background

The work of [2] presented an implementation of a pulsed wave Doppler ultrasound in a Virtex-5 FPGA. They estimated the velocity using a 128-point discrete Fourier transform implemented in Verilog language. It was reported that a total of 1,159 slice resources and 3,223 slice registers were required from the FPGA for the proposed

technique.

Another similar study is from [3], which was based on the Cyclone III FPGA family (Altera-Intel, San Jose, CA, USA). They implemented a Doppler frequency estimator that uses the peak and centroid of the power spectral density to compute velocity. It requires 10,308 logic elements for FFT computation running with a 105 MHz of clock frequency.

2. Methodology

2.1 Autocorrelation method theory

The autocorrelation algorithm is based on computing the phase for a set of ultrasound-pulsed emissions. The phase shift, φ , of the ultrasound echoes are directly related to the velocity component in the transducer axis direction by [4]

$$v_1 = \frac{c\varphi}{4\pi fT}, \quad (1)$$

where c denotes the sound velocity in the considered medium, f is the transducer central frequency and T is the period between emissions. The phase, φ , is estimated as the argument of the autocorrelation function, as [5, 6]

$$\varphi = \tan^{-1} \frac{Im[R(T)]}{Re[R(T)]}. \quad (2)$$

The input of the autocorrelation function is the IQ-demodulated ultrasound signal or the signal complex envelope [7]. Thus, the autocorrelator algorithm must process complex numbers, $r = x(n) + iy(n)$, where n denote the ultrasound emission number. The autocorrelation function for a set $N - 1$ ultrasound pairs of emissions is obtained by

$$R(T) = \frac{1}{N-1} \sum_{n=0}^{N-2} r^*(n)r(n+1), \quad (3)$$

where r^* denotes the complex conjugate of r .

2.2 Experimental set-up

VHDL algorithm was implemented in the DE-10 Lite board from Terasic. This hardware provides a large capacity MAX10 FPGA from Altera, which has up to 50,000 logic elements. It also features a 64MB SDRAM, an Arduino UNO R3 expansion connector, analog-to-digital converter, VGA output, etc. The system setup is shown in Fig.1. Digital data are provided to DE-10 Lite kit through a SPI interface. An Arduino UNO R3 board acts as a bridge between a PC and the FPGA board. In the SPI context, the Arduino is configured as the bus master and the FPGA as the slave. The MATLAB® Support Package for Arduino® Hardware was used to allow MATLAB to interactively communicate with the Arduino board. Previously acquired data from a real flow is loaded on Matlab environment which sends it to the DE-10 Lite board through an Arduino kit. The FPGA stores the data received in the SDRAM and then evaluates the autocorrelation function. In Matlab, the same computation performed in the FPGA is also done. The results obtained from FPGA are returned to the PC through SPI. Both results, from Matlab and FPGA, are compared to assess computation accuracy.

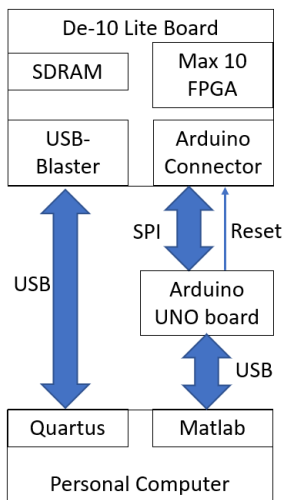


Figure 1: System set-up.

VHDL code is developed using Quartus Prime Lite Edition (version 18.1, from Intel). The code compiled is implemented at MAX10 FPGA through a USB connection. Since Eq. (1) comprises a multiply and accumulate computation, it was chosen to use a floating-point data representation to accommodate a large range of real values. At the FPGA, digital data was represented using 32 bits using IEEE 754 standard for single precision. The VHDL implementation of floating-point multiply and accumulate was based on [8]. In Matlab, it was chosen to use a 64 bits (or double precision) data representation since it will be used as a reference.

2.3 Autocorrelation implementation

The autocorrelation function was implemented in VHDL language as depicted in Fig. 2. Data is received from Arduino by the SPI controller. Arduino UNO was set up as an SPI master with a clock polarity and phase at high level. The interface was configured to transfer 16 bits of data at each transfer with a 20 MHz clock. Data from SPI controller is buffered and sent to be stored in SDRAM through the Write SDRAM module (Fig. 2). When a total of N ultrasound emissions are stored, the autocorrelator begins to read the first ultrasound emission sample then applies Eq. 3. This calculation is repeated for the next emission until it reaches the $N - 1$ emission. The result from the autocorrelator is sent from SPI to Matlab(PC) for comparison purposes.

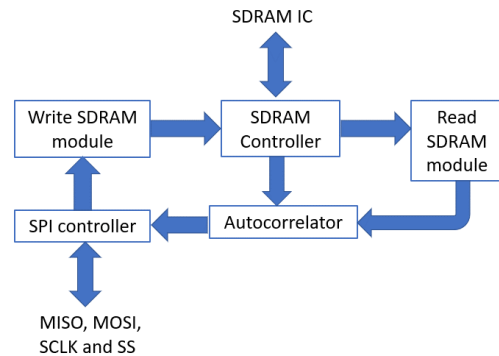


Figure 2: VHDL software block diagram.

Initialization, read and write low-level operations at SDRAM are performed by the SDRAM controller. This module used an open-source code from [9]. The SPI controller was responsible for the SPI communication. It also concatenates each pair of 16 bits of data to form 32 bits single precision word. The Write SDRAM module is responsible for buffering and issuing a write command for the SDRAM. The data for the autocorrelator is delivered by the Read SDRAM module which control the requests of readings and buffering.

The autocorrelator block consist of a state machine that control the order of execution and two VHDL components: a floating-point multiplication (`fp_mul`) and a floating-point summation (`fp_add`) component (Fig. 3). These components are instantiating 4 times in VHDL to implement the Eq. 3 as depicted in Fig. 3. The simplified

autocorrelator state machine (Fig. 4) comprises of 5 states. In the first state, the autocorrelator is waiting for a start signal which is issued by SDRAM controller after all the data are correctly stored. At state 1, the next sample, $r(n+1)$, is read at SDRAM. At the first execution $r^*(n)$, R_p and I_p are loaded with zero values. At state 2, the process depicted in Fig. 3 is executed. At state 3 it is checked if the $N-1$ ultrasound pairs of emissions were reached. If not, the content of R_SUM and I_SUM are shifted to R_p and I_p , respectively, and the content of $r(n+1)$ is shifted to $r(n)$. Reaching the end of emissions, the results of R_SUM and I_SUM are sent to the SPI controller.

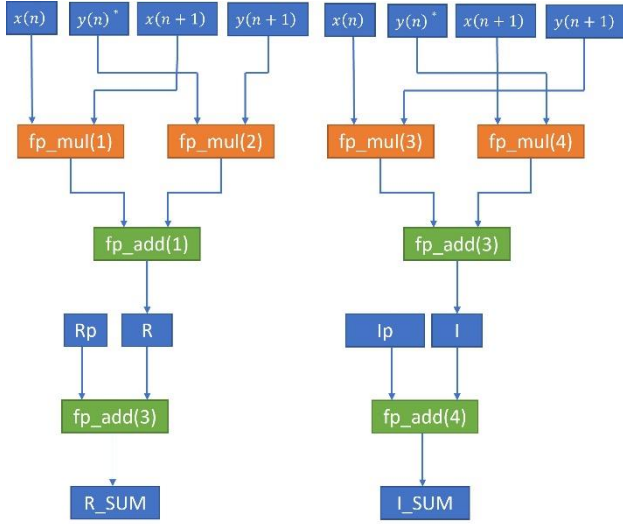


Figure 3: Multiply and accumulate component diagram.

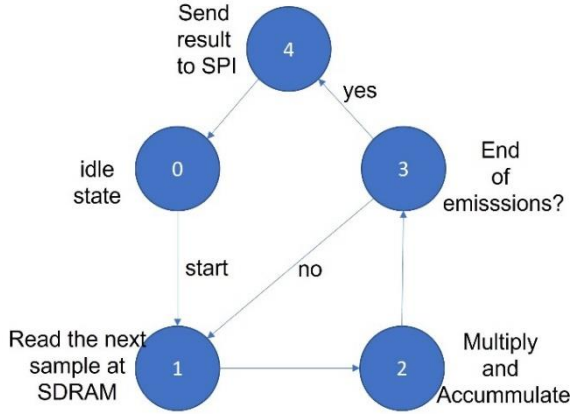


Figure 4: Autocorrelator state diagram.

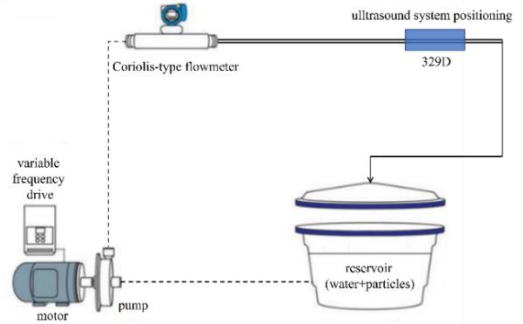
2.4 Flow apparatus

Input data, used for evaluating the FPGA autocorrelator, were obtained through a pipe flow experiment as shown in Fig. 5. In the experiment, the centrifugal pump – driven through an inverter of variable frequency – circulates the liquid in an acrylic tube whose inner diameter is of 25.9 mm (D). A trace powder with a 1.07 g/cm^3 density was added to the reservoir at a concentration of 4 g/L. Water flow is measured by a Coriolis-type flow meter. A 4 MHz ultrasound transducer (Met-flow S.A, TX4-5-8) was positioned at $329D$ from the pipe entrance. It was coupled

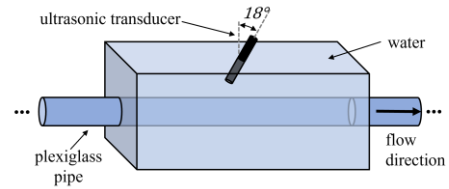
with a box filled with water and it was angled by 18° to the pipe normal (Fig. 5b).

Data acquisition was performed with a PXI System from National Instruments, model NI5752R. This system can acquire data at 50 Msamples/s and store data for offline processing. A pulse repetition frequency of 6,005.99 Hz was set-up. A mean flow velocity of 1.0 m/s was adjusted in the flow for the data collection.

Velocity processing is done offline using Matlab environment. Each velocity was measured using 128 emissions Data acquired from each emission was IQ demodulated [7]. After demodulation, the digitized data was filtered by a matched filter centered in 4 MHz and 4-cycles pulse. Finally, it was converted to a double precision (64 bits) at Matlab environment to be used as a reference. For FPGA processing data precision were reduce to 32 bits (single precision).



(a)



(b)

Figure 5: (a) Flow apparatus. (b) Ultrasound system positioning

To assess the accuracy of the proposed method, three range gates or depths $\{0.027D, 0.054D, 0.5D\}$, with $D=25.9$ mm, were chosen as shown in Fig. 6. The FPGA processor only calculates the autocorrelation value, thus velocity estimated by the FPGA is evaluated at Matlab using the autocorrelation values computed by the FPGA, using Eq. (1) and Eq. (2).

3. Results

The results shown in Tables 1 and 2 were the autocorrelation evaluation and velocity obtained with the data from the FPGA processor. The relative error between the estimates from FPGA and Matlab was very small, below 0,00003%. Thus, indicating that the proposed method is feasible to be used in terms of accuracy. This small relative error shown in Table 1 is because the autocorrelation performed by MATLAB® considers

double precision number representation (64 bits) whereas the FPGA algorithm uses single precision representation (32 bits). Velocity data estimated also show a very good agreement, (Table 2).

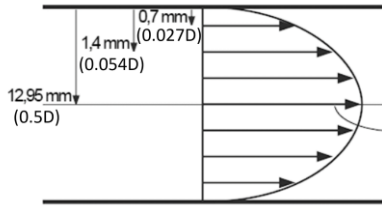


Figure 6: Range gates depths analyzed.

In terms of FPGA resources, a total of 4,623 logic elements were used (Table 3). Considering only the autocorrelation implementation, 4,123 logic elements and 352 registers were required (Table 3). Since MAX10 FPGA has 49,760 logical elements, the implementation used approximately 9.3% of the total logic elements of the integrated circuit. Considering the embedded multiplier elements, MAX10 has 288 9-bit multiplier elements. Thus, approximately 10% of the embedded multiplier (Table 3) was used in the proposed method. Compared with the results from [3], this implementation can estimate velocity with less than half of the FPGA resources. To compute the autocorrelation function, the FPGA spent 15 clock cycles for each emission. This is equivalent to spending 0.3 μ s for each emission (for a 50 MHz clock). Considering the experimental setup condition used (128 emissions), the computation of the autocorrelation function will spend 38.4 μ s.

Table 1: Accuracy results of the VHDL autocorrelator.

Depth (mm)	Relative Error - real part (%)	Relative Error - imaginary part (%)
0.7	$+1.633 \times 10^{-5}$	-1.265×10^{-5}
1.4	-2.419×10^{-5}	-1.498×10^{-6}
12.95	$+2.514 \times 10^{-5}$	5.746×10^{-6}

Table 2: Accuracy results from velocity.

Depth (mm)	Velocity Matlab (m/s)	Velocity FPGA (m/s)	Relative error (%)
0.7	0.52074182	0.52074176	-1.152×10^{-5}
1.4	0.78348715	0.78348714	-1.276×10^{-6}
12.95	1.08836469	1.08836460	-8.269×10^{-6}

Table 3: FPGA resources used.

Entity	Total Logic Elements	Total Registers	Embedded Multiplier 9-bit elements
Autocorrelator	4,123	352	28
SDRAM	417	267	0
SPI controller	83	97	0
Total	4,623	716	28

4. Summary

In this work, an autocorrelation method for the measurement of fluid flow velocity was implemented in VHDL for FPGA processing. The data processed was represented using a floating point (IEEE 754 standard) with single precision (32 bits). The proposed technique presented a very small relative error regarding autocorrelation or velocities estimation. Due to this, as future work, we recommend assessing the accuracy of a half-precision floating-point data representation (16 bits). Using fewer bits for data representation will imply using less FPGA resources and optimized hardware.

The implementation proposed used approximately 9.3% resources of the MAX10 FPGA. This result shows that this hardware may be capable of processing up to 10 ultrasound transducers simultaneously.

4. Acknowledgments

This work was carried out with the support of the following Brazilian agencies: Fundação Araucária de Apoio ao Desenvolvimento Científico e Tecnológico do Paraná (grant 026/2020) and CNPq – Conselho Nacional de Desenvolvimento Científico e Tecnológico (grant 406881/2021-9 – Chamada CNPq/MCTI/FNDCT N°18/2021, Faixa A - Grupos Emergentes). The authors are grateful for their support.

References

- [1] Takeda Y: Ultrasonic Doppler fluid flow, Springer, (2012).
- [2] Page A and Mohsenin T: An efficient & reconfigurable FPGA and ASIC implementation of a spectral Doppler ultrasound imaging system, IEEE 24th Int. Conf. on Application-Specific Sys., Arch. and Processors, 42(4), (2013), 198-202.
- [3] Ricci S and Meacci V: FPGA-Based Doppler Frequency Estimator for Real-Time Velocimetry, Electronics, 9(456), (2020).
- [4] Ofuchi C Y *et al.*: Extended Autocorrelation Velocity Estimator Applied to Fluid Engineering, ISUD 9, (2014), 109-112.
- [5] Kasai C, *et al.*: Real-time two-dimensional blood flow imaging using an autocorrelation technique, IEEE Trans. on Sonics and Ultras., SU-32(3), (1985), 458-464.
- [6] Loupas T, *et al.*: An axial velocity estimator for ultrasound blood flow imaging, based on a full evaluation of the Doppler equation using a two-dimensional autocorrelation approach, IEEE Trans. on Ultr., Fer., and Freq. Ctrl, 42(4), (1995), 672-688.
- [7] Haykin S: Communications Systems, John Wiley & Sons Inc, New York (2001).
- [8] Deschamps J P, *et al.* Guide do FPGA implementation of arithmetic functions, Springer, Dordrecht, 2012.
- [9] Placha, A SDRAM controller, open-source code, 2019. <https://github.com/Arkowski24/sdram-controller>.

Fundamental Study of Superimposed Image Flow Visualization using UVP

Yutaka Namiki¹, Tatsuya Nakada², Naruki Shoji³, Hideharu Takahashi⁴ and Hiroshige Kikura¹

¹ Lab. for Zero-Carbon Energy, Tokyo Institute of Technology, 2-12-1-N1-7, Ookayama, Meguro-ku, Tokyo 152-8550, Japan

² Ltd. Sony Semiconductor Solutions Group, 4-14-1, Asahi-chou, Atsugi, Kanagawa, 243-0014, Japan

³ Muroran Institute of Technology, 27-1, Mizumoto-chou, Muroran, Hokkaido, 050-8585, Japan

⁴ Mech. Engin., Tokyo Institute of Technology, 2-12-1, Ookayama, Meguro-ku, Tokyo, 152-8550, Japan

The Fukushima Daiichi Nuclear Power Plant accident at TEPCO Holdings, Inc. caused by the earthquake and tsunami has had a major impact on nuclear energy policy. However, Japan needs nuclear power generation in the future because of its fragile energy supply structure, and further safety improvement of power plants is required to restart operations. In existing power plants, fluid flow monitoring in pipes is indispensable because of the erosion and corrosion caused by fluid flow, which leads to defects and wall thinning in the pipes, and early detection of abnormalities in the piping system before pipe rupture. Therefore, the purpose of this study is to develop a flow visualization system to improve safety. The system visualizes the flow field by superimposing images of the flow field measured by the ultrasonic velocity profiler method (UVP) and images of the measurement location taken by a camera. Visualization and measurement of the flow in a circular pipe flow were conducted using this system. The results showed that the relative error between the distance from the starting point of the measurement to each measurement point in the image and the distance of the velocity distribution measured by UVP was about 5%. It indicates the effectiveness of the system.

Keywords: UVP, Pipe flow, Smartification.

1. Introduction

The Fukushima Daiichi Nuclear Power Plant accident at TEPCO Holdings, Inc. caused by the earthquake and tsunami has had a major impact on nuclear energy policy, including the decommissioning and shutdown of nuclear power plants. However, Japan's energy supply structure is fragile, and nuclear power generation, which can be utilized as a base power source, is necessary in the future. To restart nuclear power plants, further safety improvement of nuclear power plants is required. In addition, it is necessary to promote energy policies that consider global environmental issues to realize a sustainable society. Therefore, maintaining the integrity of existing power plants using renewable energy and nuclear power plants and ensuring the safety of future power plants are the most important issues. In power plants, fluid flow monitoring in pipes is essential for nondestructive and early detection of abnormalities in the piping system before pipe rupture, because fluid flow in pipes causes erosion and corrosion, which leads to defects and wall thinning in pipes. Shoji et al. have been conducting research on the development of a measurement system using the ultrasonic velocity profiler method (UVP method) [1], which enables non-destructive and non-invasive measurement of the flow field in piping and have developed a portable UVP device that integrates the necessary hardware elements [2]. This technology is highly compatible with small display devices due to its portability and simplicity and can be easily combined with devices such as smart glasses to realize hands-free

inspections, thus contributing to more efficient piping inspections. Therefore, in this study, we constructed a system in which a superimposed image of the flow velocity distribution measured by UVP, and an image of the measurement target taken by a camera are superimposed and then projected onto smart glasses and verified the operation by measuring the flow velocity distribution in pipes to examine the feasibility of the system.

2. Development of an automatic superimposition system for flow velocity distribution

In realizing this system, the accuracy of the sensor position and angle, the thickness of the piping, and the sound velocity are important parameters to consider. Sensor position and angle are factors that have a direct impact on position and velocity accuracy, and piping conditions are of high importance because sound refraction can change the measurement position and the system must automatically determine whether to use longitudinal or transverse propagation mode conversion accordingly. This study focused specifically on methods for automatic detection with respect to the sensor's position. It is assumed that the camera is attached to the head of the measurement person, and it is expected that the image superimposed position will be shifted frequently due to shaking, so the development of a system to improve this is required. Therefore, to improve the misalignment of the image superimposition position, we develop an automatic flow velocity distribution superimposition system.

2.1 System configuration

A flow visualization system was constructed to visualize the flow in a pipe. Figure 1 shows a schematic of the system and Figure 2 shows the system configuration. Table 1 shows the specifications of the equipment used in this system. The person taking measurements in this system wears a device with a USB camera attached to smart glasses on his or her head and carries a device for UVP measurement and a PC for image processing in his or her hand. At the same time, the UVP device in the hand acquires the flow velocity distribution information of the measurement target and sends it to the PC, which creates a superimposed image of the measurement target and the flow velocity distribution information and projects it on the small display of the smart glasses. This allows the user to visualize the velocity distribution information obtained by the UVP device on the measurement target via the Smart Glasses display. The UVP device is a portable device (150 mm long, 120 mm wide, and 60 mm high) [2] developed by Shoji et al. A sensor holder (Figure 3) is attached to the tip of the ultrasonic transducer to enable measurement of the flow velocity distribution at any position.

2.2 Acquisition of flow velocity distribution information

Experiments were conducted to measure circular tube flow. Figure 4 shows a schematic of the experimental apparatus used in this experiment. A transparent vertical circular tube (inner diameter 30 mm, made of acrylic) was used for the basic study of the system to enable future comparison with optical visualization and measurement methods. Nylon particles with an average diameter of 80 μm and a specific gravity of 1.02 (made of nylon 12, nylon powder WS200P, Nippon Laser Co., Ltd.) were dispersed in water stored in a tank as a reflector of ultrasonic waves, and a pump was used to generate an upward flow circulating through the acrylic pipe. An ultrasonic transducer (8 mm in diameter, 4 MHz center frequency) was placed acrylic pipe to measure the velocity distribution in the pipe from ultrasonic pulses reflected by reflectors. A liquid gel was inserted between the acrylic pipe and the ultrasonic transducer to prevent reflection of ultrasonic waves on the pipe surface. The flow rate in the piping, the incident angle of the ultrasonic beam, the setting conditions of the UVP device, and the Reynolds number of the flow field are shown in Table 2. Note that in this study, the frame rate on the UVP side is lower than that of the camera, so the images are updated according to the UVP time. However, there may be cases where the UVP frame rate is higher depending on the settings. In such a case, adjust the image update to match the frame rate of the camera side.

2.3 Detecting the measurement position

This section describes the development of an automatic superimposition system for flow velocity profiles. To determine the position of the superimposed image of the flow velocity distribution, it is important to detect the position of the ultrasonic transducer in the captured image. Color tracking is one of the methods to detect the position of an object in an image [3]. In this system, the sensor

holder is colored in an arbitrary color, and the measurement position is obtained by detecting the color of the sensor holder in the captured image.

The sensor holder used in this system is colored red at the tip, and the measurement position is obtained by generating a mask image in which only the sensor holder is extracted from the captured image by color detection, as shown in Figure 5. To detect the sensor holder in the mask image, the image of the measurement target is converted to HSV color space (Hue, Saturation, and Value), and only color components in the HSV range are extracted. The position of the sensor holder was then estimated by extracting the area with the largest area within the extracted color range.

2.4 Automatic superimposition method of flow velocity distribution

Figure 2 shows the configuration of the automatic superimposition system for flow velocity distribution. In this system, a PC processes the captured images and measured flow velocity distribution to create an image of the superimposed flow velocity distribution on the measurement target. The image is then projected onto the display of the smart glasses to visualize the flow information of the measurement target. At this time, a portion of the screen of the application used for UVP measurement is captured to be used as the flow velocity distribution measurement image. First, a mask image is created by extracting the sensor holder from the image of the measurement target. Then, taking advantage of the fact that the dimensions of the sensor holder are known, the relationship between the dimensions of the sensor holder in the image (number of pixels) and the actual dimensions of the image captured by the camera (mm) is obtained from the size of the sensor holder in the mask image. Let y_{pv} be the number of pixels of the vertical width of the sensor holder position obtained from the mask image, x_{ph} be the number of pixels of the horizontal width, y_v be the vertical dimension of the sensor holder, and x_h be the horizontal dimension, and let y_{ts} and x_{ts} be the conversion factors for the vertical and horizontal dimensions, respectively.

$$y_{ts} = \frac{y_{pv}}{y_v}, x_{ts} = \frac{x_{ph}}{x_h} \quad (1)$$

The conversion coefficients were averaged. These were averaged to obtain the Conversion Factor (CF) between pixels and actual size.

$$CF = \frac{y_{ts} + x_{ts}}{2} \quad (2)$$

In this study, CF was determined based on the dimensions of the holder, but in principle it is sufficient if an object with known dimensions exists in the image. Therefore, whether the holder is square or trapezoidal, it can be mapped to the holder by attaching a sticker or marker to it. Next, based on the relationship between pixels and actual

dimensions, the flow velocity distribution measurement results are scaled to the appropriate dimensions. The appropriate distance where the velocity distribution exists from the sensor holder is calculated considering the previously obtained dimensions of the wall surface to be measured. Finally, the velocity distribution measurement results obtained by the UVP device are scaled and positioned to the appropriate dimensions in the image taken of the measurement target, and a superimposed image of the velocity distribution is created.

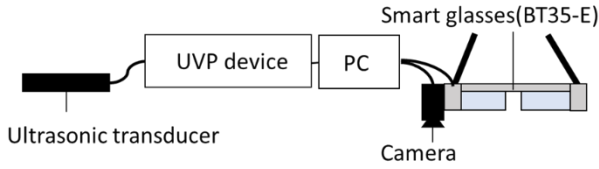


Figure 1: Flow visualization system overview

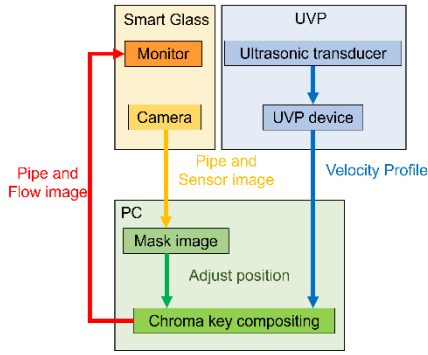


Figure 2: Configuration of automatic superimposition system of flow velocity distribution

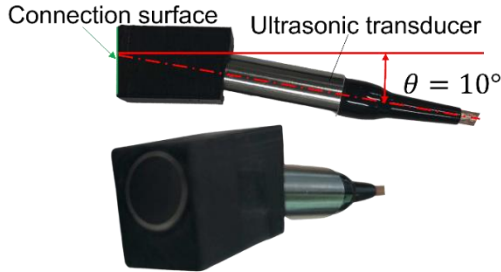


Figure 3: Sensor holder for ultrasonic transducers

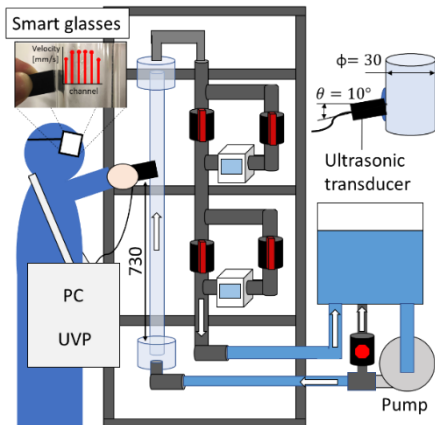


Figure 4: Schematic of flow measurement of circular tube flow

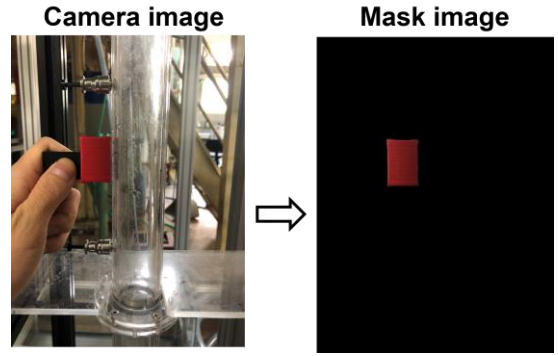


Figure 5: Mask image of sensor holder detected from camera image.

Table 1: List of equipment used in flow visualization systems.

Equipment	Model number, Maker	Specification
Smart glasses	BT35-E, EPSON	Resolution: 1280 × 720
USB camera	CM02, SROSS	Resolution: 1920 × 1080 Flame rate: 30 fps

Table 2: Measurement conditions for flow visualization system operation experiments

Flow rate	20 L/min
Ultrasonic center frequency	4 MHz
Angularity of incidence of ultrasonic waves	10 °
Pulse repetition frequency	2 kHz
Number of pulse repetitions	128
Sound velocity(25°C)	1497 m/s
Spatial resolution	0.75 mm
Time resolution	64 ms
Reynolds number	3900

3. Basic study test on system feasibility

Experiments were conducted to verify the operation of this system. Figure 6 shows the experimental system. PC acquires the image of the sensor holder captured by the USB camera and displays a sample image of the flow velocity distribution measured by the UVP device on the PC display. PC acquires the flow velocity distribution measurement result by searching for the result image from the window name. The PC calculates the relationship between the actual dimensions and the number of pixels in the image and the appropriate display position of the flow velocity distribution by creating a mask image from the sensor holder image using color detection. After that, the measured velocity distribution is scaled down and a superimposed image with the sensor holder is created. Table 3 shows the dimensions of the colored part of the sensor holder, the thickness of the pipe to be measured, and the threshold values for color detection, which were given when positioning the superimposed image in this operation

verification experiment.

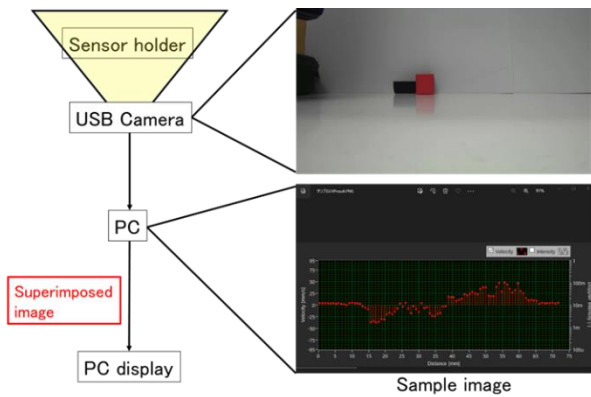


Figure 6: Schematic of the operation verification experiment of the automatic superimposition system

Table 3: Experimental conditions for verifying the operation of the automatic superimposition system.

Dimensions of the colored part of the sensor holder	20 mm × 30 mm
Thickness of piping	3 mm
Color detection threshold (HSV color space)	H:0 ~ 10, S:80 ~ 255, V:0 ~ 255

4. Experimental results and discussion

Figure 7 shows the results of an experiment to verify the operation of this system. Based on these results, we succeeded in developing a system that automatically determines the position of the sensor holder by color detection, scales the flow velocity distribution measurement results based on the dimensions of the sensor holder, and automatically superimposes them on the image taken of the sensor holder. The system automatically superimposed the measured velocity distribution on the image taken by the sensor holder after scaling it based on the dimensions of the sensor holder. The results of 150 superimposed images (5 seconds at 30 fps) measured with a scale in the background of the superimposed images showed that the relative error between the measured distance (mm) on the horizontal axis and the measured velocity distribution was within 5%. This system scales the flow velocity distribution based on the number of pixels in the captured image and the dimensions of the sensor holder, so when the resolution is low or the occupancy rate of the sensor holder in the captured image is low, the accuracy of the conversion coefficient between image pixels and actual dimensions: CF is reduced. To solve this problem, it is possible to increase the occupancy ratio of the sensor holder in the captured image by using a high-resolution camera or by increasing the size of the sensor holder. And regarding the time lag between measurement and display, currently a relatively simple algorithm is used to detect the sensor position, and thus the delay is on the order of a few milliseconds. However, in the future, it is expected that algorithms will become more sophisticated and that more parameters will be considered in the correction process, which may result in an increase in processing volume.

Thus, optimization will be required.

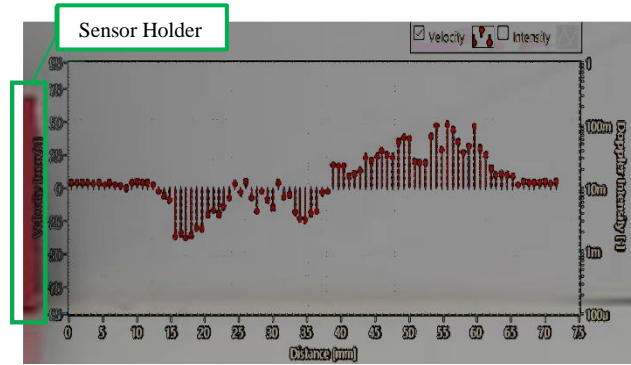


Figure7: Result of operation verification experiment of automatic superposition system

5. Summary

We developed a flow visualization system that utilizes a flow velocity distribution measurement method by UVP and AR technology using small display devices such as smart glasses. An automatic superimposition system of the flow velocity distribution was developed to improve the effect of camera shaking, and experiments were conducted to verify the operation of the system. As a result, we succeeded in automatically superimposing the flow velocity distribution and the camera image of the measurement target by scaling and positioning the flow velocity distribution based on the dimensions of the sensor holder. The relative error between the flow velocity distribution and the actual dimensions was within 5%, and the superimposition of the flow velocity distribution followed the sensor holder's position, thus reducing the influence of camera shaking. In conclusion, the development of the flow visualization system has shown the possibility of solving the problem of requiring expert knowledge to determine the measurement position of the flow velocity distribution in flow velocity distribution measurement by UVP, and of improving piping inspection in narrow spaces in power plants and plants by making it hands-free.

References

- [1] Takeda Y: Velocity profile measurement by ultrasound Doppler shift method. Int. J. Heat and Fluid Flow, Vol.7, No.4 (1986), pp.313-318.
- [2] Shoji N, *et al.*: Development of Advanced UVP Instruments Applicable to 3-D Velocity Vector Measurement. ISUD, (2021), 1-4.
- [3] Sugaya Y, *et al.*: Basic Investigation into Hand Shape Recognition Using Colored Gloves Taking Account of the Peripheral Environment, Human Interface and the Management of Information, (2013), 133-142.

Coupling of in-line UVPPD rheometry and USDMA for process control in polymorph crystallization processing of chocolate confectionery masses

Erich Windhab¹, Kim Mishra², and Lucas Grob³

¹ Lab of Food Process Engineering (FPE/IFNH); ETH Zürich, Schmelzbergstrasse 9; CH-8092 Zürich

² Planted Foods AG; Kemptpark 32-34, CH-8310 Kemptthal; Switzerland

³ Swiss Food Research; Schmelzbergstrasse 9; CH-8092 Zürich

The Ultrasound Velocity Profile Pressure Difference (UVPPD) method has proved to be a powerful in-line measuring technique for non-invasive flow mapping and characterization of Non-Newtonian fluid rheology in processing flows. Crystal melt suspensions (CMS) are yield stress shear thinning fluids in which crystal network formation is responsible for the appearance of a yield stress. CMS were made from different confectionery fat systems. UVPPD measurements were applied to determine the yield stress τ_0 , as indicator of crystal network formation during following processing steps: (1) pre-crystallization, (2) micro-foaming, (3) 3D-printing and (4) molding, cooling and de-molding, being key operations in the chocolate confectionery manufacture. The coupled application of Ultrasound Dynamic Mechanical Analysis (USDMA) based on ultrasound attenuation comes into preferable consideration when the material characteristics switches from concentrated crystal suspension to a solid to detect fat crystal network formation during solidification. This was addressed for 3D-printed and molded chocolate masses upon cooling. With an ETH-FPE developed in-line sensing USDMA setup (DETACHLOG) we managed to correlate viscous and elastic moduli (G'' , G') with crystal network structure formation. Moreover, it was possible to sharply detect the impact of the molded mass contraction during solidification and its subsequent detachment from the mold walls.

Keywords: Ultrasound-Doppler, Ultrasound Attenuation, in-line rheometry and dynamic mechanical analysis, mold wall detachment detection, process control for crystallization, foaming, 3D-Printing and cooling

1. Introduction

The flow behaviour and material characterization of yield stress fluids containing crystals play a major role in lipid (fat/oil), polymer, metal or magma melts as well as in concentrated dispersion systems. They have in common that a liquid (melt or solution) and solid (crystal) may coexist under given temperature conditions. From a rheological perspective, cooling a melt below its crystallization temperature or a solution below a temperature at which supersaturation reaches a critical value, crystal formation transforms the fluid system from a Newtonian fluid to a non-Newtonian suspension or a semisolid body. Rheology-structure relationships of crystallizing fluid systems are mostly quite complex since the crystal structure and formation kinetics can be altered by shear stress and related viscous friction-based energy dissipation acting in shear flow fields. Accordingly, thixotropy or rheopexy can be superimposed with related characteristic time scales depending on shear stress and energy dissipation rates as well as on the generated crystal shape and morphology. Such complex relationships are often poorly understood despite their relevance in applications of lipid, polymer or metal, melt flow. Theoretical and experimental studies investigating lipid melt rheology were found to resemble each other. Recently, efforts have been made to introduce gas bubbles into lipid systems. Such systems are denoted as lipid foams. Most studies of such relate foam formation of lipid systems to the presence of crystals. Several stabilization mechanisms are proposed such as pickering stabilization, viscoelastic gel formation of the continuous phase, and jamming of crystals between bubbles. Confectionery fats are natural

mixtures of high melting and low melting triglycerides. Micro-foaming of chocolate confectionery has become a novel and interesting developing domain aiming for a new class of low energy density chocolate confectionery [1,2]. This requires improved characterization of confectionery fat crystal structure formation and the development of related rheological and mechanical properties during (i) pre-crystallization, (ii) micro-foaming, (iii) 3D-printing/molding and (iv) cooling processes, for which the ultrasound based UVPPD & USDMA were adapted and successfully tested. Industrial implementations are under development.

2. Experiments and modelling

2.1 In-line rheometry in crystallization process

The UVPPD measurements were done directly after pre-crystallization. Double mantled 15 mm pipes held at 27 °C were used to convey the crystal melt suspension. The pressure difference was measured in a 3.29 m pipe section. A diaphragm pressure sensor (CC1020, Labom GmbH, Hude, Germany) with a measurement range of 1.0–1.4 bar absolute pressure was used at the beginning of the pipe segment in order to calculate the pressure difference against atmospheric pressure at the pipe exit. In between the pressure sensor and the end of the pipe segment a custom, built polyvinyl chloride cell with inserted ultrasonic transducers was used to record the velocity profile. Two 4 MHz transducers (Imasonic SAS, France) with an active diameter of 5 mm were placed at 60° and 90° angle with respect to the flow axis in order to determine the velocity profile across the pipe diameter and the speed of sound consecutively. The transducers were preferably operated at 3.75 MHz with a pulse repetition frequency of 750 Hz and

128 repetitions. The signals of the transducers were recorded with the UB-Lab device (Ubertone, Schiltigheim, F). During approximately 60 s, a total of six averaged profiles were recorded for one process setting. This procedure was repeated three times for each process setting. Subsequently, the profiles were deconvoluted and fitted with a Herschel-Bulkley model [3-5]. Fitting the Herschel-Bulkley model onto the measured velocity profile requires pipe radius R , plug radius R_p , pipe length L_p , flow index n , and consistency factor K as parameters:

$$\nu_{HB}(r) = \begin{cases} \frac{n}{n+1} \frac{\Delta P}{2L_p K}^{1/n} [(R - R_p)^{1+1/n} - (r - R_p)^{1+1/n}], & \text{if } r \geq R_p \\ \nu_{HB}(R_p), & \text{if } r < R_p \end{cases} \quad (1)$$

The fitted plug radius R_p is related to the yield stress of the CMS as follows:

$$R_p = \frac{2\tau_0 L_p}{\Delta P} \quad (2)$$

Consequently, the larger R_p and ΔP , the higher the yield stress τ_0 of the CMS. The instrumentation diagram for the crystallization and micro-foam processing including the UVPPD in-line measuring cell can be seen in Figure 1.

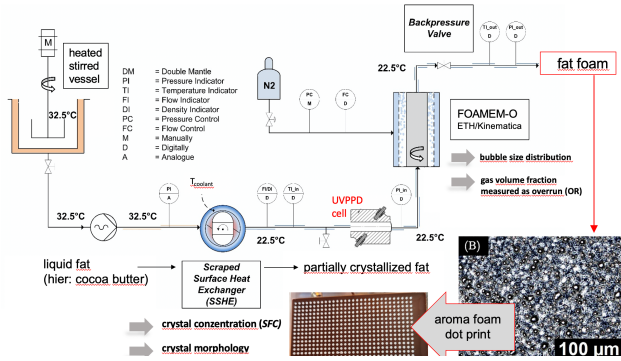


Figure 1: Processing setup for the processing of 3D-printed micro-foam structures from pre-crystallized fat crystal suspensions

Figure 2 shows further details of the UVPPD cell arrangement while Figure 3 demonstrates measured velocity profiles for various crystallization intensity and respectively derived yield values $\tau_{0,i}$.

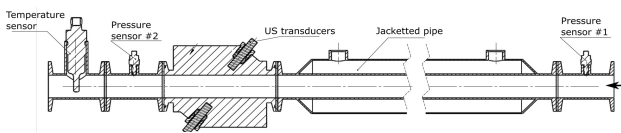


Figure 2: Arrangement of US and pressure transducers in the UVPPD measuring cell and p,T sensors in the related pipe section

The velocity profiles in Figure 3 were measured for cocoa butter melt suspensions (CB CMS) crystallized at apparent shear rates in the surface scraped heat exchanger of $\dot{\gamma}_{SSHE} = 2150 \text{ s}^{-1}$ for varying crystal volume fraction Φ_{SFC} . At low Φ_{SFC} an almost parabolic velocity profile is apparent. At $\Phi_{SFC} = 2.66 \%$ a center plug is forming indicating the onset of a yield stress. With further increasing Φ_{SFC} the

plug flow domain extends further towards to the pipe wall. At $\Phi_{SFC} = 8.80 \%$, the plug extends almost the whole pipe radius denoting the upper yield stress limit at the given measurement conditions.

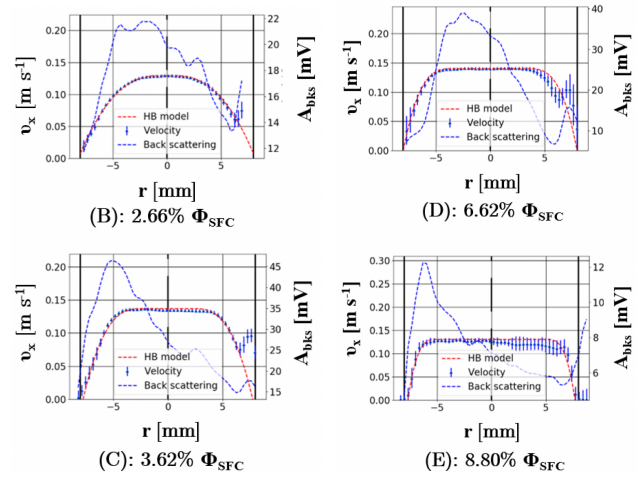


Figure 3: The fluid velocity in x-direction v_x on the left y-axis and the back scattering amplitude A_{bks} on the right y-axis as function of the pipe radius r for CB CMS crystallized at $\dot{\gamma}_{SSHE} = 2150 \text{ s}^{-1}$ for various crystal volume fractions Φ_{SFC} . The lines emerging from the velocity profile points indicate the magnitude of uncertainty. The dotted red line indicates a fitted velocity profile according to the model proposed by Herschel and Bulkley.

Yield values as derived from the centre plug radii of the velocity profiles are presented in Figure 4 together with micrographs from polarized light microscopy of the resulting crystal structure.

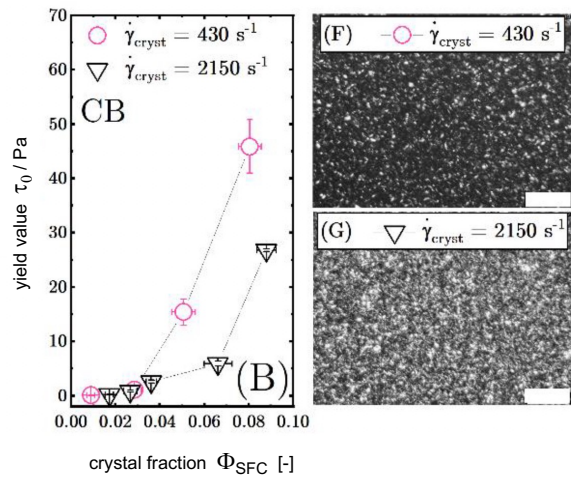


Figure 4: Left: Yield stress τ_0 as function of the crystal volume fraction Φ_{SFC} for CB, crystallized at $\dot{\gamma}_{SSHE} = 430 \text{ s}^{-1}$ & 2150 s^{-1} . (F,G) to the right displays of polarized light microscopy images of the respective CMS for both crystallization shear rates. Bar represents $100 \mu\text{m}$ [7].

As can be taken from Figure 4, crystallizing at increased shear rates leads to lower yield values in the CB system due to the generation of smaller crystals with reduced connectivity (network formation) expected to result from the increase viscous energy dissipation at higher shear rate. Yield stress τ_0 as a function of solid fat content Φ_{SFC} for

another fat melt system (palm kernel oil melt suspensions, PKO CMS) chosen as best reference fat base for chocolate confectionery fillings, was measured and resulting functional dependencies of $\tau_0(\Phi_{\text{SFC}})$ approximated with the structure model function given by equation 3:

$$\tau_0 = \frac{6\gamma}{a} \Phi^{1/(3-D)} \quad (3)$$

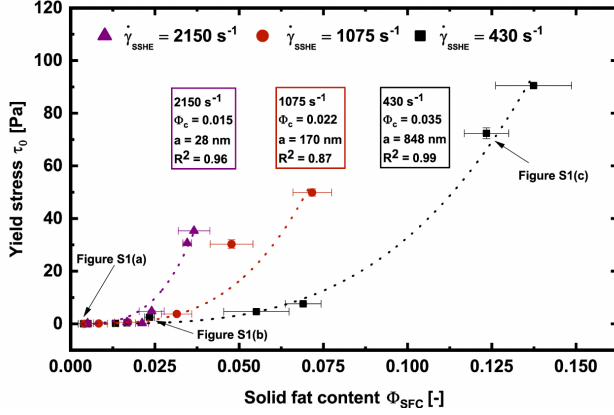


Figure 5. Yield stress τ_0 as a function of solid fat content Φ_{SFC} for PKO CMS crystallized at $\dot{\gamma}_{\text{SSHE}} = 430, 1075,$ and 2150 s^{-1} . The dashed lines indicate the fitted curves according to eq. 3 with the interfacial tension $\gamma = 0.01 \text{ Nm}^{-1}$ and the fractal dimension $D = 2.7$. The corresponding value of the primary particle diameter a , the critical crystal concentration Φ_c , and the resulting R^2 coefficient are displayed in the boxes.

2.2 Micro-foaming of fat crystal melt suspension

A membrane foaming apparatus (Kinematica Megatron MT-MM 1-52, Kinematica AG, Luzern, Switzerland) was used for the foaming of the CMS. The dynamically enhanced membrane foaming apparatus consists of two concentric cylinders [6]. The static outer cylinder with a diameter of 54.5 mm and an axial length of 60 mm acts as a membrane with nominal pore size of 3.5 μm . The inner rotating cylinder with a diameter of 44.5 mm generates a defined rheometric shear flow or a Taylor-Couette type of flow field depending on the fluid viscosity and the related Taylor number (Ta) in the 5 mm gap between the outer and inner cylinder thereby detaching the gas bubbles from the membrane surface and dispersing these into the continuous CMS phase. The CMS was axially pumped at 20 kg/h through the 5 mm gap of 60 mm length. Nitrogen gas was injected through the membrane into the gap at 7 bar with a flow rate of 20 L/h. A schematic radial cross-section of the foaming cell is depicted in the processing scheme in Fig 1.

Polarized light microscopy was used to investigate crystal morphology as well as bubble size distributions. Samples were slightly cooled during imaging by placing an ice container on the stage of the microscope. Gas bubble size and size distribution were calculated by using a custom-built image analysis software (ETH-SFP Bubble Detect). A minimum of 300 bubbles was counted to calculate a single bubble size distribution. SPAN values correspond to width divided by median bubble diameter of the distribution $(X_{90,0} - X_{10,0})/X_{50,0}$.

Previous work on membrane emulsification showed that the drop diameter is determined by the wall shear stress τ_w acting at the membrane surface and the pore diameter of the membrane. For the boundary condition $\tau_w > \tau_0$, the wall shear stress τ_w in the membrane foaming apparatus was calculated via the wall shear rate $\dot{\gamma}_w$ according to equations 4 and 5 given below for rotating inner cylinder and a static outer membrane cylinder.

$$\dot{\gamma}_w = \frac{2\Omega}{n((\alpha)^{2/n} - 1)} \quad (7)$$

$$\tau_w = \tau_0 + K\dot{\gamma}_w^n = \tau_0 + \tau_{vs} \quad (8)$$

The Bingham number Bm was introduced to describe the ratio of the yield stress τ_0 and the viscous flow stress τ_{vs} acting during gas bubble dispersion in the PKO CMS. The Bingham number Bm for a CMS in a shear flow is expressed as:

$$Bm = \frac{\tau_0}{\eta(\dot{\gamma}_w^n)} = \frac{\frac{6\gamma}{a} \Phi^{1/(3-D)}}{K\dot{\gamma}_w^n} \quad (9)$$

with the power law behavior of the structure-related yield value approximations considered.

Figure 6 demonstrate the functional relationship between the reciprocal Bingham number Bm^{-1} and the resulting normalized maximum bubble size $x_{90,0}$ of the foam generated under various solid fat content conditions at different shear rates in the membrane foaming device.

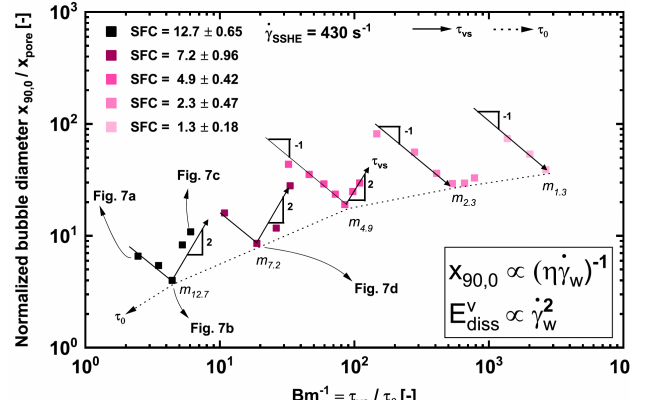


Figure 6. Normalized bubble diameter $x_{90,0}/x_{\text{pore}}$ as function of the reciprocal Bingham number Bm^{-1} for foamed PKO CMS crystallized at $\dot{\gamma}_{\text{SSHE}} = 430 \text{ s}^{-1}$. Direction of increasing viscous stress τ_{vs} for a given Φ_{SFC} is indicated (solid lines) as well as direction of increasing yield stress τ_0 (dashed line).

2.2 Novel 3D-printing of foamed fat suspensions

We introduced and applied a novel Additive Manufacturing (AM) approach capable of producing complex 3D food structures at elevated production rates and with added functionality. The complex 3D structure was broken down into three main length scales denoted as macro-, meso- and micro-scale. The macro-scale product elements acting as scaffold for the meso-scale elements were manufactured by twin-screw cold extrusion applying a macro-scale printing die (cm-range). Two six-axes robots equipped with a

single screw meso-scale (mm-range) extruder system and an electromagnetically triggered single/multi jetting micro-scale (100 μm scale) nozzle dose and shape the meso- & micro- scale product elements and connect them synchronously to the macro scale printed scaffold element. Figure 7 shows different views of the setup and product.

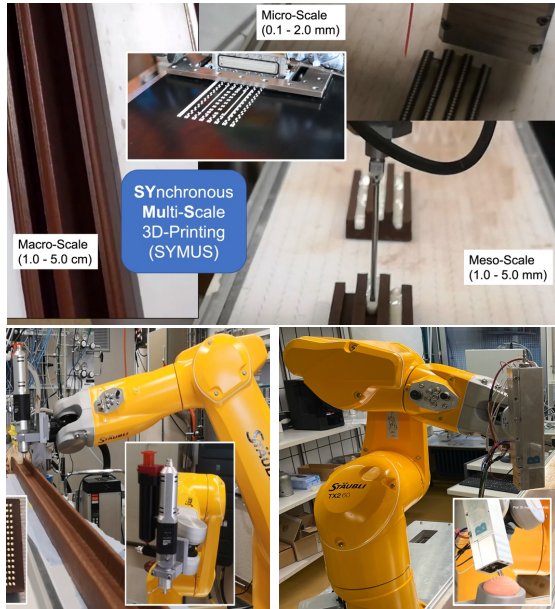


Figure 7: Setup for Multi-Scale Synchronous 3D-Printing of chocolate confectionery from foamed chocolate/fat crystal suspensions crystallized and foamed with in-line rheological control by UVPPD.

2.2 USDMA controlled solidification

The solidification under cooling conditions of micro-foamed and non-foamed chocolate confectionery is a final processing step being decisive for (1) shape retention of printed or molded products and for (2) the final formation of the fat crystal network concerning the crystal polymorph structure and the structure density. Both, (1) and (2) determine the final product structure significantly. The application of US attenuation measurements in order to detect fat crystal networking during solidification crystallization of molded chocolate masses during continuous cooling in industrial cooling tunnels has demonstrated to allow for viscosity and elasticity monitoring until the molded solidified product detaches from the mold wall or the 3D-printed product has solidified to an extent that it can be picked by robots and packaged. The degree of shrinkage of confectionery fat structure during its solidification is an important characteristic to enable proper demolding and improved resistance against fat migration and quality deterioration by fat bloom formation during storage. Figure 8 demonstrates the US-transmitter/receiver installation in a Makrolon mold and the characteristic US attenuation (US amplitude damping) pattern during chocolate mass solidification and final detachment from the mold wall. During solidification crystallization domains of initially (i) increasing viscosity and subsequent (ii) increasing elasticity upon crystal network formation were distinguished since increase in viscosity leads to increased US-

amplitude damping, whereas elasticity increase causes a reduction of the damping effect.

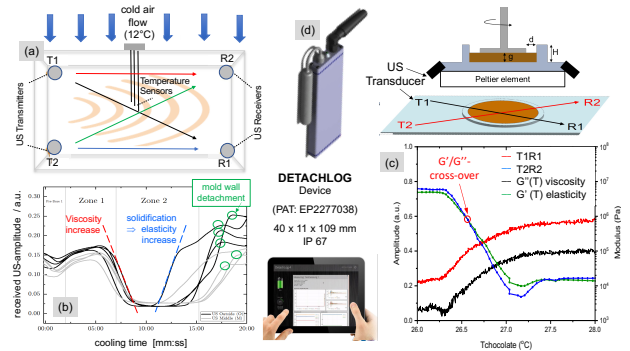


Figure 8: US-attenuation-based in-line measurement of molded chocolate during solidification & mold wall detachment (ETH-Detachlog) (a) US transmitter/receiver placement at mold bottom; (b) US-amplitude attenuation with differentiation of viscous/elastic contributions; (c) detailed analysis of viscous and elastic moduli (G'' , G') during chocolate mass solidification [8].

3. Summary

The US-Doppler velocimetry based UVPPD technology was adapted for in-line measurements of the non-Newtonian rheological material functions of crystallized and micro-foamed chocolate confectionery fat crystal suspensions. The transient characteristics of such systems cannot be measured satisfyingly by off-line rheometry. For applications like foaming and 3D-printing the yield stress τ_0 was demonstrated to be the crucial rheological material parameter determining (i) fat crystal network formation, (ii) related stabilization of micro-foam bubble structure as well as (iii) contraction and structure density of the final product. As soon as the material behavior of the investigated confectionery/fat systems switch from paste-like to solid-like the introduced in-line USDMA (Ultrasound Dynamic Mechanical Analysis) based measurements allowed for monitoring solidification kinetics and structure density development. Thus, the applied US-based measuring principles are of pivotal relevance for application in chocolate confectionery industry. From such new insights optimization criteria for products and process design (crystallizer, 3D-Printer, cooling tunnel, foaming device, mold) are on the way to be developed and commercialized.

References

- [1] K. Mishra et al. (2022) Journal of Colloid and Interface Science, vol. 630: no. Part A, pp. 731-741, Amsterdam: Elsevier, 2022.
- [2] K. Mishra et al. (2021); Soft Matter, vol. 18: no. 6, pp. 1183-1193, Cambridge: Royal Society of Chemistry, 2021.
- [3] Windhab, E. J (1995). Rheology in food processing, chapter 5, pp. 80–116. Springer US, Boston, MA, 1995.
- [4] Ouriev, B., Windhab E. (2004); Measurement Science and Technology, 14(11):1963-1972, 2004.
- [5] J Wiklund, B Birkhofer, S Jeelani, M Stading, E Windhab (2012); Appl. Rheol. 22 (2012) 42232
- [6] Pokorny L., Kohler L., Takeda Y., Windhab E. (2016); Flow Measurement and Instrumentation; 52, pp.137-143
- [7] K. Mishra, D. Dufour, E. Windhab (2020); Crystal Growth & Design, 20(2):1292–1301, 2020.
- [8] E. Windhab et al. (2012); Patent Nr. EP2277038

Ultrasound pulse measurement of air-lift multiphase pipe flow in an inclined pipe

Yuichi Murai¹, Takumi Hayashi¹, Dongik Yoon¹, Hyun Jin Park¹, Yuji Tasaka¹,
Satoru Takano², and Sotaro Masanobu³

¹ Faculty of Engineering, Hokkaido University, N13W8, Sapporo 060-8628, Japan

² Ocean Engineering Department, National Maritime Research Institute, Mitaka, Tokyo 181-0004, Japan

³ Offshore Advanced Technology Department, National Maritime Research Institute, Mitaka, Tokyo 181-0004, Japan

We developed the method of ultrasonic detection for large bubbles rising rapidly in an upward gas–liquid two-phase pipe flow at a variable inclination angle. The proposed method uses combination of the echo intensity reflected by large bubbles and the Doppler frequency. The method using the Doppler frequency performs well in the detection of large bubbles regardless of the interface condition, whereas the method using the echo intensity has trouble in detecting an uneven interface. In contrast, the information of the echo intensity guarantees high accuracy of the interface detection even if that of the Doppler frequency has low accuracy for the detection owing to many small bubbles existing in the liquid film. Here, the two methods are combined to overcome their problems, and a validation test confirms that the results of the combined method agree well with the results of image processing. As demonstrations of the proposed method, the slug frequency, velocity, and airflow rate of large bubbles in an air-lift pump are obtained.

Keywords: Air-lift pump, three-phase flow, bubble velocity, liquid film, flow-metering, pressure loss

1. Introduction

Multiphase flow plays an important role in many practical fields such as oil transportation, chemical engineering, and airlift pumps. Slug flow is a common flow pattern that appears widely in two-phase flow where bubbles become large enough to occupy almost the entire pipe cross-section. The characteristics of slug flow with a high superficial velocity of the gas phase (j_g) are completely different from those of the Taylor bubble that rises smoothly keeping axisymmetric interfacial figures. In air-lift pumps, typical speed of the bubbles exceeds 3 m/s and the gas-liquid interface experiences highly unsteady three-dimensional turbulence[1-4]. In this study, we have developed a method to capture such an interface using combined capabilities of ultrasound echo intensity and Doppler signal information based on the knowledge of ultrasonic interfacial detection[5-10].

2. Experimental Method

2.1 Experimental facility

The airlift pump system at the National Maritime Research Institute (NMRI, Japan) is used in the present study (Fig. 1). The total height (H) of the main pipe was 8.5 m and the inner diameter (D) was 26 mm. The inclination of the pipe (θ) could be freely controlled from 45° to 90°. Compressed air was injected into the bottom of the pipe at a fixed flow rate controlled by an electronic valve, and a flowmeter monitored the flow rate. The main pipe was filled with water and the water level was maintained by a water level adjuster next to the main pipe. The injected air was discharged at the outlet of the pipe, and the lifted water was discharged to a top water tank along a guide vane. The liquid flow rate was estimated by measuring the mass of

stored water in the tank, and the superficial velocity of liquid flow (j_l) was obtained from the flow rate. The top tank allowed only water to enter the bottom water tank.

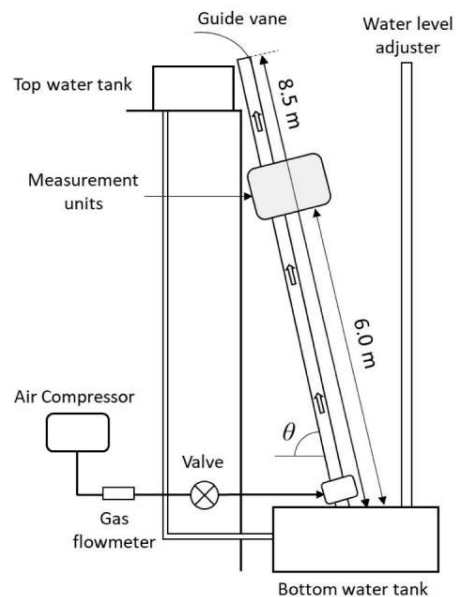


Figure 1: The experimental set-up of an air-lift pump system allowing variable inclination angle at $45^\circ < \theta < 90^\circ$ degree.

2.2 Ultrasound Sensing

The measurement units comprised two US measurement sets with one optical measurement system as shown in Fig. 2. Two US transducers (TDX1 and TDX2) were installed in each water jacket made from transparent acrylic resin, and they were sufficiently submerged in water to avoid exposure to air. Both transducers were placed 30 mm from

the outer wall of the pipe to avoid the near-field effect. The scattering reflection of large bubbles occurs at nose regions because of its curved interface, and it results in echo signal loss. Therefore, we determine the optimal angle of both TDXs as 3° based on our previous study that measured the large bubbles using ultrasound measurement [4, 6]. The distance (ITDX) between the centers of TDX1 and TDX2 was 500 mm. Large bubbles with high j_g are asymmetric in the inclined pipe, and the thickness of the liquid film was thus different on the two sides. Accordingly, TDX1 and TDX2 were installed on opposite sides of the pipe to measure the thickness on both sides. A high-speed camera and light-emitting diode panel were installed at the same position as TDX2 for comparison with the US measurement.

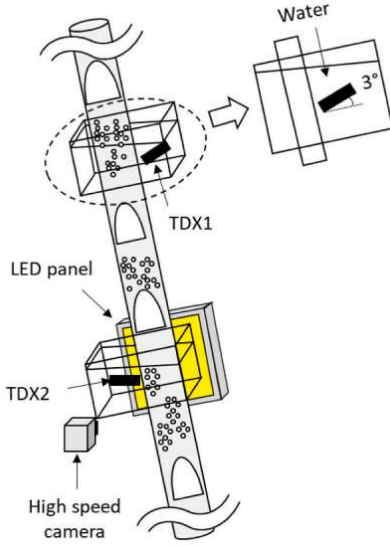


Figure 2: Location of ultrasound transducer to measure the asymmetric multiphase flow inside the inclined pipe.

2.3 Experimental conditions

The experiments were conducted using three superficial velocities of the gas-phase flow ($j_g = 1.67, 3.71, 4.95$ m/s). Since the US measurements utilized in many industries involving inclined conditions, three inclinations ($\theta = 45^\circ, 75^\circ, 90^\circ$) were thus adopted. j_l is varied by not only θ but also j_g , and the range of j_l was 0.70–1.05 m/s. Note that the flow pattern falls in the slug flow regime and does not change remarkably as shown in Fig. 3. All other details of the experimental conditions are listed in Table 1.

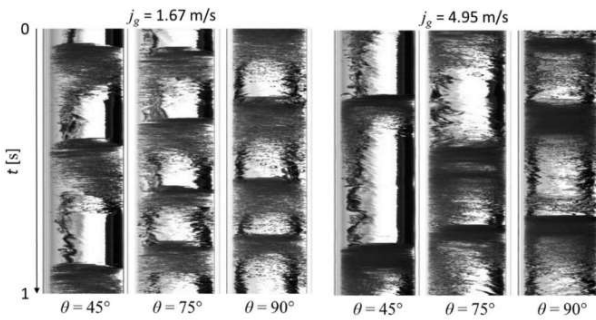


Figure 3: Timeline images of the gas–liquid two-phase flow produced by image processing of high-speed video camera.

Table 1: Experimental and measurement conditions

Flow conditions		
Inner diameter of pipe (D)	26	mm
Pipe length (L)	8.5	m
Inclination of pipe (θ)	45, 75, 90	degrees
Superficial velocity of gas-phase (j_g)	1.67, 3.71, 4.95	m/s
Superficial velocity of liquid-phase (j_l)	0.70–1.05	m/s
Water temperature	21	$^\circ\text{C}$
Measurement conditions		
Measurement position (l/D)	250	
Ultrasound frequency (f_0)	4.187	MHz
Pulse repetition frequency (f_{PRF})	3.998	kHz
Cycles of ultrasound pulse	4	
Emission voltage of ultrasound	60	V
Gain value of US generators	+20	dB
Recording range of voltage (V_{range})	500	mV
Speed of sound (c)	1480	m/s
Sampling speed of US signal (t_s)	40	ns
Spatial resolution of US signal ($\Delta\xi$)	29.4	μm
Measurement time	10	s
Angles of TDX	3	degrees
Frame rate of the camera	500	Fps

3. Experimental Results

3.1 Time-line visualization

From each ultrasound transducer, we could obtain echo intensity and Doppler velocity as a function of time. These original data are shown in Fig. 4 for the vertical pipe and Fig. 5 for 45-deg inclined pipe. The velocity profile is estimated using two successive pulses (e.g., the first and second pulses, the second and third pulses, and the third and fourth pulses), and the temporal resolution of the velocity profile is thus the same as that of the raw echo signals (TDX2-Echo). The liquid velocity remarkably fluctuates with the measurement time for dispersed bubbles passing the US beam whereas more than half of values of the liquid velocity are almost zero for the large bubbles on the US beam. The variance of velocity (TDX2-Var) is estimated for further analysis of the fluctuation of the liquid velocity. A blue line in TDX2-Var represents the variance whereas a red line represents the moving average of the variance using 80 windows, with the corresponding t being 0.02 s.

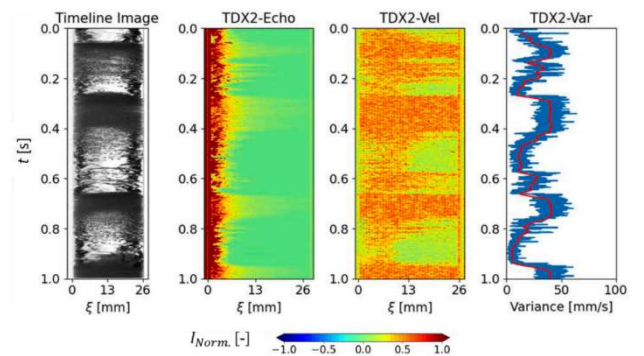


Figure 4: Timeline ultrasonic echogram and Doppler map at $j_g = 3.71$ m/s and $\theta = 90^\circ$.

Under the vertical condition (Fig. 4), it is clearly seen that the variance is high at the dispersed bubbles whereas it is low at the large bubbles as determined by comparing with the timeline image. However, this trend becomes unclear at $\theta = 45^\circ$ (Fig. 5). This is due to the small bubbles in the liquid film. The thickness of the liquid film increases with a reduction of inclination, and the bubbles are entrained in the film. The bubbles dispersed in

the liquid film lead to a high variation in the Doppler frequency, and the variance does not vary remarkably compared with the variance at $\theta = 90^\circ$. To conclude, the variance depends on the number of bubbles dispersed in the liquid film, and the number density of bubbles in the film increases with the reduction of θ resulting in errors in the detection of large bubbles.

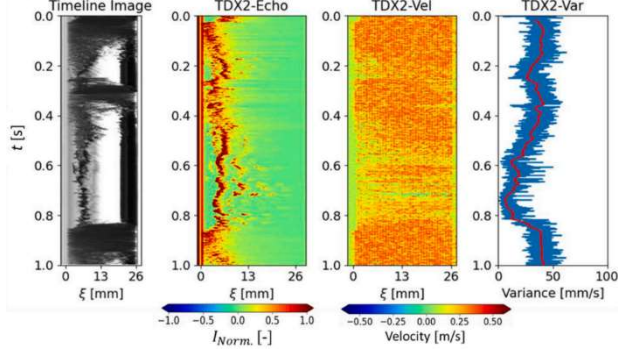


Figure 5: Timeline ultrasonic echogram and Doppler map at $j_g = 3.71$ m/s and $\theta = 45^\circ$.

3.2 Combined algorithm

The results for the detection of large bubbles using the information of echo intensity and Doppler frequency are shown in Fig. 6. The grey and green regions indicate the detection of a large bubble by the methods using information on the echo intensity and Doppler frequency. Although both methods identify the large bubble, they fail sometimes to recognize the bubble. We consider two combination algorithms, namely the AND OR algorithms. In the AND algorithm, a large bubble is detected if both methods share part of the detection of the large bubble, and the passing times of the large bubble in the nose and tail are determined by the entrained small bubbles in the liquid film (see the red line). Meanwhile, the method using the echo intensity identifies the large bubble despite the existence of small bubbles in the film. The echo intensity reflected by small bubbles is removed by the median filter, leaving only echo signals reflected by the large bubble. In summary, both methods are likely to involve large errors when they are solely used owing to the above described issues. However, their combination cancels out each other's drawbacks. We have overcome the issue with comparison by optical measurement and applied the most suitable thresholds for each ultrasound signals. Details are reported in our previous paper [4, 11, 12].

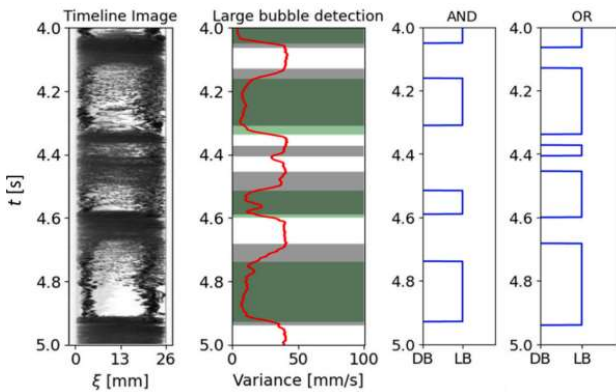


Figure 6: Comparison of AND OR algorithms for large bubble detection at $j_g = 3.71$ m/s and $\theta = 90^\circ$.

3.3 Statistics and discussion

Fig. 7 shows the probability of the slug frequency obtained from (a) the proposed method and (b) brightness information of optical measurement with the colors of the graphs indicating j_g . For the result of US measurement, a common feature among the graphs is that f_s is densely distributed at low frequencies with $j_g = 1.67$ m/s whereas the distribution tends to become wide with an increase in j_g at all inclinations. This trend agrees with the result of Murai et al. that the mean f_s increases with j_g [4]. Meanwhile, f_s at $\theta = 75^\circ - 90^\circ$ has a similar distribution between $j_g = 1.67$ m/s and $j_g = 3.71$ m/s, whereas f_s at $\theta = 45^\circ$ has a similar distribution between $j_g = 3.71$ m/s and $j_g = 4.95$ m/s. This indicates that the length and velocity of the large bubble appreciably vary at $45^\circ = \theta \leq 75^\circ$. In other words, f_s depends on both the inclination of the pipe and the superficial velocity of the gas flow. In the comparison of the US and optical measurements, f_s at $j_g = 1.67$ m/s and 3.71 m/s obtained from both measurements in all θ shows similar trends to each other, although the probability is slightly different. Meanwhile, f_s at $j_g = 4.95$ m/s obtained from optical measurement is more densely distributed than that of US measurement. It is supposed that the minor differences between both measurements come from the definition of the large bubble.

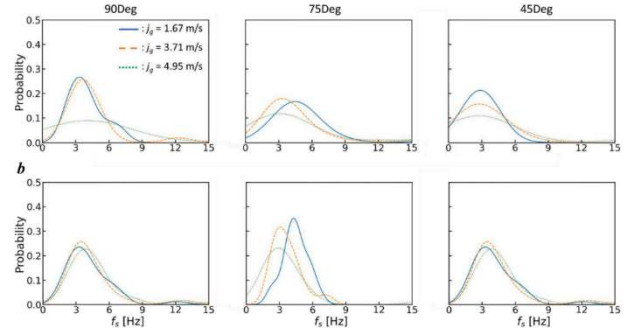


Figure 7. Probability of the slug frequency obtained from (a) proposed method and (b) optical measurement.

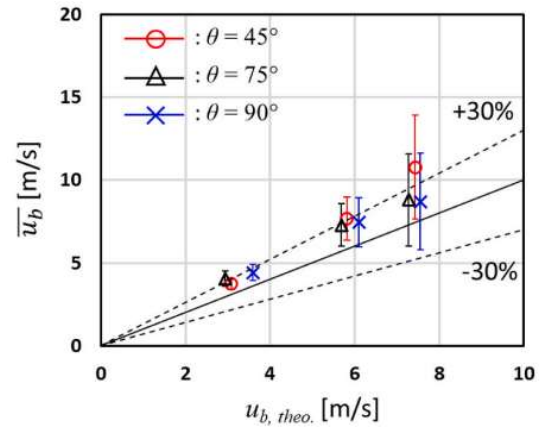


Figure 8. Mean velocity of large bubbles rising in the airlift pump

Fig. 8 shows the comparison of mean velocity of rising bubbles, u_b and the theoretical velocity of large bubble. A black solid line indicates the one-to-one correspondence between u_b and theoretical one. The dashed lines indicate the difference between both velocities. The difference is almost within $\pm 30\%$, and the difference mainly comes from the different flow patterns

between the present study and Bendiksen study[13]. Many dispersed small bubbles in the slug and churn patterns were observed in the present study, Bendiksen study was completed with the little small bubbles. We supposed that the dispersed bubbles in the upside and downside of large bubbles cause the pressure difference resulting in the high variation of velocity for the large bubbles. The air flow rate of the large bubbles is next obtained using the information on u_b .

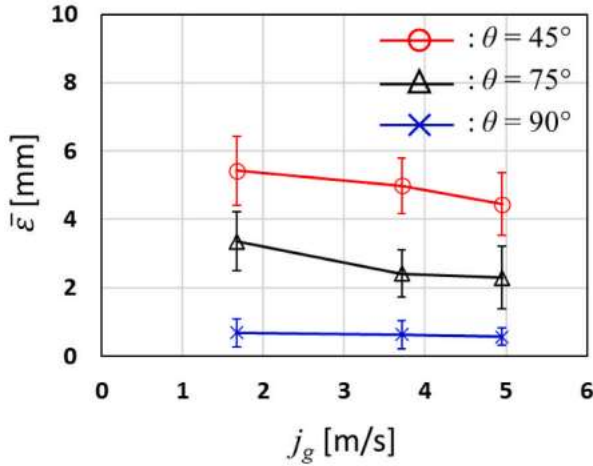


Figure 9. Mean thickness of liquid film clinging on the pipe wall

Fig. 9 shows the mean liquid film thickness of large bubbles, for each θ and j_g . It increases with the reduction of θ owing to the buoyancy contribution to the bubble; however, it tends to decrease with an increase in j_g . This is because the inertia of the gas phase flow is intensified with an increase in high j_g resulting in an increase in u_b in the streamwise direction. In other words, the buoyancy contribution weakens relative to the inertia. Note that the error bars in the figure means standard deviation come from intermittent passage of liquid slugs. Although ε slightly varies along the perimeter of the pipe, it is almost constant under the vertical condition. The volume of a large bubble rising under the vertical condition is thus easily estimated by assuming that the shape of the bubble is a cylinder.

4. Concluding Remarks

This study proposed a US measurement technique for measuring slug flow with high superficial velocities of gas-phase flow. Two methods were used to identify large bubbles in the slug flow. One used the echo intensity and the other used the Doppler frequency. It was confirmed that the method using the echo intensity was unlikely to detect a large bubble when there was scattered reflection from the uneven interface, whereas the method using the Doppler frequency could not identify a large bubble when the liquid film contained small bubbles. The two methods were thus combined to overcome their demerits, AND and OR algorithms were adopted for the combined method.

Acknowledgement

This work was performed with funding from the Japan Organization for Metals and Energy Security (JOGMEC), Ministry of Economy Trade and Industry, Japanese Government (METI). The research also received funding from the JSPS KAKENHI (grant number JP21J11854). The authors are grateful to Dr. Stéphane Fischer for technical support in the use of UB-LAB X8 during the experiment and also to Prof. Yasushi Takeda for the technical advises.

References

- [1] Z. Wang, Y. Kong, D. Li, X. Wang, D. Hu, Investigating the hydrodynamics of airlift pumps by wavelet packet transform and the recurrence plot” Exp, Thermal Fluid Science 92 (2018) 56–68.
- [2] H. Fujimoto, T. Nagatani, H. Takuda, Performance characteristics of a gas–liquid–solid airlift pump” Int. J. Multiphase Flow 31 (2005) 1116–1133.
- [3] K. Shimizu, S. Takagi, Study on the performance of a 200 m airlift pump for water and highly viscous shear-thinning slurry” Int. J. Multiphase Flow 142 (2021), 103726.
- [4] Y. Murai, T. Hayashi, D. Yoon, H.J. Park, Y. Tasaka, S. Takano, S. Masanobu, Ultrasound Doppler measurement of air-lift two-phase and particulate three-phase pipe flows” Exp, Fluid 63 (2022) 126.
- [5] C. Tan, Y. Murai, W. Liu, Y. Tasaka, F. Dong, Y. Takeda, Ultrasonic Doppler technique for application to multiphase flows: a review” Int. J. Multiphase Flow 144 (2021), 103811.
- [6] Y. Murai, Y. Tasaka, T. Nambu, Y. Takeda, S.R. Gonzalez, Ultrasonic detection of moving interfaces in gas-liquid two-phase flow” Flow Meas, Instrumentation 21 (2010) 356–366.
- [7] H.J. Park, Y. Tasaka, Y. Murai, Bubbly drag reduction investigated by time-resolved ultrasonic pulse echography for liquid films creeping inside a turbulent boundary layer” Exp, Thermal Fluid Sci 103 (2019) 66–77.
- [8] H. Murakawa, H. Kikura, M. Aritomi, Application of ultrasonic multi-wave method for two-phase bubbly and slug flows” Flow Meas, Instrumentation 19 (2008) 205–213.
- [9] D. Yoon, H.J. Park, T. Ihara, Development of an instantaneous velocity-vector-profile method by using conventional ultrasonic transducers” Meas, Sci. Technol. 33 (2021), 035301.
- [10] H.J. Park, D. Yoon, S. Akasaka, Y. Tasaka, Y. Murai, Gas volume estimation in a vertical pipe flow considering the bubble size obtained from an ultrasonic velocity vector profiler” Exp, Fluid 63 (2022) 130.
- [11] D. Yoon, T. Hayashi, H. Park, Y. Tasaka, Y. Murai, S. Takano, S. Masanobu, “Ultrasound measurement of large bubbles rising in angled slug pipe flows” Flow Measurement and Instrumentation 91 (2023) 102357.
- [12] N. Otsu, A threshold selection method from gray-level histograms” IEEE, Trans. Sys. Man. Cyber. 9 (1979) 62–66.
- [13] K.H. Bendiksen, An experimental investigation of the motion of long bubbles in inclined tubes, Int. J. Multiphase Flow 10 (1984) 467–483.

Measurement of Solid-Gas-Liquid Three-Phase Flow using Pulsed Ultrasound

Naruki Shoji¹, Hiroshige Kikura², Hideharu Takahashi³, Koji Teramoto¹, and Hideki Kawai¹

¹ College of Design and Manufacturing Technology, Robotics and Mechanical Engineering Research Unit, Muroran Institute of Technology, 27-1 Mizumoto-cho, Muroran, Hokkaido 050-8585, Japan

² Laboratory for Zero-Carbon Energy, Tokyo Institute of Technology, 2-12-1 Ookayama, Meguro-ku, Tokyo 152-8550, Japan

³ School of Engineering, Department of Mechanical Engineering, Tokyo Institute of Technology, 2-12-1 Ookayama, Meguro-ku, Tokyo 152-8550, Japan

In the process of transporting methane hydrate from the seafloor, a multiphase flow of methane hydrate (solid), methane gas (gas), and seawater (liquid) is generated in the recovery pipe. It is important to measure the flow ratio of each phase in the pipe in order to determine the amount of recovery and control the flow conditions. To realize the multiphase flow measurement, we focused on ultrasonic velocity profiler (UVP) and developed the measurement system. In this study, we generated a solid-gas-liquid three-phase flow (ice-air-water system) in a vertical pipe and applied the UVP to it in order to measure the multiphase flow in the pipe. An algorithm was developed to separate the velocity data of each phase by focusing on the signal intensity and spatio-temporal shape of the reflected echo signals obtained from each phase. Moreover, the validity of this method was experimentally confirmed by comparing with high-speed camera images.

Keywords: Multiphase flow, Phase identification, Signal processing, Speckle pattern

1. Introduction

Methane hydrate, which is a solid form of methane gas, is expected to be a next-generation energy resource in Japan and is believed to be stored in the deep seafloor with low temperatures and high pressures environments [1]. The methane hydrate (MH) transportation from the seafloor has attracted attention as a method using the gas-lift effect, in which gas is injected into a vertical pipe to generate an upward flow [2]. In the gas-lift method, a solid-gas-liquid multiphase flow of methane hydrate, methane gas, and muddy seawater is generated in the pipe. To optimize the pumping efficiency and assessing the status of MH recovery, the solid-gas-liquid volume ratio in the pipe should be known and the appropriate gas injection flow rate should be controlled according to the pumping conditions. However, there is no established method for measuring the solid-gas-liquid multiphase flow. It is difficult to use contact probes or other means to invasively measure the inside of the pipe because of the flow of solid phase. Moreover, a metal pipe is used as the recovery pipe, applying optical methods such as particle image velocimetry are difficult. Therefore, this study focuses on ultrasonic measurement methods that allow non-invasive measurement from outside the metal pipe and aims to develop a monitoring technique for solid-gas-liquid multiphase flow in a pipe using ultrasonic waves. In this study, ultrasonic velocity profiling method (UVP) was applied to a simulated solid-gas-liquid multiphase flow, ice-air-water system, in a vertical pipe, and features were extracted from the ultrasonic echo signals to verify whether the solid, gas, and liquid phases could be distinguished respectively.

2. Experiment

2.1 Experimental facility

To verify the feasibility of the solid-gas-liquid three-phase flow measurement using the UVP method, the pulsed ultrasonic measurement was applied to the multiphase flow and reflected echo signals were acquired. Figure 1(a) shows the test facility to generate solid-gas-liquid three-phase flow. The test facility mainly consists of a water tank, a pump, a vertical pipe (made of acrylic, inner diameter D : 50 mm), an air compressor, a gas injector, a solid injector, and an overflow tank. Tracer particles (nylon particle, mean diameter: 80 μm) were mixed in the water tank, and the pump generated an upward flow in the vertical pipe. The water flow rate was referenced to an electromagnetic flow meter installed in the flow channel. As the gas phase, compressed air was injected into the vertical pipe by the air compressor, and the gas flow rate was monitored by a float flow meter. In addition, ice was injected as the solid phase which simulated the MH. Figure 1(b) shows the schematic diagram of the measurement setup of UVP. In this experiment, the ultrasonic transducer (TDX) was installed at an angle of 16° to the pipe wall normal in a test section at 3 m from the air injection section ($L/D = 60$) to verify the feasibility of measuring the solid-gas-liquid multiphase flow using the UVP. A water box was placed around the test section pipe for acoustic matching to pass through ultrasonic waves into the pipe from outside the pipe. Table 1 shows the experimental conditions. During the experiment, the water flow rate and the air flow rate was kept constant at 46 liter/min and 1 liter/min, respectively. Ice was also injected from the solid injector during the ultrasonic measurement time. The size of ices was less than 30 mm.

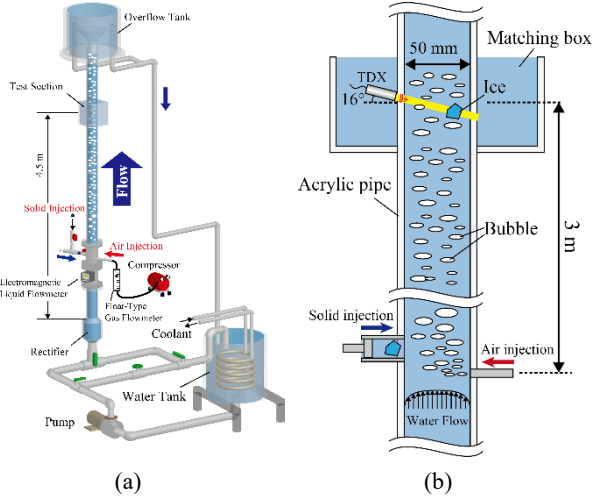


Figure 1: Schematic diagram of (a) test facility for solid-gas-liquid three-phase flow generation and (b) measurement setup.

Table 1: Experimental conditions.

Parameter	Condition
Fluid	Ice-air-water three-phase flow (with 80 μm nylon particles)
Pipe inner diameter	50 mm
Wall thickness at test section	1 mm
Water temperature	10°C
Water flowrate	46 liter/min
Air flowrate	1 liter/min
Size of ices	Less than 30 mm

2.2 Measurement system

Figure 2 shows the ultrasonic measurement system and Table 2 shows the measurement conditions for the experiment. The measurement system consists of laboratory-made ultrasonic measurement hardware [3], the hardware control and signal processing computer, and TDX (ultrasonic center frequency: 2 MHz, element diameter: 10 mm). The hardware mainly includes a high-voltage pulser for the pulsed ultrasound transmission, a variable amplifier for the received echo signal, a low-pass filter, an analog-to-digital converter (ADC), and FPGA (Field Programmable Gate Array) to control each circuit. In this experiment, ultrasonic pulses were transmitted at ± 75 V, and the received echo signals were sampled by the ADC at a sampling speed of 50 MS/s and bit resolution of 12 bits. The pulse repetition frequency was set to 2000 Hz and the echo signal was recorded 8192 times consecutively in one measurement (appx. 4.2 seconds). The recorded signals were processed on the computer using MATLAB 2021a (MathWorks). Incidentally, a high-speed camera image measurement (FASTCAM Mini AX50, Photron) using the backlight method was also performed simultaneously synchronized with the pulse transmission timing (2000 fps) to identify the ultrasonic reflection source.

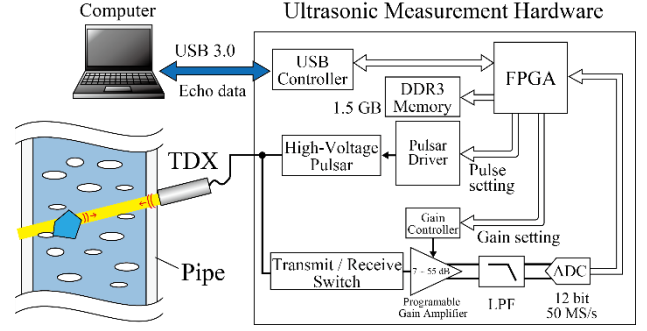


Figure 2: Schematic diagram of the ultrasonic measurement system.

Table 2: Measurement conditions.

Parameter	Condition
Sound velocity in water	1448 m/s
Ultrasonic center frequency	2 MHz
Wavelength in water	0.72 mm
Number of pulse cycles	2
Ultrasonic element diameter	10 mm
Pulse repetition frequency	2000 Hz
Incident angle	16°
Number of echo signals recorded consecutively	8192
Sampling speed of echo signal	50 MS/s

3. Phase-Separation Algorithm

3.1 Signal characteristics

To separate the solid (ice), gas (air) and liquid (water) phase velocity data of UVP, the characteristics of echo and Doppler signals were considered. First, to discriminate between the liquid phase (tracer particles) and other phases, we focused on the statistical method based on the reflected echo signal intensity using the reflectance of each phase [4]. The acoustic reflectance can be described by

$$R = \frac{Z_1 - Z_2}{Z_1 + Z_2} = \frac{\rho_1 c_1 - \rho_2 c_2}{\rho_1 c_1 + \rho_2 c_2} \quad (1)$$

where Z represents acoustic impedance, c is sound velocity, and ρ is the density, respectively. The reflectance R of the gas-liquid interface is greater than the small particle-liquid interface significantly. Thus, the echo intensity reflected from a gas-phase is larger than from a particle. In addition, echo intensity also depends on the reflector size. If the reflector size is larger than the ultrasonic beam diameter, higher echo intensities are observed. Therefore, liquid phase can be identified by thresholding to echo intensity. Next, we examined a method for discriminating between the solid and gas phases. Figure 3 shows example of spatio-temporal plots of high-speed camera and ultrasonic echo signal intensities in bubbles and ice obtained experimentally. In each figure, the horizontal axis represents measurement time, t , and the vertical axis represents the distance from the TDX surface, x . The echo

intensity was determined by the following equation:

$$A(t, x) = \sqrt{s^2(t, x) + \{H(s(t, x))\}^2} \quad (2)$$

where s is the echo signal, and H represents the Hilbert transform. As shown in Figure 3(b), the spatio-temporal intensity distribution of the signal reflected from the bubble interface was short in the distance direction and had high signal intensity. In contrast, as shown in Figure 3(d), the spatio-temporal intensity distribution of the signal reflected from ice has a high signal intensity at the ice interface and a complex speckle pattern. Considering the ultrasonic propagation paths in the case of bubbles and solids as flowing reflectors, as shown in Figure 4, the reflectance at the bubble interface is approximately 1 from Eq. (1), and the signal width of the reflected echo is equal to the transmitted pulse width. On the other hand, in the solid phase, it is reflected at the solid interface and incident from the liquid phase into the solid phase. This causes multiple reflections in the solid. The reflected waveforms are superimposed and interfere with each other. In addition, because the solid rotates and moves with the flow, the interference waveform shape changes with time. As a result, a speckle pattern appears in space-time. Therefore, the gas and solid phases can be distinguished by detecting this speckle.

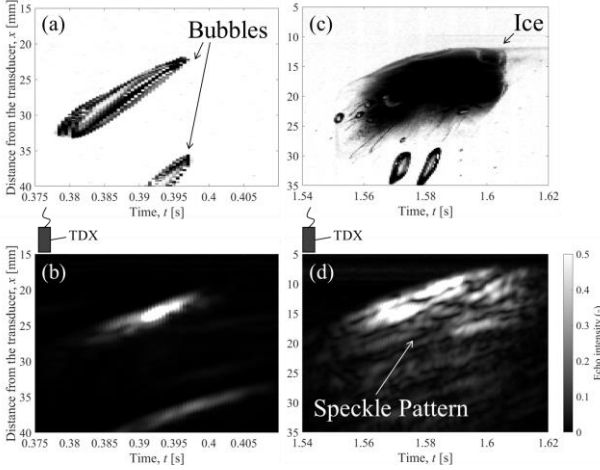


Figure 3: Example of spatio-temporal plots of high-speed camera and ultrasonic echo signal intensities in bubbles and ice. (a) high-speed camera image and (b) echo intensities in bubbles. (c) high-speed camera image and (d) echo intensities in ice.

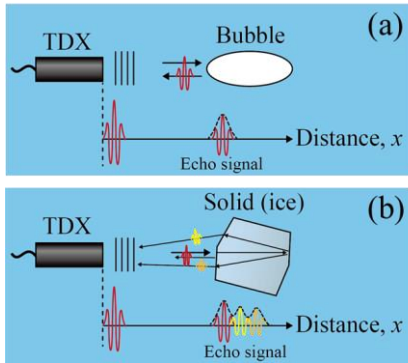


Figure 4: Ultrasonic propagation path in gas and solid phases.

3.2 Speckle detection

To discriminate between solid and gas phases, speckle was detected from the signal. Speckles are generated by the interference of diffusely reflected components in the solid phase, so multiple peaks of signal intensity appear in the time direction and the intensity decay is slow. In contrast, the gas phase is totally reflective at the interface, resulting in a relatively sharp single peak. Then, a moving time window was set for the Doppler signal intensity, and the autocorrelation function was calculated for the window. When the decay is slow and multiple peaks appear, the fall of the correlation value with respect to the time lag is slow. By evaluating the decay time of the correlation value, it is possible to determine the speckle (identify the solid and gas phases). Where the received echo signal at transmission timing, t , and reflected position, x , is $s(t, x)$, the echo signal is represented as follow:

$$s(t, x) = A(t, x) \cos \{4\pi(f_c + f_D)x/c\} \quad (3)$$

where c is sound velocity, A is signal intensity, f_c is ultrasonic center frequency and f_D is the Doppler frequency, respectively. By applying quadrature demodulation to Eq. (3), a complex Doppler signal $z(t, x)$ containing only the Doppler frequency component is obtained.

$$\begin{aligned} z(t, x) &= \text{LPF} \left[s(t, x) \cos \left(\frac{4\pi f_c x}{c} \right) \right] \\ &\quad + j \text{LPF} \left[s(t, x) \sin \left(\frac{4\pi f_c x}{c} \right) \right] \\ &= A_D(t, x) e^{-j4\pi f_D x/c} \end{aligned} \quad (4)$$

where $\text{LPF}[\]$ represents the low-pass filtering process for the signal in bracket $[\]$, A_D is the Doppler signal intensity, and j is imaginary unit. As in Eq. (2), the Doppler signal intensity is obtained by applying the Hilbert transform. Figure 5 shows the example of Doppler signal and its envelope. The signal from the bubble had a clear peak, while the signal from the ice had a complex envelope shape due to interference.

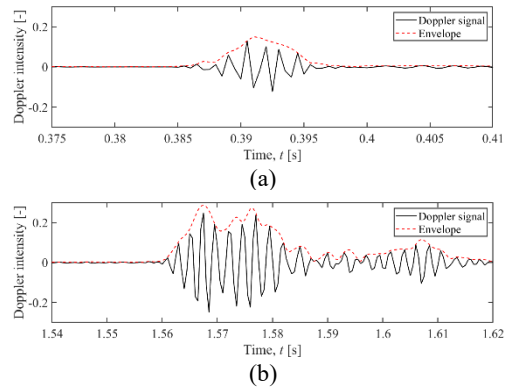


Figure 5: Example of Doppler signal and its envelope shape. (a) signal from a bubble, (b) signal from an ice.

An autocorrelation function is applied to the envelope within a certain time range, t_1 to t_2 .

$$r(\tau) = \frac{1}{r(0)} \int_{t_1}^{t_2} A_D(t, x) A_D(t - \tau, x) dt \quad (5)$$

As shown in Figure 6, the decay time of auto correlation coefficient was different between solid and gas phase. Thus, phase identification is possible by using the descending time of the coefficient as an evaluation function. Where the time until the coefficient is halved is τ_h , the evaluation function that discriminates between the solid and gas phases is expressed by the following equation.

$$J_{SG} = \frac{1}{\tau_h + 1} \quad (6)$$

These processes were applied to echo signals of Figure 3, and Figure 7 shows the identification results. In Figure 7, the color represents the probability of solid phase, which is normalized by the maximum value of the evaluation function in Eq. (6). The solid and gas phases were successfully discriminated.

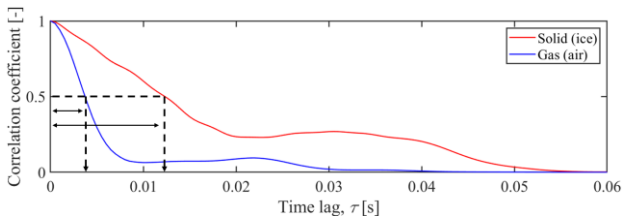
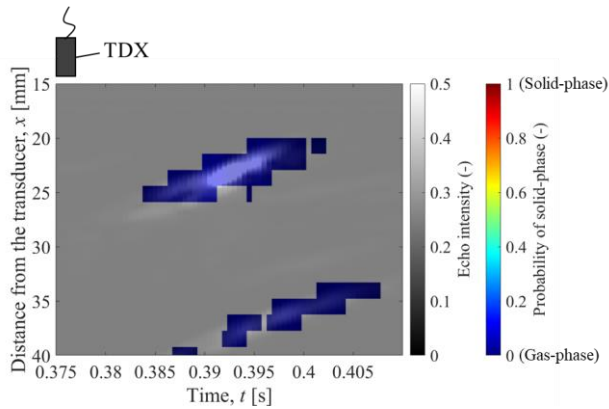
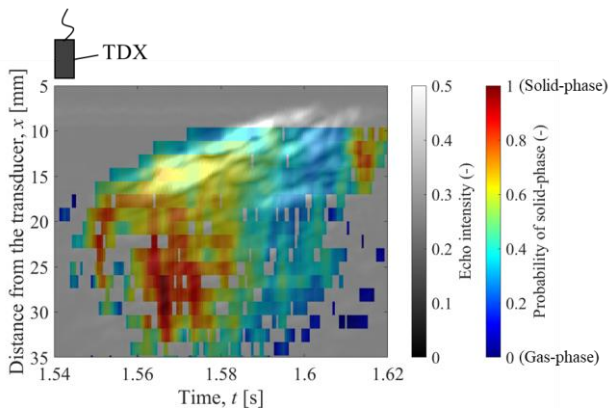


Figure 6: Comparison of auto correlation coefficient of Doppler signal envelope between solid (ice) and gas (air).



(a)



(b)

Figure 7: Results of solid and gas phase identification. (a) signal of bubble, (b) signal of ice.

4. Results and Discussion

Figure 8 shows the instantaneous velocity profile of each phase detected using the Doppler signal separated by the phase identification algorithm. Center graph is solid phase velocity profile, and bottom is bubble velocity profile, respectively. Velocity data were obtained at each phase location. The velocity profile of the solid phase was compared with that obtained by time-of-flight method using high-speed camera images; the spatial averaged solid phase velocities measured by UVP were 456, 459, and 424 mm/s for #1 to #3, respectively, and 475, 515, and 437 mm/s for the high-speed camera. The relative error was within 3-10 %, the validity of the developed method was confirmed.

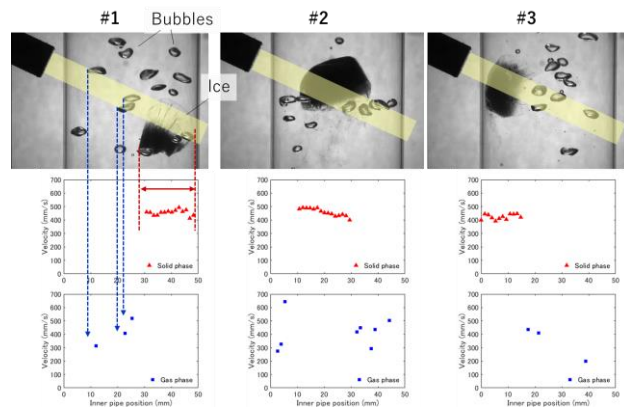


Figure 8: Instantaneous velocity profiles of each phase.

5. Summary

To realize the multiphase flow measurement with the UVP, solid-gas-liquid three-phase flow (ice-air-water system) in a vertical pipe was generated and the UVP measurement was applied to it. To identify the velocity data of each phase, the signal characteristics were extracted. The liquid phase (water) and other phases are separable by echo signal intensity, and the solid phase (ice) and gas phase (air) are shown to be potentially discriminable by detecting the speckle patterns formed in spatio-temporal signal intensity distribution. The method presented in this paper is affected by a combination of conditions such as solid phase size, acoustic impedance, ultrasonic frequency and element size. In the future, we will organize these influences and improve the measurement accuracy.

References

- [1] Agency for Natural Resources and Energy of METI HP: https://www.enecho.meti.go.jp/about/special/johoteiky/met_hanehydrate.html (2017)
- [2] Matukuma Y, *et al.*: Methane Hydrate Recovery Technology from Deep Seabed, Japanese J. Multiphase Flow 36 (2022), 398-406.
- [3] Shoji N, *et al.*: Leakage Detection and Flowrate Estimation With Three-Dimensional Vector Ultrasonic Velocity Profiler, Proceeding of the 12th Japan-Korea Symposium on Nuclear Thermal Hydraulics and Safety (2022), 1-5.
- [4] Wongsaroj W, *et al.*: 2D velocity vector profile measurement on bubbly flow using ultrasonic technique, Mechanical Engineering Journal 7 (2020), 1-15.

Study on Ultrasonic Echo Measurement for Vertical Pipe Gas-Liquid Multiphase Flow Containing Large Bubbles

Ryota Obana¹, Issei Watanabe¹, Kohei Maehara¹, Kazuya Shimizu² and Shu Takagi¹

¹ Dep. of Mechanical Engineering, Univ. Tokyo, 7-3-1 Hongo, Bunkyo-ku, Tokyo 113-8654, Japan

² Ocean Engineering Dep., National Maritime Research Institute, 6-38-1 Shinkawa, Mitaka, Tokyo 181-0004, Japan

For the effective operation of airlift pump, the method to achieve the flow state of upward liquid-gas multiphase flow in a pipe by ultrasonic measurement is investigated. In this study, echo measurement data taken from two different air-lift experiment systems are analyzed. Extracting one indicator from echo map on each ultrasonic emission and calculating the feature information of flow by machine learning is conducted. As feature information, flow pattern is chosen and applying a flow pattern identification model made in one experiment into another experiment is tried. As a result, a model scored high accuracy in one experimental system marked lower, but high to some extent accuracy in another system. It is implied that with the more quality and quantity of training data, the constructed flow pattern identification model can be converted to unknown experimental system.

Keywords: Ultrasonic Echo, Gas-Liquid Interface, Vertical Pipe Flow, Large Bubbles, Machine Learning

1. Introduction

In the depths of Japan's exclusive economic zone (EEZ), ranging from around 1000 to 6000 meters below the sea surface, significant deposits of valuable metals, including cobalt-rich crust and REY-rich mud, have been discovered. These abundant resources are found on the seabed. As an effective pumping method, an airlift pump is attracting the attention. It operates by introducing air into a vertical pipe, creating a difference in density between air and water, which induces upward flow. Airlift pumps are particularly advantageous due to their straightforward design, enabling equipment to be conveniently gathered on a ship. They have been successfully employed in extracting manganese nodules from depths close to 5000 meters [1].

The pumping process in an airlift pump involves gas-liquid multiphase flow within the pumping pipe, which exhibits different flow patterns, directly affecting pumping efficiency. While significant knowledge exists regarding changes in flow patterns in two-phase air-water flows, our understanding of flow patterns in gas-liquid phase flows in huge length of pipe (up to 6000 m), especially when the liquid phase is non-Newtonian or when gas-liquid-solid three-phase flow occurs due to the presence of mud and solid particles during pumping, remains insufficient. Actually, in 200 m length airlift experiment, gas-liquid flow show deviation from known flow pattern map [2]. Thus, it is crucial to continuously observe the flow state during the pumping process.

In this study, ultrasonic measurement is used as the observation method. Ultrasonic measurement offers several advantages, such as its suitability for opaque fluids and its non-invasive nature. The objective of this study is development of flow observation method for ascending gas-liquid multiphase flow in a pipe using ultrasonic measurement.

2. Experiment

In this study, data from two airlift experimental systems are used. In both system, cases with air-water two-phase flow are analyzed. Measurements are conducted on measurement section consisting of a vertical pipe made of transparent PMMA to allow flow visualization. An TDX is used to emit ultrasonic pulses and to receive the echo (ultrasonic intensity).

2.1 Experimental system 1

First system is constructed in the University of Tokyo. An overview of the apparatus is shown in Fig.1. The pipe inner diameter in the measurement section is 40 mm and the wall thickness is 5 mm. One ultrasonic transducer (TDX) is installed within a water jacket with inclination angle 5° in the measurement section and one high-speed camera taking images of the same point as the TDX, and the ultrasonic measurements and camera recording are synchronized. Emitted ultrasonic pulses consists of 4 waves with the frequency 4.17 MHz, and the repetition frequency is 3998 Hz. The distance between the TDX and pipe outer wall is roughly 20 mm, in the calculated far-field area of the ultrasonic wave. The flow rate of each phase is controlled by pump and mass flow controller. The flow rates vary in gas phase from 20 to 80 L/min, and in liquid phase from 15 to 75 L/min. The flow pattern map made on the basis of research by Taitel et al.[3] is shown in Fig.2.

2.2 Experimental system 2

As the second system, data from an airlift experiment conducted jointly by the University of Tokyo, Hokkaido University and National Maritime Research Institute (NMRI) in 2021 are used. The pipe inner diameter in the measurement section is 26 mm and the wall thickness is 2 mm. The gas flow rate is controlled by mass flow controller and the consequential liquid flow rate is measured by an electromagnetic flow meter. Flow rates vary in gas phase from 32 to 255 L/min. The flow pattern

map is shown in Fig.2. Three TDXs are attached to one pipe within water jackets, which ensure the far-field area distance (30 mm) and all the measurement is synchronized with high speed video camera. TDX2 measures the same point as camera, and other TDXs measures vertically distant points, which can observe locational variations of the flow structure. Additionally, TDX3 is set on the opposite direction with others, which can check the variation of flow structure by direction. In this study, however, 3 TDXs are used at the same time simply to make the amount of echo data achieved in one experiment larger. The setting of ultrasonic emission is the same as system 1.

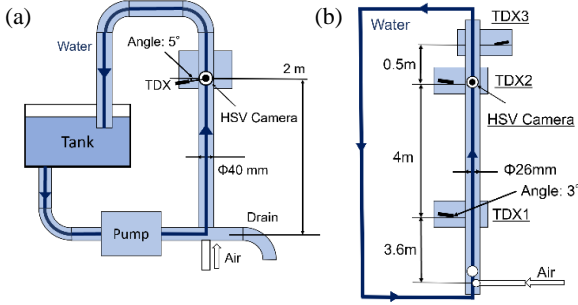


Figure 1: Experimental system in system 1 (a) and 2 (b).

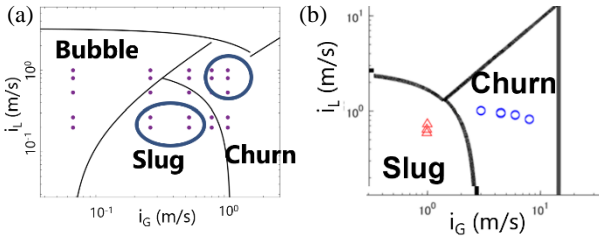


Figure 2: Flow pattern map in system 1 (a) and 2 (b).

3. Analysis Method

The ultrasonic measurement mechanism is conducted by emitting an ultrasonic beam towards the flow path and receiving the reflected wave by the same transducer. In this section, the reflection information is analyzed using the echo intensity technique [4]. This technique uses the extremely high ultrasonic reflectivity of the gas-liquid interface to locate the position of the gas-liquid interface. The visualization of the flow is in comparison with the camera image, in which each temporal variation of camera image and echo map is piled up along the timeline. An example of the visualization is shown in Fig.3.

In this study, identification by machine learning using the temporal variation of extracted echo property is conducted. Also, the efficiency of trained model conversion from one experimental system to another experimental system is examined. As the echo property, the “center of gravity”, which express the echo distribution in distance direction is used (Fig.3). In order to check the efficiency of data extraction, identification using actual echo map data is also conducted and the accuracy is compared. The data is split with sampling time calculated by dividing constant converted length (3.75 m) with mixture apparent velocity i_r . The label is achieved from the flow pattern map.

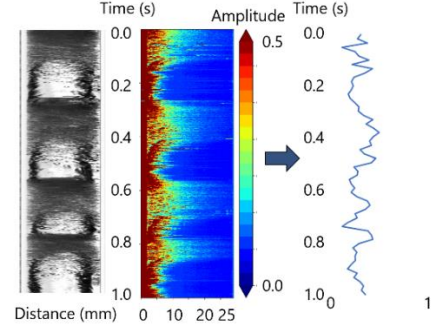


Figure 3: Example of comparison of processed camera image and echo map, and calculation of “center of gravity” of echo.

4. Result

In training, data taken from experimental system 1 are used. Flow pattern identification is conducted between slug flow and churn flow, using random forest algorithm with center of gravity data and convolutional neural network (CNN) with echo map data. As train data, 72 pieces are chosen from each flow pattern (144 pieces as a whole). Also, as test data 18 pieces are used from each and the slug/churn identification accuracy for all 36 pieces of test data is compared. As a result, the accuracy with center of gravity data is 0.92, which is higher than the accuracy with echo map data, 0.77. While the effectiveness of identification model with center of gravity data is demonstrated in experimental system 1, the convertibility of the model to another experimental system is examined. The identification model constructed in experimental system 1 is directly converted to the identification of slug/churn flow in experimental system 2 and the accuracy is checked. As test data, 13 pieces are used from each flow pattern. The accuracy with the test data (system 2) into the converted model (system 1) result in 0.69, which is lower than the accuracy with test data from system 1 (0.92). In this study, the conversion of flow pattern identification model constructed with data from one experimental system to another experimental system does not show as secure accuracy as in original experimental system.

Table 1: Accuracy of flow pattern identification model trained with “center of gravity” data from system 1 and tested with data from each system.

	System 1	System 2
Accuracy	0.92	0.69

5. Discussion

First, in flow pattern identification with echo data using machine learning, it is found that the appropriate data extraction makes training more efficient and improves the accuracy with limited train data. In this study center of gravity data is used, but there can be another effective data extraction. Second, the flow pattern identification model valid for experimental system 1 did not show the same degree of accuracy for system 2. Looking into the incorrectly identified cases, it turned out that in system 1 all of the incorrect cases are churn flow overestimated as slug flow, while in system 2 all the misidentified cases are slug flow overestimated as churn flow. In both incorrect

cases the flow structure is ambiguous in terms of flow patterns and difficult to decide slug/churn flow even from the flow structure. Thus, the difference of accuracy can be attributed to the low distinctiveness of the flow itself, not the identification method. In flow pattern, which is artificially divided and for which there is no practical significance in strictly defining the boundaries, misidentifying cases seen in this experiment are difficult to solve and not so important. Therefore, for the development of practically important flow pattern identification system, train data and test data should be taken from more distinctive cases.

6. Summary

In this study, ultrasonic measurement to vertical pipe gas-liquid multiphase flow containing large bubbles is conducted in two experimental systems. With the echo intensity data as extracted “center of gravity” data, flow pattern identification between slug and churn flow using machine learning is tried. In a single experimental system, the identification model shows accuracy higher than 0.9, which confirms the efficiency of machine learning flow pattern identification with data extraction. Also, it is implied that an identification model constructed in one experimental system can be directly converted to identification in another system with echo data of good quantity and quality in view of distinctiveness of flow pattern, even if some size scales of the systems are different.

Acknowledgement

The presenters thank Dr. Sotaro Masanobu, Mr. Satoru Takano, others in National Maritime Research Institute (NMRI), Prof. Yuichi Murai, Dr. Hyun Jin Park, Dr. Dongik Yoon and others in Hokkaido University for their cooperation. This work was supported by Ministry of Economy, Trade and Industry (METI) and Japan Organization for Metals and Energy Security (JOGMEC).

References

- [1] Yamazaki, T. Past, Present, and Future of Deep-Sea Mining. *Journal of MMIJ*, Vol. 131, pp. 592–596 (2015). (Japanese)
- [2] Shimizu, K. and Takagi, S., Study on the performance of a 200 m airlift pump for water and highly-viscous shear-thinning slurry. *Int. J. Multiph. Flow*, Vol. 142, 103726 (2021).
- [3] Taitel, Y., et al. Modelling flow pattern transitions for steady upward gas-liquid flow in vertical tubes. *AIChE Journal*, Vol. 26, No. 3, pp. 345–354 (1980)
- [4] Murai, Y. et al. Ultrasonic detection of moving interfaces in gas-liquid two-phase flow. *Flow Meas. Instrum.*, Vol. 21, pp. 356–366 (2010).

Influence of the shear stress on fine sediment exchanges with the substrate using UVP measurements

Romain Dubuis¹, Giovanni De Cesare¹

¹ Hydraulic Platform LCH, ENAC, École Polytechnique Fédérale de Lausanne, Lausanne, Switzerland

The dynamic of fine sediment in rivers is closely related to the interactions between fine particles, the riverbed and the flow conditions. The accumulation of fine sediment in the riverbed reduces vertical water exchanges and can have detrimental effects on the ecosystem of rivers. The conditions needed for the deposition of suspended sediment on the surface or inside the riverbed depend on the local flow conditions and have only been little studied. To explore this aspect, flow velocity measurements were performed using a UVP probe to evaluate the shear stress and assess the accuracy of the measurement in locations with different flow conditions along a flume. The shear velocity was inferred from the velocity profiles using the log-law equation. These results were then compared to the estimation of the shear stress using a simple backwater curve model. Results show that the shear velocity can be well evaluated when the flow conditions are not disturbed by protruding grains, even though gravel induce some variability in the results. The use of UVP to measure the shear stress with small relative water depth in comparison with bed roughness still represents challenges that might be addressed in future work.

Keywords: Fine sediment deposition, UVP, Shear velocity, Surface clogging, Velocity profile

1. Introduction

The excessive accumulation of fine sediment in the pores of riverbeds results in a reduction of vertical exchanges which can have detrimental effects on fish and benthos [1], as observed in numerous channelized or regulated Alpine rivers. The deposition of fine sediment transported as suspended load on riverbeds results in surface clogging when the flow conditions are unable to wash fine sediment deposited on top of the riverbed surface. Inner clogging can also take place when these fine particles are filtered inside the substrate but cannot deposit on the surface. [2]. When the shear stress of the flow mobilizes the riverbed, fine sediment trapped in the substrate is released, a process called declogging. As such, flow conditions have an important influence in the dynamics of fine sediment in rivers, in addition to other factors. Given the high variability of flow conditions in a river and the spatial dynamic of transported fine sediment, it is relevant to establish a relation between the local flow conditions and the type of clogging observed. The shear stress applied by the flow on suspended and deposited particles must be determined to understand correctly the process taking place. Ultrasonic velocity profilers (UVP) can be used to measure the local shear stress based on the velocity profile, and avoid complex numerical simulation in spatially varying flow conditions. However, the accuracy of the measurement using this method has first to be compared with theoretical values. In this context, the accuracy of shear stress measurement using a UVP is compared with theoretical values obtained from a simple eddy curve model, in the case of a bed of gravel and suspended sediment.

UVP probes have the advantage to allow for the measurement of the velocity profile with a limited impact on the flow. The turbid environment provided by the presence of suspended sediment in the case of clogging experiments is also adapted to this method [3].

2. Experimental setup and instruments

2.1 Flume

The deposition of fine sediment and the clogging process were analyzed using a 6.25 m long, 15 cm wide flume filled with a 31 cm thick layer of substrate (Fig. 1, see also [4]). The substrate was composed of a wide grain-size distribution of sand and gravel, ranging from 0.1 to 8 mm, with a small armoring of the surface layer, which had a geometric mean diameter d_{50} of 4.9 mm. A false bottom allowed an infiltration flow to be established through the substrate layer. Fine sediment in suspension was composed of quartz silt ranging between 0.1 and 63 μm , at a concentration ranging between 0.8 and 1 kg/m^3 . A continuously varying flow depth was set to analyze the type of deposition with varying flow conditions, with a discharge of 2.24 L/s and a water depth h_w ranging between 3.8 and 14.2 cm. The quantification of the clogging process was done by observing the chan-

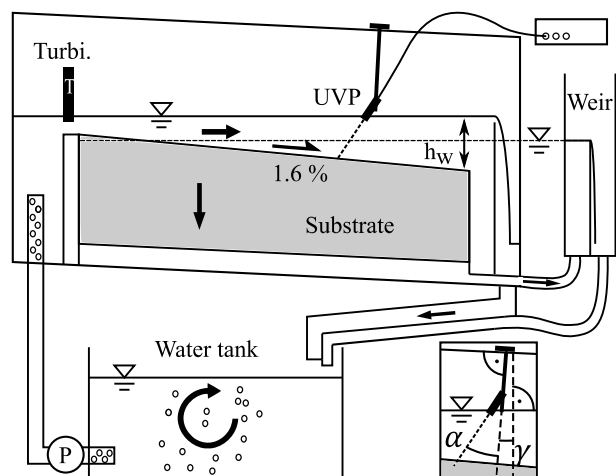


Figure 1: Experimental setup with regularly varied water depth and bed shear stress, equipped with a UVP probe.

ge in suspended fine sediment concentration, the final surface covered by fine sediment, samples of the substrate as well as through the change of the substrate permeability.

2.2 Ultrasonic Velocity Profiler

The flow conditions were measured in different locations along the flume by measuring the velocity profile at the center of the cross-section. To this effect, a Met-Flow 4 MHz UVP was used. The UVP probe was placed in the opposite direction of the flow, at an angle α of 30° to the perpendicular of the flume top slope (Fig. 1). The direction of the flow was assumed to be parallel to the flow surface. The flow velocity U was therefore inferred from the averaged measured velocity \bar{v}_m using the following relation:

$$U = \frac{\bar{v}_m}{\sin(\alpha + \gamma)} \quad (1)$$

Where γ is the angle between the surface flow and the top structure of the flume (see Fig. 1, detail).

3. Methodology

3.1 Data acquisition

Experiments were conducted to evaluate the deposition of fine sediment at the limit between surface clogging and inner clogging by observing the surface of the riverbed covered by fine sediment at the end of the experiment. The continuously decreasing shear stress provided by the increase of the water depth along the flume had to be determined to link the observed phenomena with the flow conditions. Velocity profiles were measured at 13 locations along the flume, distant of 50 cm each.

The tip of the UVP probe was positioned right below the water surface, at a distance x from the inlet. Silt particles in suspension, which are responsible for the clogging of the bed, were used as seeding to reflect the signal. The longitudinal position of the probe was occasionally shifted by a few centimeters when local flow disturbances due to the irregular bed surface resulted in a velocity profile that deviated significantly from the theoretical log-law profile.

The UVP was set to measure points from 5 mm from the probe, with one measurement point every 0.74 mm, which corresponds to a vertical resolution of 0.64 mm. A total of 200 velocity profiles were measured in each location, with 256 repetitions for each profile. The voltage was set to 60 V, and the echo gain started at 3 and ended at 6.

3.2 Processing of the data

The raw data were then processed to obtain the shear velocity, in a similar way to the method used by [3] or [5]. The logarithmic law of the wall defines the velocity profile as [6]:

$$U = \frac{u_*}{\kappa} \ln\left(\frac{z}{z_0}\right) \quad (2)$$

Where κ is the von Karman's constant, taken as 0.41, u_* is the shear velocity and z_0 the bed roughness

dimension. Assuming a rough turbulent flow, the bed roughness can be defined as $z_0 = k_s/30$, where k_s is Nikuradse's roughness, situated in the range $2d_{50} \leq k_s \leq 3d_{90}$ [5], and resulting, for the composition of the bed surface, in $d_{50}/12 = 0.38 \text{ mm} \leq z_0 \leq d_{90}/10 = 0.75 \text{ mm}$. In a similar way to [5], no form drag correction was applied since the bed is flat. A linear regression between the velocity profile and the logarithm of the dimensionless depth z/z_0 was used to find the shear velocity. The regression was restricted to measurements situated in the interval $0.7 \cdot d_{50} < z < 0.25 \cdot h$, with h the water depth, as suggested by [7], to stay within the log-law region and avoid influence of the bottom particles.

4. Results

4.1 Velocity profiles

The regression of the velocity measurements within the selected interval are presented in Figure 2, at 13 different locations along the flume. The regression was performed using $z_0 = 0.38 \text{ mm}$, a value situated at the lower end of the proposed range.

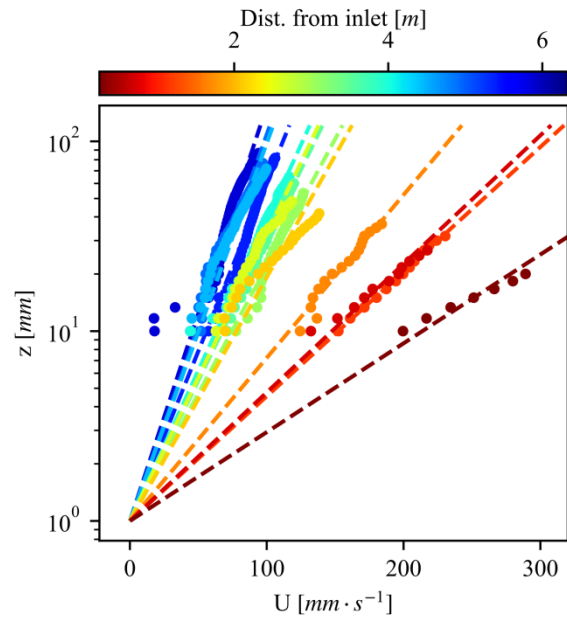


Figure 2: Velocity profiles in the log-law interval as a function of the depth (y-axis), expressed with a log-scale. The dashed lines correspond to the linear regression of each profile.

Outside of the selected interval, the measurement data deviates from the theoretical log-law curve and are therefore not used in the regression. In consequence, the resulting velocity profile obtained from the fit deviates in the upper part of the flow depth, especially for velocity profiles measured at the upstream part of the flume where the flow velocity was higher (Fig. 3).

The R^2 values of the fits for the different regressions lay in the range between 0.81 and 0.99, with the lowest value (<0.9) attributed to a section at the end of the flume (Fig. 2, dark blue) and at around 2.2 m (Fig. 2, yellow).

4.2 Comparison of shear stress with backwater curve model

The low value of z_0 used for the regression allows to obtain shear velocities that correspond approximately to

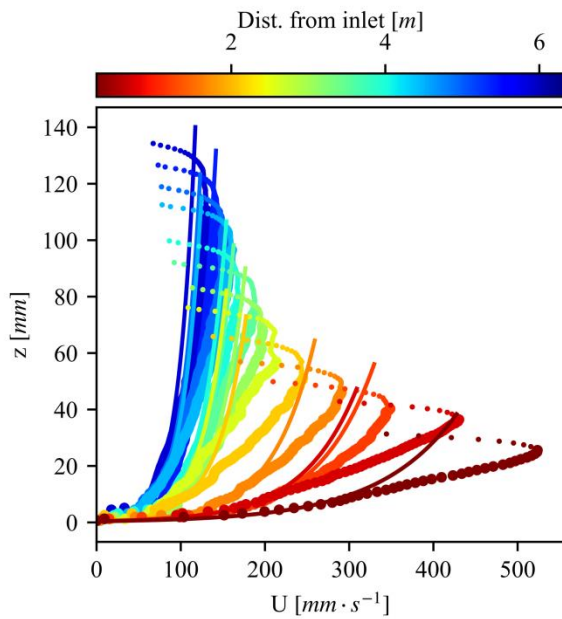


Figure 3: Full velocity profiles in each measured section along the flume (bullets) as a function of the depth (y-axis). The continuous lines correspond to the log-law velocity profile obtained from the regression of Fig. 2 up to the water surface. Small bullets show measurement affected by UVP transducer.

the theoretical shear velocity calculated using a simple backwater curve model, as shown on Figure 4. The backwater curve model was calibrated using water surface and bed level measurements of multiple experiments with the same substrate and wall roughness. Using a more commonly accepted value of $k_s = 3d_{90}$ [8], the values of the shear velocity using the UVP measurements are overestimated in comparison with the theoretical values obtained from the backwater curve model. In this case, the theoretical value is about 70% of the measured shear velocity.

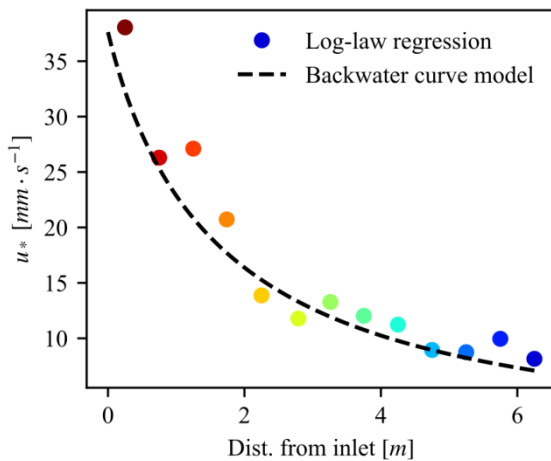


Figure 4: Comparison between the shear velocity obtained by UVP measurements and by the backwater curve model.

4.3 Clogging process at the limit between surface and inner clogging

Based on the analysis of the riverbed surface covered by fine sediment at the end of the experiment, using pictures of the surface [9], it is possible to express the relation between the type of clogging and the shear stress (Fig. 5). The surface covered by fine sediment corresponds to the proportion of white surface (fine sediment) in contrast with the darker substrate, analyzed pixel by pixel.

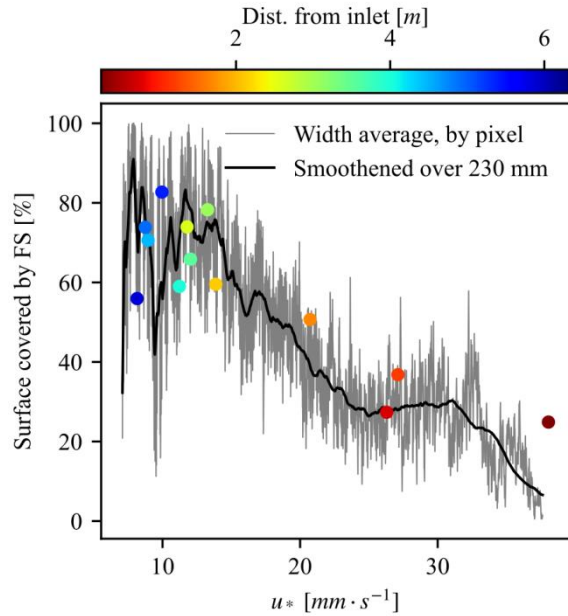


Figure 5: Surface covered by fine sediment as a function of the shear velocity, using theoretical (continuous line, from calibrated backwater curve) and measured (bullets) shear velocity. Pixels used in the analysis of covered surface correspond to a distance of 0.23 mm, longitudinally.

The surface covered by fine sediment decreases regularly with the increase of the shear velocity, without specific threshold, from values of around 80% (Fig. 6c), until the covered surface reaches a value of about 20% for shear velocities over 25 mm/s (Fig. 6a). This last case corresponds to the usual cover observed in experiments with inner clogging.

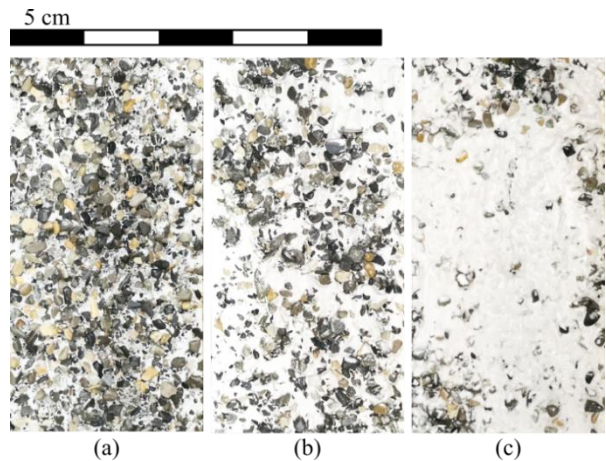


Figure 6: Surface covered by fine sediment in the case of (a) inner clogging, (b) in the transition and (c) surface clogging.

5. Discussion

5.1 Data acquisition

The rough surface of the riverbed, with the largest grains reaching 8 mm, in comparison with the water depth (38 to 142 mm) implies that the velocity profile can change significantly depending on the location of the probe. The arrangement of the grains at the bed surface can modify the flow on an important part of the flow depth, for example in the presence of secondary currents. To this regard, the presence of secondary current could be checked by using a second transducer with a different angle. Alternatively, the ADV method could provide a more detailed measurement of the local flow [10]. Since the average flow conditions are relevant and secondary currents occur in a limited area of the bed surface, the UVP method allows obtaining sufficiently detailed results for the studied case. The definition of the bottom of the flow is also a source of errors since the probe may capture the presence of intra-gravel flow when the signal is directed between gravel particles or be affected by the presence of protruding grains. This aspect implies testing different locations to obtain good profiles. The reduced velocity near the surface of the water as observed in Figure 3 can be attributed to the influence of the UVP transducer and does not correspond to the real velocity close to the water surface.

5.2 Estimation of the shear stress

Using the logarithmic law equation to estimate the shear velocity gives accurate results when a well-developed velocity profile can be obtained. This method depends on factors like the bed roughness, which needs to be estimated, and can provide different results depending on the assumptions. The results obtained through this method should be therefore used with precaution, especially when no calibration can be performed to evaluate the best value of the bed roughness, for example.

In a similar way to what observed [7], the range over which the log-law regression is applied can be extended to larger values than $z = 0.25 \cdot h$, for instance $0.3 \cdot h$, with a similar quality of the fit, although [7] use an ADV method, providing 3D detailed measurements.

5.3 Type of clogging

The smooth transition between inner clogging and surface clogging observed along the flume during this experiment is attributed to the hiding-exposure effect [5], [11]. Large protruding grains of the substrate can reduce the shear stress in the interstices of the riverbed surface which allows for the deposition of fine sediment reaching these areas. A more systematic examination of flow velocity near the substrate surface would provide a better understanding of how the transition between the two types of clogging is related to the interaction between flow and bed roughness.

The discrete measurement of the shear velocity reveals the relation that exists between the surface covered by fine sediment and the shear velocity. However, assessing the type of clogging depending on a single measurement

should be taken with precaution since the local measured value can vary on very short distance.

6. Conclusion

The evaluation of the bed shear stress by using velocity profiles obtained from UVP probes provided similar results to the one obtained on the basis of the flow and geometric characteristics of the flume. Due to the relatively large bed roughness, obtaining usable velocity profiles required to avoid perturbations of the flow due to protruding grains. This method is able to estimate the shear stress that defines the type of clogging, taking advantage of the suspended material responsible for the clogging process. In larger applications with different bed morphologies, this method would allow estimating the local flow conditions and related type of clogging.

References

- [1] J. I. Jones, J. F. Murphy, A. L. Collins, D. A. Sear, P. S. Naden, et P. D. Armitage, « The Impact of Fine Sediment on Macro-Invertebrates », *River Research and Applications*, vol. 28, n° 8, p. 1055-1071, 2012, doi: 10.1002/rra.1516.
- [2] R. Dubuis et G. De Cesare, « The clogging of riverbeds: A review of the physical processes », *Earth-Science Reviews*, vol. 239, p. 104374, avr. 2023, doi: 10.1016/j.earscirev.2023.104374.
- [3] J.-N. Saugy, A. Amini, et G. De Cesare, « Flow structure and grain motion assessments of large river widening in a physical model using ultrasonic Doppler velocity measurements », *Exp Fluids*, vol. 63, n° 7, p. 115, juill. 2022, doi: 10.1007/s00348-022-03430-9.
- [4] R. Dubuis et G. De Cesare, « Influence of Vertical Fluxes on the Clogging of Riverbed by Fine Sediment », in *39th IAHR World Congress*, in IAHR. Granada, 2022, p. 659-666. doi: doi:10.3850/IAHR-39WC2521711920221145.
- [5] C. J. McCarron, K. J. J. Van Landeghem, J. H. Baas, L. O. Amoudry, et J. Malarkey, « The hiding-exposure effect revisited: A method to calculate the mobility of bimodal sediment mixtures », *Marine Geology*, vol. 410, p. 22-31, avr. 2019, doi: 10.1016/j.margeo.2018.12.001.
- [6] H. Schlichting et K. Gersten, *Boundary-Layer Theory*, 8th revised ed. Springer Science & Business Media, 2000.
- [7] F. Bagherimiyab et U. Lemmin, « Shear velocity estimates in rough-bed open-channel flow », *Earth Surface Processes and Landforms*, vol. 38, n° 14, p. 1714-1724, 2013, doi: 10.1002/esp.3421.
- [8] G. H. Keulegan, « Laws of Turbulent Flow in Open Channels », *Journal of Research of the National Bureau of Standards*, vol. 21, p. 707-741, 1938.
- [9] R. Dubuis et G. De Cesare, « Limits between surface and inner clogging of riverbed by fine sediment », in *proceedings of River Flow 2022*, 2022.
- [10] D. Duma, S. Erpicum, P. Archambeau, M. Piroton, et B. Dewals, « Velocity and Turbulence Measurements for Assessing the Stability of Riverbeds: a Comparison between UVP and ADV », *Proceedings of the 11th International Conference on Hydrosience & Engineering*, p. 539-544, 2014.
- [11] W. Wu, S. S. Y. Wang, et Y. Jia, « Nonuniform sediment transport in alluvial rivers », *Journal of Hydraulic Research*, vol. 38, n° 6, p. 427-434, nov. 2000, doi: 10.1080/00221680009498296.

Characterization of Thruster-Induced Turbulence for Fine Sediment Suspension

Montana Marshall, Azin Amini, Giovanni De Cesare¹, and Andre Luis Stakowian²

¹ School of Architecture, Civil and Environmental Engineering (ENAC), Platform of Hydraulic Constructions (PL-LCH), École Polytechnique Fédérale de Lausanne (EPFL), Switzerland

² Graduate School of Electrical Engineering and Computer Science (CPGEI), Federal University of Technology-Paraná (UTFPR), Brazil

Reservoir sedimentation is a key challenge for storage sustainability because it causes volume loss, affecting hydropower production capacity, dam safety, and flood management. A preliminary EPFL study proposed and studied an innovative device (called SEDMIX), which uses water jets to keep fine sediments near the dam in suspension and ultimately allows the sediments to be released downstream. The jets induce a rotational flow which creates an upward motion and keeps fine sediments in suspension near the dam and water intakes. The sediment can then be continuously released downstream through the power waterways at acceptable concentrations, without additional water loss or required energy. The efficiency of the SEDMIX device has been confirmed through experimental simulations and numerical analyses at EPFL. This study involves updated experimental simulations to include thrusters in the device design instead of water jets, because they lead to a less complex arrangement that requires less energy to operate. The thruster-induced turbulent kinetic energy is observed and characterized using Ultrasonic Velocity Profiling (UVP) to determine optimal device configurations for effective sediment release.

Keywords: reservoir sedimentation, storage losses, sediment routing, turbidity currents, dam safety, sediment suspension, thrusters, hydrodynamics, long range Ultrasonic Velocity Profiling (UVP), turbulence, Met-Flow

1. Introduction

1.1 Scientific Background

In high-altitude alpine reservoirs, turbidity currents are the main inflow process for sediments [1]. Turbidity currents mainly occur during floods, when a sediment-laden river enters the reservoir downstream of the root delta. These currents transport fine sediments downstream to the deepest part of the reservoir, close to the dam. This causes two main issues: increased sedimentation at the dam (decreasing the available storage volume for hydropower and flood control), as well as negatively impacting operation of the bottom outlets and/or water intakes.

Reservoir sedimentation is a key challenge for storage sustainability because it causes volume loss, affecting hydropower production capacity, dam safety, and flood management. According to a recent UN University study [2], it is forecasted that dams around the world will lose nearly a quarter of their storage capacity due to sedimentation by 2050. This storage loss rate is of particular concern for mid-altitude reservoirs which must regularly conduct costly sediment management operations which affect their sustainability. The SEDMIX device is designed to help solve this exact issue: minimizing the ongoing sedimentation issues in existing dams.

1.2 Existing Technologies

To combat reservoir sedimentation and the negative impacts of turbidity currents, there are several sediment management strategies that are being investigated and applied worldwide. These include venting, flushing, and mechanical dredging, among others. While these strategies have benefits, they also have practical challenges that hamper using them as successful techniques [3].

For example, venting allows for the release of sediments

downstream during a flood event but requires a substantial amount of water release in the process (decreasing hydropower availability and production). Mechanical dredging allows for removal of large quantities of deposited sediment but is costly and requires ongoing maintenance and disposal of the dredged material. Flushing is more cost effective but may require powerplant outage for a limited period and may have larger potential for adverse downstream impacts.

This study focuses on an innovative concept for a system that does not have as many negative aspects when it comes to dam-reservoir operation. The SEDMIX device is a more flexible and versatile solution that has the potential to be employed in reservoirs with a diverse range of design details and location-specific criteria than each of the solutions mentioned above.

1.3 SEDMIX Device Concept

A PhD thesis that was completed at EPFL PL-LCH [4] proposed and lab-tested an innovative system (called SEDMIX), which used water jets to keep fine sediments near the dam in suspension and allowed them to be routed downstream. This study involves updated experimental simulations to include thrusters in the device design, instead of jets, because it leads to a less complex arrangement that requires less energy to operate.

The thrusters induce a rotational flow which creates an upward motion. This thruster arrangement is beneficial for sediment release as it keeps fine sediments in suspension near the dam and water intakes. The sediment can then be continuously routed downstream through the power waterways at suitable concentrations, without additional water or energy loss.

The SEDMIX device consists of two rigid parts: one floating at water level and one on the basin bottom holding a multi-thruster manifold frame (shown in Figure 1). Once constructed, the thruster manifold frame will be suspended from a floating platform and lowered underwater into position. As such, the system can be mobile and can be moved around the reservoir to find the position that provides optimal sediment evacuation. The facility is modular and combines the use of different materials, taking into consideration structural resistance, weight, workability, aging properties, and cost.



Figure 1: Conceptual graphic showing SEDMIX design (source: PL-LCH)

2. Experimental Setup

This study involves a physical experimental model to study thruster performance and the ability of the SEDMIX device to keep fine sediments in suspension. The goal of the study is to better understand the influence of the SEDMIX device on reservoir hydrodynamics. The experimental setup is shown in Figure 2 and described in the following sub-sections.

The experimental setup allows for testing different thruster configurations and parameters, including the number, size, location, and angle of the thrusters. Three ultrasound transducers are used to measure vertical velocity profiles in the water column (Figure 2). At steady state, the locations of the transducers (and therefore the measured profiles) are systematically moved using a robotic transversal system to ultimately develop a two-dimensional grid of velocity profiles and calculated turbulence.

2.1 Laboratory Tank

The physical experiments are conducted in a prismatic tank with vertical walls. The tank has an inner basin length of 4.0 meters (m), an inner width of 1.97 m and a basin height of 1.50 m (for a total volume of 11.8 m³). The bottom of the tank is a steel plate. Most of the front and right lateral walls are made of glass, providing transparency for visual observations, and the other walls are made from steel plates.

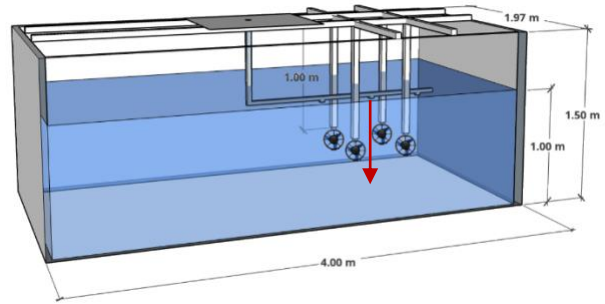


Figure 2: Experimental Setup (source: PL-LCH). Red line shows the direction of the UVP measurement.

2.2 Thrusters

This study involves the use of four thrusters, set up in a grid as shown in Figure 3.

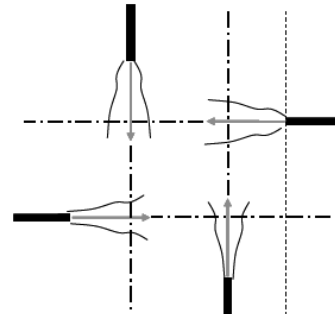


Figure 3: Plan view of thruster geometry (source: PL-LCH)

The thrusters used for this experiment are Blue Robotics T200 thrusters [5], which consist of a fully flooded brushless motor with encapsulated motor windings and stator as well as coated magnets and rotor (see Figure 4). The thruster body and propeller are made from polycarbonate plastic and the only exposed metal components are made from marine grade 316 stainless steel.

Based on information from the manufacturer, the thrusters have a (approximate and theoretical) maximum velocity output of 4.5 m/s, and a maximum discharge of 0.0125 m³/s. The thrusters are supported with a movable steel frame, as shown in Figure 2.

The thrusters can generate thrust both in the forward and reverse directions, although the reverse direction has a lower force and efficiency. The thruster throttle can be controlled using a programmed electronic speed controller (ESC), which then uses a Pulse Width Modulation (PWM) signal to control the throttle of the thruster.

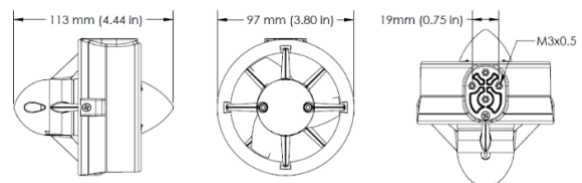


Figure 4: Thruster T 200 Schematic (source: Blue Robotics)

2.3 Long-range Ultrasonic Velocity Profiling (UVP) transducers

Met-Flow long range Ultrasonic Velocity Profiling (UVP) transducers (2 MHz) are used to study induced velocities in the tank, as ultimately, turbulent kinetic energy.

The Ultrasonic Velocity Profiling technique (UVP), using the UVP DUO profiler by Met-Flow, measures instantaneous velocity profiles of liquid flows by using the Doppler shift of echoes reflected by small particles flowing with the liquid. The UVP technique is quasi non-intrusive and hence, does not disturb the flow circulation.



Figure 5: Ultrasound Transducer (image provided by Met-Flow)

For this experiment, the transducers are mounted to a horizontal rod at the top of the water column and are pointed downward to obtain velocity profiles (see Figure 2). The transducer locations are easily changed because they are mounted using a robotic arm that is remotely controlled, allowing for measurements at known and precise locations.

Table 1 outlines the parameters used to take measurements using Met-Flow software and the UVP DUO profiler.

Table 1: Summary of Ultrasonic Doppler Velocity Profiler Measurement Parameters

Parameter	Value
Ultrasonic Frequency	2 MHz
Transducer Diameter	24 mm
Number of Cycles	4
Channel Width	1.48 mm
Number of Repetitions	128
Sound Velocity	1480 m/s
Output Voltage	90 V
Number of Samples	1024

3. Methodology

The focus of this experiment is to test the influence of different thruster and geometric configurations on the hydrodynamics in the experimental tank. Variables that were tested during this study include:

- the location of the thrusters (distance between each thruster and off-bottom clearance),
- the angle of the thrusters (with respect to horizontal), and
- thrust output of each thruster (RPM).

The tank is a closed system that does not have any incoming or outgoing flow. The water height is kept constant at a depth of 1.0 m. The temperature of the water was kept at room temperature (between 15 - 20°C), and as such, the viscosity does not vary significantly. The experiments are conducted without specific particle tracers, instead using natural impurities present in the water for echoes (dust, organic material, etc.).

3.1 Geometric Parameters

Figure 6 outlines the geometrical parameters of the tank and thruster system.

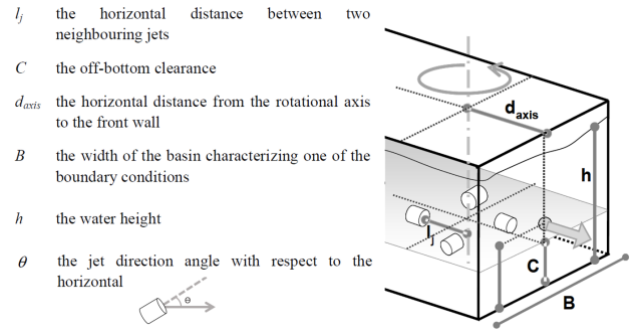


Figure 6: Geometrical parameters regarding the thruster and tank configuration (adapted from [4])

3.2 Experimental Parameters and Configurations

Table 2 outlines the different experimental configurations that are performed for this study, starting with the control (which was adapted from the optimized configuration found in [4]). The subsequent experiments then test one variable at a time, keeping all other variables constant (and equal to the control case).

Table 2: Experimental Parameters and Configurations (see Figure 6 for parameter descriptions)

Experiment	Thrust [RPM]	l_j [m]	C [m]	Θ [°]
Control	1550	0.5	0.5	0
1a	1530	0.5	0.5	0
1b	1570	0.5	0.5	0
1c	1600	0.5	0.5	0
2a	1550	0.4	0.5	0
2b	1550	0.6	0.5	0
2c	1550	0.7	0.5	0
3a	1550	0.5	0.4	0
3b	1550	0.5	0.6	0
3c	1550	0.5	0.7	0
4a	1550	0.5	0.5	+ 45
4b	1550	0.5	0.5	- 45

4. Results

The first measurement that is considered for each of the different experimental configurations is the water velocity profiles and the maximum velocity observed. Figure 7 shows an example of a velocity profile measured using the transducers and UVP DUO by Met-Flow (see orientation of transducer in Figure 2). The use of three transducers, pointed in the downward direction, will allow for the characterization and quantification of velocity in the water column in a vertical plane.

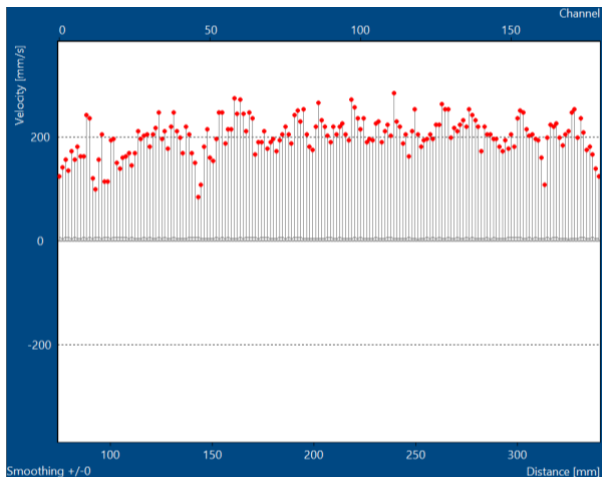


Figure 7: Preliminary UVP results for Experimental Configuration 1a measuring the velocity profile in the water column (Met-Flow UVP Software Version 3)

Using information from the velocity profiles obtained during the different experimental configurations, turbulent kinetic energy is calculated. The optimal geometric configuration will be one that results in inducing the magnitude of turbulent kinetic energy that keeps fine sediment in suspension. Mean kinetic energy, which represents the quantitative measure of the intensity of turbulence and the fluctuation in flow velocity, will be calculated using the velocity profile information obtained from the UVP analysis and characterized and compared in different zones of the measured cross-section.

Calculation of the turbulent kinetic energy for the experimental configurations outlined in Table 2 will allow for the determination of the optimal geometric and operational parameters that result in flow conditions that maximize sediment suspension. In a real reservoir, these flow characteristics would then lead to optimal sediment release downstream.

5. Ongoing research

In parallel to this study, numerical simulations of this experimental setup are also being performed in order to compare results to the physical experiment, validate the measurements from the ultrasonic transducers, and test additional configuration and parameter combinations.

Ultimately, the results obtained from this study will aid in the next step of the project, which is prototype

implementation of a SEDMIX device in a reservoir for further testing and observation in real, full-scale conditions. The experimentally established UVP transducer configuration for measuring velocities, flow patterns, and ultimately device efficiency, will be used to define locations of field measurements using UVP. Information gleaned from these studies will allow for continued optimization of the device and industrial development for use in reservoirs that have fine sedimentation issues.

6. Acknowledgements

The authors would like to thank everyone who helped to make this experiment happen. Cédric Bron designed the thruster structure and helped with the selection, setup, and programming of the different measurement tools. Kilian Gertsch and Kosta Nikolav also helped with the design of the experimental tank and constructed the specific experiment elements.

7. References

- [1] De Cesare, G. Boillat, J. 1998. Alluvionnement des retenues par courants de turbidité. Thèse EPFL, 1820.
- [2] Perera, D., Williams S., and Smakhtin V. 2023. Present and Future Losses of Storage in Large Reservoirs Due to Sedimentation: A Country-Wise Global Assessment. In Sustainability 15, no. 1: 219.
- [3] Chamoun S., De Cesare G., Schleiss A. J. 2016. The importance of venting turbidity currents on the sustainable use of reservoirs. In the Proceedings of Hydro Conference 2016, Montreux, Switzerland.
- [4] Jenzer-Althaus J., De Cesare G., & Schleiss A. J. 2014. Sediment evacuation from reservoirs through intakes by jet-induced flow. In Journal of Hydraulic Engineering, 141 (2).
- [5] Blue Robotics Thruster T 200 (designed and manufactured by Blue Robotics)
<https://bluerobotics.com/store/thrusters/t100-t200-thrusters/t200-thruster-r2-rp/>
- [6] Amini A., Manso P., Lindsey N., Venuelo S., Schleiss A.J. 2017. Computational hydraulic modeling of the sediment stirring and evacuation through the power waterways at the Trift reservoir. In the Proceedings of the Hydro Conference 2017. Spain.
- [7] Onate-Paladines, A., Amini A., De Cesare G. (2019). Computational Modelling of Fine Sediment Release Using SEDMIX Device with Thrusters. SCCER-SoE Annual Conference 2019.
- [8] Schleiss A. J., Franca M. J, Juez C., De Cesare G. 2016. Reservoir Sedimentation. In Journal of Hydraulic Research. Volume 54 (6), pp. 595-614.

Physical modeling and UVP monitoring yield an efficient protection of a lake reedbed from erosion

Vecsernyes Zsolt¹, Andreini Nicolas¹, Wohlwend Florent¹, Gobat Karine¹, Jaeger Amandine¹, Venturi André²

¹ Laboratory for Applied Hydraulics of HEPIA, University of Applied Sciences Western Switzerland, HES-SO, Geneva, Switzerland

² CERA civil engineers SA, Geneva, Switzerland

The Lake Geneva revitalisation program includes among various measures the implementing of reedbeds along the artificialized riprap shoreline. The vegetation and its substratum must be protected against wind induced harms due to wave energy and currents. Since embankment-dikes in Suisse lakes are not permitted, according to the Suisse Federal Act on the Protection of Waters (RS 814.20), the Laboratory for Applied Hydraulics (LHA) of HEPIA has been mandated by the *Service du lac, de la renaturation des cours d'eau et de la pêche of Geneva* to carry out a detailed analysis by physical modelling of a double vertical-wall breakwater structure. The metal-wood structure designed by CERA civil engineers had to be optimized at the LHA, to achieve high wave-energy dissipation. In an experimental wave tank of the LHA, reedbed resistance and its substratum erosion potential were tested under 50-year return period wind conditions. The structural strains were also determined, under 100-year return period wind. The breakwater developed at the LHA prevents efficiently the reedbed against wind-wave induced harms and substratum erosion, as verified by Met-Flow UVP probes and described in the present study.

Keywords: physical hydraulic model, Met-Flow UVP probes, reedbed protection, breakwater, lake revitalisation

1. Introduction

The future Coligny reedbed will constitute a revitalisation measure for a portion of the artificialized Lake Geneva shoreline (Fig. 1), and an ecological compensation linked to the planned public access and leisure activities such as bathing. The project fulfils the Geneva renaturation master plan (PDCn 2030) and the Swiss federal laws, and classifies the Coligny revitalisation program as 1st priority.



Figure 5: The revitalisation project is situated on the east bank of the Lake Geneva shore.

The project site extends over 650 m along the Coligny shoreline. The primary lacustrine facilities are, a submerged wave-breaker parallel to the shoreline and a riprap belt defining the edge of the reedbed. Further structures are also planned such as a public access and a recreational platform. The waterbody between the shoreline and the breakwater will also benefit from the protection of the latter.

The lacustrine reedbed has to be protected from threats due

to wind induced waves. The innovative breakwater design, developed at the LHA, and the achieved wave energy dissipation yielding an adequate protection of the reedbed are detailed in [1] and [2].

The present paper describes how shears stress on the reedbed substratum is reduced thanks to the breakwater, helping the resilience of the revitalisation measure.

2. Experimental setup

The experimental study was carried at the Laboratory for Applied Hydraulics of HEPIA-Geneva on a physical hydraulic model (Fig. 1) obeying Froude similitude at 1:25 geometrical scale. Scales of typical linked hydraulic parameters are presented in Table 1, where P index stands for prototype (natural condition) and M index designates model.

Table 1 Scales of typical hydraulic variables due to Froude similitude

Wave length L (m), Height h (m), Pressure P (m)	$\frac{L_P}{L_M} = \frac{H_P}{H_M} = \frac{P_P}{P_M} = \lambda$	25
Wave period and time t (s), Wave celerity and flow velocity U (m/s)	$\frac{t_P}{t_M} = \frac{U_P}{U_M} = \lambda^{1/2}$	5
Wave frequency f (1/s)	$\frac{f_P}{f_M} = \lambda^{-1/2}$	0.20

The 6.32 m long and 0.385 m wide wave tank was equipped with an air-piston wave generator. Lake bathymetry was reproduced over a path of 145 m (prototype) from the shoreline. As shown in Fig. 2 and 3, the model of the reedbed was implemented at the leeward extremity of the wave tank, in front of the shoreline. The

reedbed substratum was made of rigid expanded polystyrene, and the vegetation of flexible synthetic fiber planted in the substratum. The breakwater could be placed

at various distances from the shoreline. Its modular structure, presented in Fig. 4, allowed several geometrical configurations.

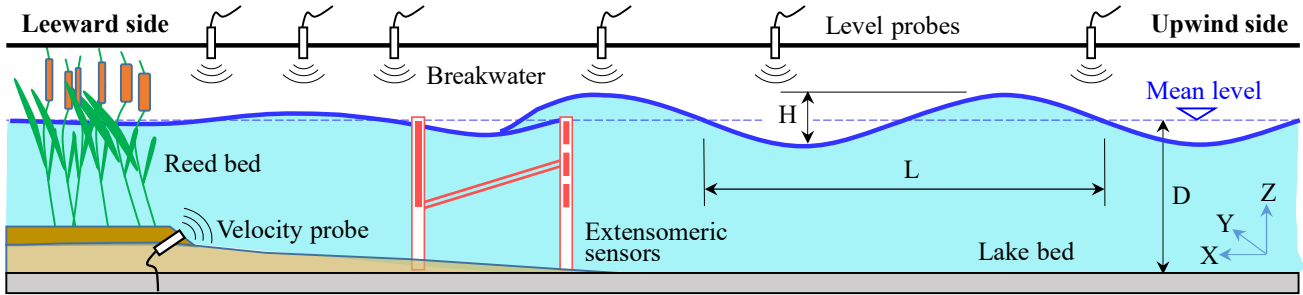


Figure 2. Hydraulic scheme of the physical model (wave tank). Wave propagation from the right to left.

The wave tank was mounted with six UNAM (Baumer) ultrasound level probes placed at six strategic points. A Met-Flow UVP 2 MHz ultrasound velocity probe was installed on the edge of the reedbed, with 30° from horizontal. Table 2 shows the UVP measurement ranges.

Table 2 Measurement ranges of the Met-Flow 2MHz UVP probe.

Velocity range (m/s)	Velocity resolution (mm/s)	Distance range (m)	Spatial resolution (mm)	Acquis. time (ms)	Sampl. frequ. (Hz)
0.09	0.3	3	1.48	132	8
49	193	0.006		1	4170

The breakwater was equipped with HBM SG LE11 50 Hz 2.5 V extensomeric sensors glued at spots where the poles were embedded in the modelled lake-bed (Fig. 4).

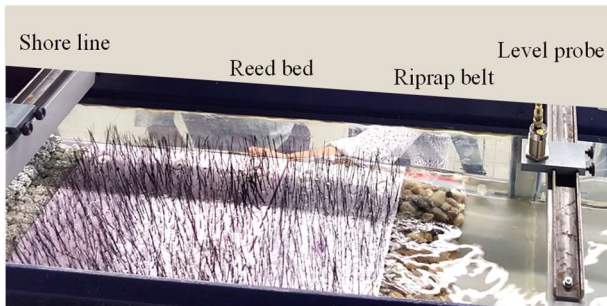


Figure 3: Model of the reedbed in the experimental wave tank. Substratum: rigid expanded polystyrene; vegetation: flexible synthetic fiber; riprap belt: agglomerated gravel.

The primary geometry of the breakwater was provided by CERA engineers. It was designed with two separate vertical walls, facing the waves (Fig. 4). While these walls on the prototype are planed of wooden planks, those of the model were built in metal. The leeward wall is designed with a solid surface and the upwind one with a definite hollow ratio.

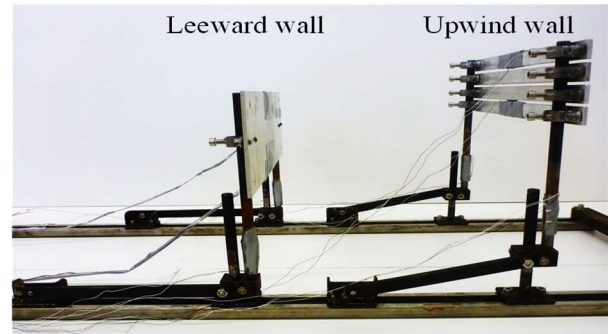


Figure 4: Model of the breakwater, composed of two parallel vertical panels. Extensomeric sensors were glued to the steel spots (S235 European norm EN 10 025 and ECISS IC 1).

On the model, the steel structure of the frame, poles and beams were built of the same material as planned on the prototype (S235 European norm EN 10 025 and ECISS IC 1), in order to achieve a consistent physical compartment due to same specific mass, Young elasticity, Poisson coefficient.

Typical prototype dimensions of the breakwater are presented in Table 3, according to Fig. 5.

Table 3 Typical prototype dimensions of the breakwater.

Bottom of walls above lake-bed, H_1	1.5 – 2.2 m
Wall height, H_2	2.3 – 3.0 m
Wall thickness, T	0.025 m
Upwind wall's hollow, P	10 - 0 %
Distance between the walls, L_B	6 - 8 m
Beam diameter, D_B	0.3 m

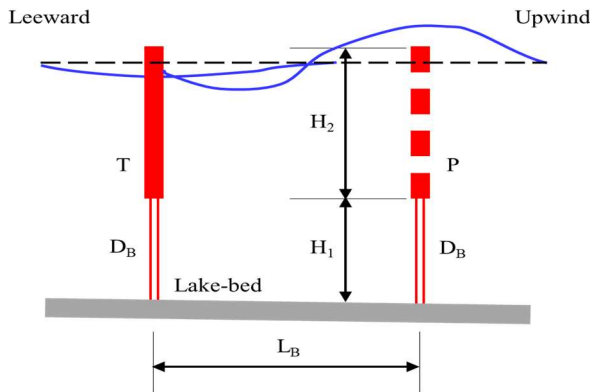


Figure 5: Typical geometric parameters of the breakwater

3. Analysis methods

The velocity measurements were done with a single 2 MHz Met-Flow probe. The sampling path extended over 45 mm. Vertical profiles with horizontal velocity were obtained as the $\cos 30^\circ$ component of the recorded data.

The measured flow velocity and calculated bed shear stress were compared to critical values, for both initial and project states. The reedbed substratum is considered as composed of sand and silt with moderate cohesion. The critical bed shear stress is expressed by Eq. 1.

$$\tau = \rho \left(\frac{U_x \cdot \kappa}{\ln \left(\frac{11 \cdot h}{k_s} \right)} \right)^2 \quad (1)$$

with:

- ρ , density of water,
- U_x , horizontal flow velocity,
- κ , von Kármán's constant (typically: 0.408),
- h , water column above the substratum,
- k_s , roughness height.

4. Preliminary data

Lake Geneva bathymetry was obtained from specific GIS data. The Lake's water level is regulated at its emissary in Geneva by the Seujet hydropower plant. The typical winter water level is 371.60 m.a.s.l.. During spring, snowmelt fills back the lake to the typical maxima of 372.30 m.a.s.l., lasting seven months. The historical extreme maxima corresponds to 372.70 m.a.s.l., attained a second time in Mai 2021.

Wind data were obtained from MétéoSuisse. Due to its 16 km fetch (Fig. 1), the determinant wind at Coligny is the northeast Bise. Duration curves of distinct return periods of the Bise were considered according to [3]. The dimensionless wave variables were determined with the JONSWAP method (Joint North Sea Wave Observation Project) [4], expressed as a function of the determinant dominant wind, the local bathymetry and shoaling conditions, as follows.

5. Modelling results

All results are hence presented with prototype values corresponding to natural i.e. project conditions.

The calibration of the physical model was first carried out. The simulations were done under stationary condition with sinusoidal homogeneous waves. Wave propagation was frontal to the breakwater to attain a maximum mechanical stress on its structure and effort on the reed bed.

Six water levels were applied for all tests, between the 372.70 m.a.s.l. extreme high-level of the lake and the 371.45 m.a.s.l. extreme low level.

The initial state was first simulated, without the breakwater, but the reedbed implemented in the model. For the project state, the experimental series were run by systematically adjusting the breakwater's geometry to achieve an efficient energy dissipation (see [2] and [1]).

The measured velocity range on the model is 0-0.4 m/s, and the velocity resolution is 10 mm/s (see Fig. 7 and 9). According to Table 1, these ranges fit in the UVP measurement range. The uncertainty of the measurement results is below 1 %.

5.1 Initial state

Reedbed behavior and soil erosion analysis at the initial state (without breakwater), were done for 50-year return period. Typical prototype values were: $H = 1.0$ m, wave height, $L = 23.8$ m, wave length, $1/f = 4.05$ s, wave period.

During the flux phase, pointing to the shore, KMnO_4 dye tests showed a slight slowing down of the wave induced flow, due to the vegetation. The Met-Flow probe installed at the upwind edge of the reedbed, revealed a systematic characteristic velocity profile, as shown in Fig. 7 (solid line), with a near parabolic velocity distribution.

In Fig. 7 (dashed line), a typical velocity profile corresponding to the reflux phase is presented. While the main flow tends to backflush, the vegetation induces an eddy flow with a reversed current close to the substratum.

During both flux and reflux, the wave induced current close to the bed seems to slow down.

The typical horizontal component of the measured velocity converted to prototype value varies between $U_x = 1.5$ m/s and 2.0 m/s, oscillating from flux to reflux. Due to these measured values the calculated shear stress (Eq. 1) varies between $\tau = 4.94$ and 8.78 N/m².

Former analysis [5] reported a critical flow velocity comprise between $U_{cr} = 0.5$ to 0.6 m/s for erosion of sand substratum, and $U_{cr} = 0.3$ to 0.4 m/s for mud. Critical stress reported for sand erosion (Eq. 1) is about $\tau_{cr} = 0.3$ to 0.35 N/m², and about $\tau_{cr} = 0.2$ to 0.25 N/m² for mud.

In the light of the foregoing, it is noteworthy that without a breakwater both flow velocity and shear stress exceed the critical values, demonstrating the erosion of the reedbed's substratum. The impoverishment of the soil yields an inevitable destruction of the reedbed, which must be avoided in order to sustain the projected ecological revitalisation measure. A protecting breakwater is therefore needed.

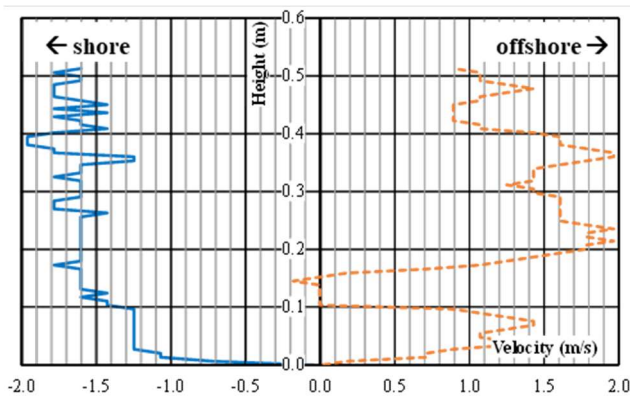


Figure 7. Horizontal U_x Met-Flow UVP velocity profiles (prototype values). Solid line: flow over the reedbed is pointing the shore. Dashed line: backdraft flow pointing mainly offshore, with a reversed flow close to the substratum, revealing the influence of reeds.

5.2 Project state

The wave tank equipped with the breakwater is presented in Fig. 7. The most relevant breakwater layout yields a near 70% wave energy reduction over the reedbed.

Substratum erosion potential is estimated on the basis of recorded velocity profiles. The two characteristic flow shapes shown in Fig.9 reveal a velocity pattern typically weaker than under initial state (Fig. 7). During backwash, flow encounters a reversed current near the bottom (Fig. 9 dashed line), due to the vegetation.

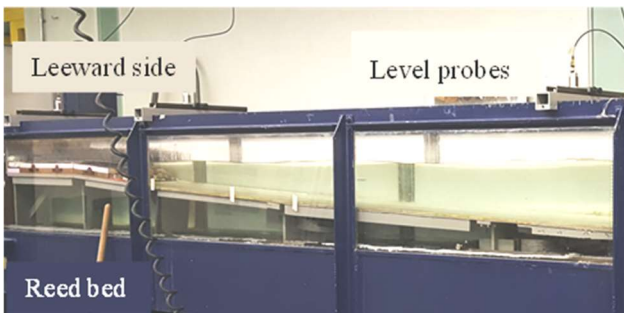


Figure 8. Wave tank during project state simulation. The breakwater yields a significant wave energy dissipation at its leeward stretch.

The typical horizontal component of the measured velocity under 50-year storms, converted to prototype value varies between $U_x = 0.35$ and 0.55 m/s, oscillating from flux to reflux. Due to these measured values the calculated shear stress (Eq. 1) varies between $\tau = 0.27$ and 0.66 N/m². These values are close to or lower than reported critical ones for sand erosion ($U_{cr} = 0.5$ to 0.6 m/s; $\tau_{cr} = 0.3$ to 0.35 N/m²).

Kármán constant of Eq. 1 may vary between 0.35 and 0.42 in flows over mobile sediment beds. With $\kappa = 0.42$, instead of 0.408, the maximum shear stress would not change significantly ($\tau = 0.70$ N/m²). The systematic shading effect of the reed vegetation may also help to protect its proper substratum even under 50-year storms.

The designed breakwater yields an efficient protection of

the reedbed and its substratum against erosion.

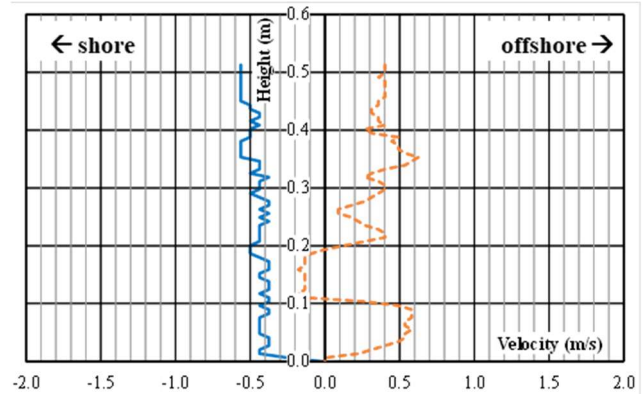


Figure 9. Horizontal U_x Met-Flow UVP velocity profiles (prototype values). Solid line: flow over the reedbed is pointing the shore. Dashed line: backwash flow pointing mainly offshore, with a reversed flow close to the substratum, revealing the influence of reeds.

6. Conclusion

The presented study carried out, on a physical model at the LHA of HEPIA in Geneva, on the protection of a reedbed yielded the following achievements:

- Without a breakwater the reedbed of Cologny should suffer from harms due to wind induced waves.
- Former papers [1] and [2] point out that the innovative double-wall breakwater developed by CERA engineers and tested at the LHA will protect the reed bed, by dissipating the wave energy about 70%.
- The present paper demonstrates, with the help of Met-Flow UVP measurements and calculated shear stress, that the breakwater yields also an efficient protection of the reedbed substratum.

In conclusion, the innovative breakwater can be constructed off shore Cologny, to guarantee a resilient reedbed.

References

- [1] Vecsernyes Z, *et al.*: Physical modelling yields an innovative breakwater structure protecting a reed bed in Lake Geneva from wind wave induced harms, IAHR APD, Sapporo (2020)
- [2] Jaeger, A. Étude sur modèle physique d'un brise-lames lacustre, Bachelor thesis HEPIA HES-SO, Switzerland (2017)
- [3] Bruschin and Falvey: Vagues de vent sur un plan d'eau confiné: considérations générales et application au Léman (Petit-Lac), in Bulletin technique de la Suisse romande, Cahier 14. Tiré de doi.org/10.5169/seals-72567. (1975)
- [4] Hughes, S.A.: Physical models and laboratory techniques in coastal engineering. Advanced Series on Ocean Engineering, Volume 7, World Scientific, Singapore, (1993), 570 pp.
- [5] Kamphuis, J.W.). Introduction to Coastal Engineering and Management. Advanced Series on Ocean Engineering, Volume 30, World Scientific, Singapore, (2010), 502 pp.

Sediment Dynamics by Bistatic Ultrasonic Doppler Under Real Waves

Noemie Fritsch¹, Guillaume Fromant², France Floc'h¹, Stephane Fischer³, Yohan Cobac¹, Charles Poitou¹, Christophe Prunier¹, Stephane Bertin¹, Emmanuel Augereau¹, Marion Jaud¹, Jonathan Tannin¹

¹ Laboratoire Géosciences Océan, Institut Universitaire Européen de la Mer, Rue Dumont d'Urville, Brest, France.

² Laboratoire d'Informatique Signal et Image de la Côte d'Opale, Université du Littoral Côte d'Opale, Calais, France.

³ Ubertone, Schiltigheim, France.

In order to improve sand transport models, the coastal engineering community needs data collected in natural conditions. In particular, sand transport processes in the wave boundary layer still need to be investigated, but the high temporal and spatial variability observed in this area makes it complicated to monitor it properly. In order to address this issue, the first worldwide in situ deployment of UB-Lab 3C, based on Acoustic Concentration and Velocity Profiler technology, took place at Porsmilin beach, in 2022. First data collected with this instrument are processed, and averaged in order to obtain intra-wave velocity, concentration and flux for two categories of waves in the shoaling zone: low and high orbital velocity waves. Sediment concentrations under higher orbital velocity waves are stronger than under lower orbital velocity waves. This preliminary data set is promising, and further analysis should allow to extend existing knowledge on sand concentration and transport under real in situ waves in shallow environments.

Keywords: Acoustic Profiler, ACVP, ADVP, Sediment Dynamics, Concentration, 3C Velocity Vector Profile

1. Introduction

Beaches are among the most dynamic areas on Earth. In order to predict beach morphodynamics, the coastal engineering community needs robust and reliable sand transport models, all the more so since water level rise due to climate change is bound to reshape the shoreline and to impact its dynamics in the years to come. Depending on the wave conditions and their initial state, beaches erode or accrete. While erosion mechanisms have been the focus of numerous publications in the last decade and are therefore quite well quantified in predictive models (van Rijn et al. 2011), mechanisms leading to accretion still remain poorly understood in comparison. Up until now, most data concerning sediment transport processes were collected in laboratory facilities (Ribberink et al. 2008; Nielsen et al. 2002 ; Hughes, 1993). It is known for instance that onshore-directed transport mainly occurs in the wave boundary layer via bed load, under moderate wave conditions (Mieras et al. 2019), but the relative contribution of different transport mechanisms leading to onshore-directed transport still needs to be clarified. Furthermore, understanding suspended sediment load as well as bed load is necessary in order to predict morphological changes of beaches (Aagaard and Jensen, 2013).

Technical difficulties accounting for the lack of in situ sediment transport data are twofold: first, the complex logistic needed to deploy instruments in the field in such energetic environments and second, the lack of appropriate means of colocalized velocity and concentration measurements. Indeed, in order to

investigate boundary layer transport processes, high spatial and temporal resolution is needed for an accurate quantification of these highly variable processes. Likewise, the investigation of turbulence in this very area also requires high temporal resolution. Colocalized measurements of sediment velocity and concentration are necessary to compute transport. In this frame, the Acoustic Concentration and Velocity Profiler (ACVP) technology has been developed and allows obtaining high resolution profiles of velocity and estimations of concentration through an inversion model (O(ms), O(mm)) (Hurther et al. 2011). Since then, the instrument has been turned into a field prototype, the UB-Lab 3C, by Ubertone. This novel instrument, which has been made suitable for the marine environment, has been deployed for the first time in 2022 at Porsmilin Beach, Brittany, France, with the aim to better understand sediment conditions under waves. Targeting the observation of sand transport in the boundary layer, data collected with this instrument seem very promising and should allow improving predictive sand transport models.

First, the deployment site and methods are presented. Then, preliminary results are revealed, based on first observations of velocity, concentration and cross-shore flux in the boundary layer under waves in the shoaling zone.

2. Study sites and methods

2.1 Study area

UB-Lab 3C deployment took place on October 27th, 2022 at Porsmilin beach, Brittany, France. It is a pocket Beach located 15 km West of Brest. It is submitted to

moderate south-west swell. It is a macrotidal sandy beach, with a median sand particle radius $D_{50} = 320$ micrometers (Dehouck, 2009). The long-shore dynamic observed on the beach is negligible compared to cross-shore dynamic.

2.2 UB-Lab 3C deployment method

UB-Lab 3C is part of a whole set of instruments deployed on a dedicated platform, (Fritsch et al. 2022) in order to study hydrodynamics and sediment transport in the water column (see Fig. 1). For instance three acoustic Doppler velocimeters (ADV) and concentration profilers are installed higher in the water column.



Figure 1: Mooring at low tide (top) and UB-Lab 3C (385 mm long with a central emitter and 4 surrounding receivers (bottom)

The mooring was deployed at low tide in the intertidal zone of the beach (1m high). Instruments then recorded hydrodynamic and sediment transport data during one tidal cycle, and the platform was retrieved during the following low tide. That day, the wave height was approximately 0.75 m at the beach and 1.25 m offshore.

2.3 UB-Lab 3C features

The UB-Lab 3C (Fig.1) is an ADVP - Acoustic Doppler Velocity Profiler (Hurther et al. 2011) and was developed by Ubertone. This bistatic velocity profiler works with one narrow beam emitter and four simultaneous wide beam receivers, each is 10 cm apart from the receiver. All transducers are wide band and centered at 1MHz. Profiles can be recorded at a sampling frequency up to 64 Hz and spatial resolution down to 2.2mm.

In this study, it simultaneously recorded the 3C velocity and backscattered echo amplitude profiles, up to 15 cm

above ground. The instrument was set with a PRF of 1650Hz, each profile was calculated over 32 pulses. We applied acoustic inversion techniques on backscattered intensities (Thorne and Hanes, 2002), to estimate sediment mass concentration in the boundary layer. Since concentration and velocity are measured in the same volume, they can be regarded as colocalized measurements. Quasi instantaneous cross-shore fluxes were then computed by multiplying colocalized concentration and velocity profiles. The sand bed is defined as corresponding to the location of the maximum backscattered intensity.

2.4 Studied data

The water elevation above the mooring over high-tide is obtained through pressure data (collected at 5Hz rate). The water height reached 4.5m above the mooring during the deployment. The time series studied below were recorded in the shoaling zone. Those specific time series were chosen because separation between waves was possible. The first studied time series starts at 14h48min53s (UTC) and stops at 14h51min10s. The second studied time series starts at 14h54min5s and stops at 14h56min11s. The ‘free stream’ velocity time series on Fig. 2 corresponds to the cross-shore velocity average of the cells 30 to 35 (U_{rms}) in the profile recorded by the UB-Lab 3C (50 Hz) (among the 100 cells in a profile).

2.5 Data processing

Since measurements are quasi instantaneous, they are subject to noise problems. In order to remain consistent with previous studies realized under waves (Fromant et al 2019, Hurther and Thorne 2011), data were averaged on 15 waves which were cut with a zero-crossing method. Then, indices retrieved from this velocity cutting were applied on concentration and velocity profiles recorded by the UB-Lab 3C. This method is explained on Fig. 2. This way, concentration and velocity profiles under each studied wave were obtained. Then, those waves were divided into two groups based on the value of their orbital velocity.

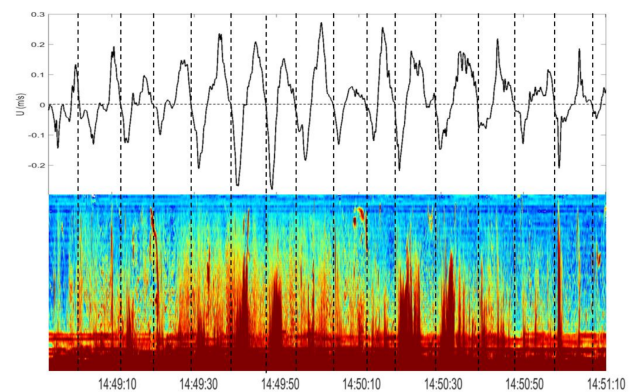


Figure 2: First line: free stream velocity of the first time series, and second line: corresponding concentration under the waves. The concentration profiles are cut following the indices retrieved after the wave cutting thanks to a zero-crossing method (vertical dotted thick black lines, arbitrary color range).

2.6 Wave characteristics

The first group of waves corresponds to the ‘low orbital velocity’ waves (category 1), and the second group the ‘high orbital velocity’ waves (category 2). The characteristics of the mean free stream of each category are displayed in Table 1. T is the wave period in seconds, A_{sy} is the wave asymmetry computed as:

$$A_{sy} = \frac{a_{max}}{a_{max} - a_{min}} \quad (1)$$

with a_{max} the maximum acceleration value during the studied wave cycle, and a_{min} , the minimum acceleration value. S_k is the wave skewness computed as:

$$S_k = \frac{u_{max}}{u_{max} - u_{min}} \quad (2)$$

with u_{max} the maximum velocity value during the studied wave cycle and u_{min} the minimum velocity value. A_{orb} is the orbital velocity, computed following Ribberink et al. (2008):

$$A_{orb} = \frac{\sqrt{2}U_{rms}T}{2\pi} \quad (3)$$

with U_{rms} the root mean square of the wave velocity .

Table 1: Wave parameters for both categories (see eq. 1, 2 & 3).

Parameter	Category 1		Category 2	
	Average	Standard deviation	Average	Standard deviation
T (s)	9.2	1.4	9.0	1.4
$A_{sy}(1)$	0.52	0.11	0.51	0.07
S_k (1)	0.53	0.12	0.53	0.13
A_{orb} (m)	0.12	0.05	0.27	0.07

For each category of waves, velocity, concentration and flux data are studied. Those quantities are represented on Figures 3, 4 and 5 for the category 1 (waves with low orbital velocity) and on Figure 6 for the category 2 (waves with high orbital velocity).

3. Results

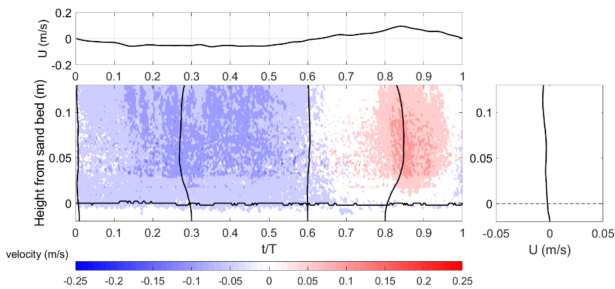


Figure 3: Free stream wave velocity (first line), intra wave mean velocity color plot (middle graph) and mean wave-averaged velocity profile (right panel) for the low orbital velocity waves.

velocity profile (right panel) for the low orbital velocity waves.

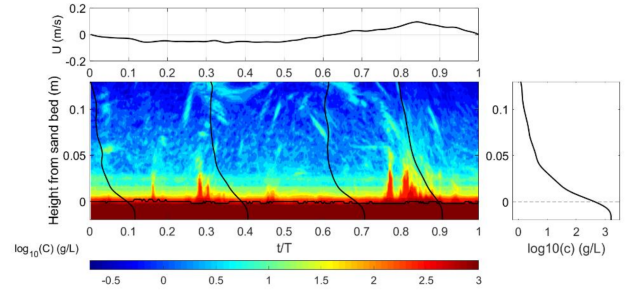


Figure 4: Free stream wave velocity (first line), intra wave mean concentration color plot (middle graph, in logarithmic scale) and mean wave-averaged concentration profile (right panel) for the low orbital velocity waves.

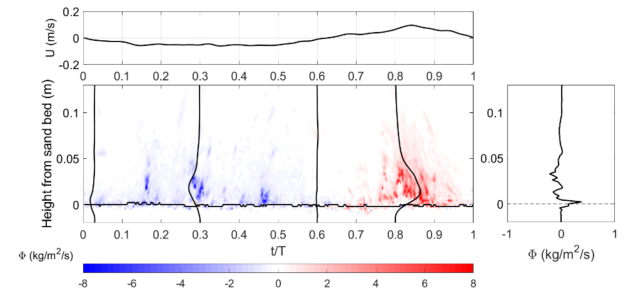


Figure 5: Free stream wave velocity (first line), intra wave mean flux color plot (middle graph) and mean wave-averaged flux profile (right panel) for the low orbital velocity waves.

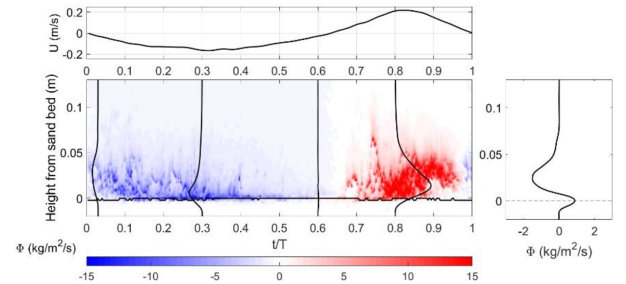


Figure 6: Free stream wave velocity (first line), intra wave mean velocity color plot (middle graph) and mean wave-averaged velocity profile (right panel) for the high orbital velocity waves.

3.1 Structure of the figures

On each of the above-displayed figures (Fig. 3 to 6), the free stream wave velocity cycle is displayed in the first line, then the color plot represents the intrawave velocity (Fig. 3), concentration (Fig.4) and cross-shore flux (Fig. 5 and 6). The vertical profiles on the color plots correspond to the phase-averaged profiles at specific wave events inside a wave cycle: the crest to trough flow reversal, the maximum offshore velocity, the trough to crest flow reversal and the maximum onshore velocity events. The thick black horizontal line corresponds to the bed, detected as explained earlier. Finally, the panel on the right corresponds to the wave-averaged profile of velocity, concentration or cross-shore flux.

3.2 Velocity data

In terms of velocity, it can be observed that in the ‘high orbital velocity’ case (not plotted), the intrawave velocity values are higher than in the ‘low orbital velocity’ case (Fig. 3).

3.3 Concentration data

The intrawave concentration dynamics under the category 2 mean wave (Fig. 4) are more important than under the category 1 mean wave (not plotted). Notably, there is a high concentration patch at $t/T = 0.8-1$ for the high orbital velocity waves, after the trough to crest flow reversal and during the onshore half cycle of the wave. In this case, since sediment did not have the time to resettle before the end of the onshore half cycle, phase lagging effects might be observed (Ribberink et al. 2008, O’Donoghue and Wright 2004). Sediment mobilized during the onshore half cycle might be advected offshore during the offshore half wave cycle. This phenomenon does not seem to be observed for the low orbital velocity case.

3.4 Flux data

The measured intrawave cross shore flux values are higher for the category 2 mean wave (Fig. 5) than for the category 1 mean wave (Fig. 6). This is consistent with the higher concentration values observed in category 2 than in category 1 (Fig. 4). On the mean flux profile (right panel of Fig. 6), it is clear that a strong wave-averaged onshore flux can be observed close to the sand bed, whereas an offshore-directed flux can be observed higher in the water column. This result is consistent with previous studies (Mieras et al, 2019; Brenner et al., 2018).

4. Discussion and Conclusion

The UB-Lab 3C is the first commercial version of a field ADVP and was developed by Ubertone. Its first deployments allowed obtaining colocalized high resolution measurements of velocity and concentration profiles in natural conditions. First data collected at Porsmilin beach, Brittany, France, show how promising this technology is in terms of boundary layer transport observations. For a better understanding of sand transport processes, UB-Lab 3C data should be processed in the light of the data recorded higher in the water column from the ADVs and the concentration profilers. Data set collected with the mooring (Fig. 1) should offer a complete overview of cross-shore sediment processes on sandy beaches.

Several deployments were done in the meantime, in particular in the winter 2022-2023 at Porsmilin Beach in Brittany, France. Those specific deployments aim at targeting the observation of seasonal accretive conditions that can be observed after stormy events on sandy beaches. It is hoped that data collected with this UB-Lab 3C, associated with data from other instruments deployed in the mooring will deepen knowledge on cross-shore sand transport in natural conditions, particularly under

accretive conditions.

This field version of the UB-Lab 3C will soon be available also in lab version, with external transducers and splashproof case.

Acknowledgements

This work is part of ANR project WEST (ANR-20-CE01-0009), it was also supported by Geo-Ocean lab (UMR6538), ISblue project (ANR-17-EURE- 0015) and co-funded by a grant from the French government under the program "Investissements d’Avenir". Part of the equipment used in this experiment was funded by the French Government, the European Fund for Economic and Regional Development, the Regional Council of Brittany, and authorities of Finistère as part of the CPER project O3DO (2016-2020). Special thanks to ODYSC team for support on field experiments, P2I, Albert Lucas sailors and IUEM divers.

References

- Aagaard, T., & Jensen, S. G. (2013). Sediment concentration and vertical mixing under breaking waves. *Marine Geology*, 336, 146–159.
- Dehouck, A. (2009) Morphodynamique des plages sableuses de la mer d’Iroise.
- Fromant, G., Hurther, D., Zanden, J., A, D. A., Cáceres, I., O’Donoghue, T., & Ribberink, J. S. (2019). Wave Boundary Layer Hydrodynamics and Sheet Flow Properties Under Large-Scale Plunging-Type Breaking Waves. *Journal of Geophysical Research: Oceans*, 124(1), 75–98.
- Hurther, D., & Thorne, P. D. (2011). Suspension and near-bed load sediment transport processes above a migrating, sand-rippled bed under shoaling waves. *Journal of Geophysical Research: Oceans*, 116(7).
- Hurther, D., Thorne, P. D., Bricault, M., Lemmin, U., & Barnoud, J. M. (2011). A multi-frequency Acoustic Concentration and Velocity Profiler (ACVP) for boundary layer measurements of fine-scale flow and sediment transport processes. *Coastal Engineering*, 58(7), 594–605.
- Mieras, R. S., Puleo, J. A., Anderson, D., Hsu, T. J., Cox, D. T., & Calantoni, J. (2019). Relative Contributions of Bed Load and Suspended Load to Sediment Transport Under Skewed-Asymmetric Waves on a Sandbar Crest. *Journal of Geophysical Research: Oceans*, 124(2), 1294–1321.
- Nielsen, P., & Callaghan, D. P. (2002). Shear stress and sediment transport calculations for sheet flow under waves.
- O’Donoghue, T., & Wright, S. (2004). Concentrations in oscillatory sheet flow for well sorted and graded sands. *Coastal Engineering*, 50(3), 117–138.
- Ribberink, J. S., van der Werf, J. J., O’Donoghue, T., & Hassan, W. N. M. (2008). Sand motion induced by oscillatory flows: Sheet flow and vortex ripples. *Journal of Turbulence*, 9, 1–32.
- Thorne, P. D., & Hanes, D. M. (2002). A review of acoustic measurement of small-scale sediment processes. In *Continental Shelf Research* (Vol. 22).
- Van Rijn, L. C., Tonnon, P. K., & Walstra, D. J. R. (2011). Numerical modelling of erosion and accretion of plane sloping beaches at different scales. *Coastal Engineering*, 58(7), 637–655.

Rock-Flow Cell Parameters Evaluation Using Ultrasound Doppler Velocimetry

Stakowian, Andre, L.¹, Dextre, Gino N. D.⁵, Botton, Luís F.¹, Dos Santos, Eduardo, N.¹, Coutinho, Fabio, R.², Ofuchi, César, Y.¹, Da Silva, M, J.³, De Cesare, G.⁴, Morales, R, E, M.⁵, Mariette, O.⁶

¹ Graduate School of Electrical Engineering and Computer Science (CPGEI), Federal University of Technology - Paraná (UTFPR), Av. 7 de Setembro 3165, Curitiba, 80230-901, Parana, Brazil.

² Dep. of Electronics Engineering, Federal Univ. of Technology - Paraná (UTFPR), R. Cristo Rei 19, Vila Becker, Toledo, Parana, 85902-490, Brazil.

³ Institute of Measurement Technology, Johannes Kepler University Linz, Altenberger Str. 69, 4040, Linz, Austria.

⁴ Platform of Hydraulic Constructions (PL-LCH), École Polytechnique Fédérale de Lausanne (EPFL), CH1015 Lausanne, Switzerland.

⁵ Mechanical & Materials Engineering Postgraduate Program (PPGEM), Federal University of Technology - Paraná (UTFPR), Av. 7 de Setembro 3165, 80230-901, Curitiba, Parana, Brazil.

⁶ Met-Flow S.A, Chemin Auguste-Pidou 8, 1007 Lausanne, Switzerland.

This work presents a study of two-phase flow generated inside a rock-flow cell setup. It is characterized by a pipe section filled with fluid (oil in our studies) that is put into oscillation around its mass centre by an electric motor. This type of apparatus has been used by some research groups worldwide to mimic the flowing conditions of complex pipe multiphase flows but with the advantage of being compact in size. In this work, a rock flow cell was used to characterize stratified-wavy and slug flow regimes to investigate the phenomenological dynamics and behaviour around the liquid interface. The experimental procedure cases covered two total cell liquid loadings (30% and 75%), and the setup configuration was kept the same in terms of angular frequency oscillation (100 rpm) and oscillation angle amplitude (19°). Ultrasound Doppler Velocimetry (UDV) was used to monitor and assess the flow field velocity behaviour and distribution inside a rocking pipe, obtained through the EAM (Extended Auto-Correlation Method) velocity estimator algorithm. From the resulting velocity profile, we estimated the shear rate parameter. Furthermore, we could identify the air-oil phase interface position using the echo amplitude information. The UDV technique applied to rock-flow cell has a great potential to generate detailed flow information, which in turn can be used, for example, to validate Computational Fluid Dynamics (CFD) numerical simulations.

Keywords: Rock-Flow Cell, Doppler Velocimetry, Multi-Phase Flow, Velocity Profile.

1. Introduction

As the interest in a better understanding of flows' behaviour and characterization has grown through the last decades, various methods and technologies have emerged to shed more light on the fluid dynamics research field. Amongst some of the approaches to working with the fluid dynamics field, we can mention optical methods such as Particle Image Velocimetry (PIV), which require both the fluid and its casing to be transparent and has high implementation and computational costs. Electrical impedance and conductance probes, which are invasive options prone to lead to flow disturbances. On the other hand, ultrasound-based methods, such as Ultrasound Doppler Velocimetry (UDV), have the desirable advantages of being non-invasive, non-intrusive, capable of working with opaque fluids, and ease of installation and operation [1]. The UDV method also encounters applications in various industry and research fields such as nuclear plants, food engineering, chemical plants, oil and gas exploitation and transportation [2], [3].

The ideal scenario for studying the flow behaviour would be having access to real plants and installations, which is only sometimes possible and would be costly. Thus, alternatives have to be found to promote the studies. Such

options are flow loops, which can be built in different configurations, trying to resemble the real plants and installations, enabling the assessment of characteristics of the phenomena in more detail. Another option is the rock-flow cells, which have the advantage of being compact in size and able to produce complex multiphase flows, using fewer resources as, for example, the reduced volume of the liquid phase. The main applications of rock-flow cells are in the flow assurance field, where hydrate formation and deposition are studied [4], [5], and also the assessment of hydrate mitigation methods [6], [7].

In this work, we first present the stratified-wavy flow assessment, a more straightforward flow pattern through which we could understand the experimental process and signal processing. Then, the slug flow pattern is addressed with a higher level of liquid loading. This type of flow is commonly found in multiphase flows, receiving particular attention due to their presence in various applications, particularly in the oil and gas industry. This specific flow pattern poses a significant challenge in fluid transportation due to problems associated with pipeline corrosion caused by the erosion of anticorrosive materials. Additionally, the mixing region of slugs enhances hydrate formation, one of the significant concerns in flow assurance. In such scenarios, the presence of bubbles originates from the

detachment of the gas phase at the rear of the long bubble. This detachment is caused by an imbalance of forces, primarily resulting from excessive shear near the fluid interface. This paper proposes the use of a new approach for estimating the shear rate using the US method in the rock-flow cell configuration.

The shear rate parameter may suffer from multidimensional velocity vectors, however, in this work we are primarily interested in the shear force in the vertical ultrasound beam plane. In this scenario, the shear rate is estimated from the field velocity (in the flow direction), calculated through the following relation: $\varepsilon = \partial u / \partial y$; where ε is the shear rate (s^{-1}) to be analyzed, u (m/s) the particle velocity in x direction (flow direction), y (m) position of pipe section.

2. Experimental Set-Up and Methodology

The experimental apparatus developed for the experiments and results presented in this work is named Rock-Flow Cell. It consists of a 1200 mm long acrylic pipe with a 50 mm inner diameter, mounted on an aluminum frame with an oscillating pivot (Figure 1). One engine performed the RFC oscillating movement through a connecting rod and crank system. An accelerometer located at one edge of the pipe measured the oscillation frequency and oscillation amplitude range, which were kept at 100 rpm and 19° , respectively, throughout the whole experimental set. Images were captured through a high-definition camera (Logitech c920) and processed in the MatLab® 2019b release.

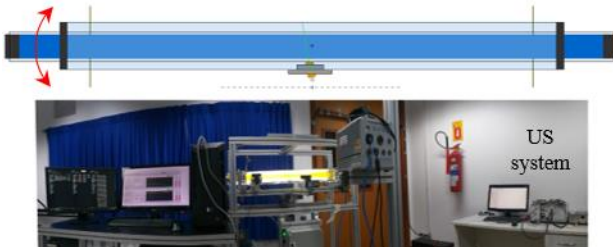


Figure 1: Rock-Flow Cell schematic description.

The test fluid is a mineral oil, which density is 843.32 (kg/m^3), its viscosity is 0.0687 (kg/ms), and its superficial tension is 0.031 (N/m). We worked with two distinct total cell liquid loadings (30% and 75%, concerning the total cell volume) as our experimental cases; the amount of oil, in volume, corresponding to each liquid loading, was weighted, mixed with yellow dye to identify the air-oil interface better, and poured inside the pipe. An acrylic box filled with water was disposed around the pipe to reduce the light refraction effect and, thus, the distortion of the image captured by the camera. A frequency inverter was applied to regulate the oscillation speed (100 rpm).

The instrumentation of the rock-flow cell was made through a 4 MHz ultrasonic transducer, positioned beneath the pipe, aligned with its axis, and at 10° to the pipe's cross-sectional plane. The data set was acquired using the National Instruments-based PXIe-1078 chassis with a

PXIe-7966R FPGA module. The entire signal post-processing has been done offline in the MatLab® 2019b release. Polyethylene seeding particles of 937 (kg/m^3), with a mean diameter of around 250 (μm), were added and mixed with the oil phase. These particles played the role of tracers for the Ultrasonic Doppler technique.

The experimental approach, briefly described, was as follows: initially, we positioned the pipe section perfectly horizontally, with the aid of an electronic angle meter; then we started the data acquisition system; after about 2.5 seconds, we started the motion system. We intentionally did this process to capture a portion of the flat, steady state, part of the liquid phase, which enabled us to confirm the liquid loading through the liquid height obtained from the ultrasound backscattered signal. Finally, the offline post-processing part encompasses the air-oil phase interface identification through the amplitude threshold technique from the raw, backscattered signal [8] and the velocity map obtained through the Extended Auto-Correlation Method (EAM) [9].

3. Results and Discussions

In this section, we provide a qualitative and quantitative discussion about the outcomes of our experiments. Figure 2 displays the phase interface estimated and the velocity map for the 30% of liquid loading. Given this level of cell filling, we have the stratified-wavy flow pattern developed, characterized by the undulatory behaviour of the liquid phase that does not touch the upper part of the pipe. In the first nearly 2.5 seconds the cell was kept in its steady state, and then the system was put into oscillation. In this figure, we can also see two well-defined, alternating equivalent behaviour regions, governed by the direction of oscillation of the rock-flow cell. R1 and R2 represent the clock-wise sense of motion of the rock-flow cell, where the flow moves away from the transducer, and R3 and R4 being the opposite.

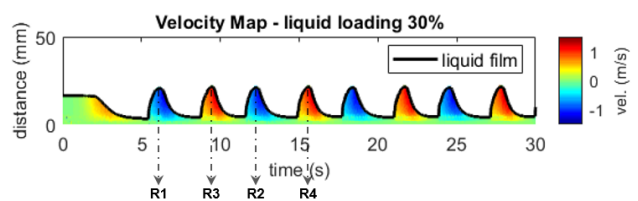


Figure 2: Stratified-wavy flow pattern obtained with 30% of total liquid loading.

Additionally, from the velocity map (Figure 2) we can observe that the magnitude of velocity field distribution is higher on the back of the wave structure. In a similar manner, we compared the mean velocity profiles for the corresponding lines R3 and R4, as shown in Figure 4.

Figure 3 depicts the instantaneous velocity profiles along lines R1 and R2, exhibiting an equivalent behavior between them, and good agreement in terms of shape and magnitude, also reproducing the no-slip condition at the wall surface. We noticed that an oscillation frequency of 100 rpm results in a max velocity of about 0.75 (m/s) in both directions.

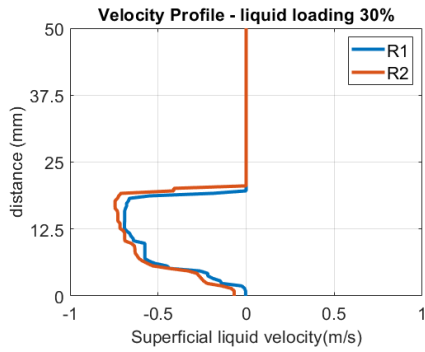


Figure 3: Comparison of velocity profiles for the equivalent behaviour regions R1 and R2.

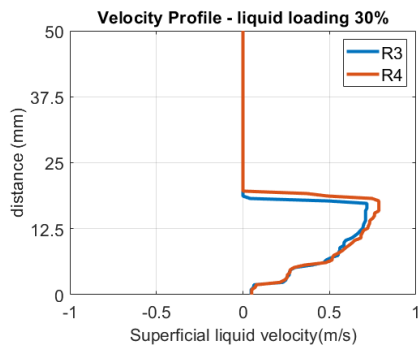


Figure 4: Comparison of velocity profiles for the equivalent behaviour regions R3 and R4.

From the velocity profiles (Figure 3 and Figure 4), we also calculated the shear rate parameter, shown in the Figure 5 and Figure 6.

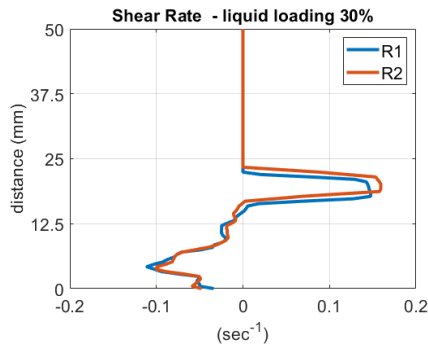


Figure 5: Comparison of the shear rate parameter for the equivalent behaviour regions R1 and R2.

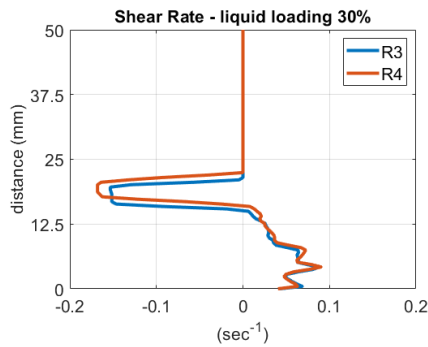


Figure 6: Comparison of the shear rate parameter for the equivalent behaviour regions R3 and R4.

As expected, both the oil-air interface and the pipe wall experience the effects of liquid shear stress. This stress is slightly more pronounced at the air-oil phase interface due to the counter-flow pattern, wherein the liquid flows in the opposite direction to the gas. In this configuration, the region near the interface of the fluid layers undergoes a relative movement.

Figure 7 illustrates the velocity map for the liquid loading of 75%. At this level of cell filling, we have the slug flow pattern developed, characterized by alternating gas bubbles and slug body structures. As we could expect, the slug flow is a more complex flow pattern compared to the stratified-wavy, resulting in a diversified range of outcomes.

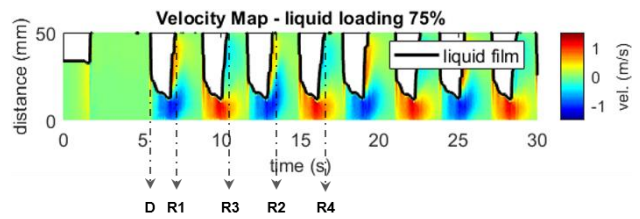


Figure 7: Slug flow pattern obtained with 75% of total liquid loading.

In the flow map (Figure 7), one can notice that we have two distinct field velocity distributions at each slug unit that repeat themselves throughout the equivalent behaviour regions. In Figure 7, the region labeled as 'D' indicates that the leading edge of the slug bubbles, often referred to as the bubble nose, carries a certain amount of oil mass with it due to viscous effects, and this phenomenon occurs in both directions.

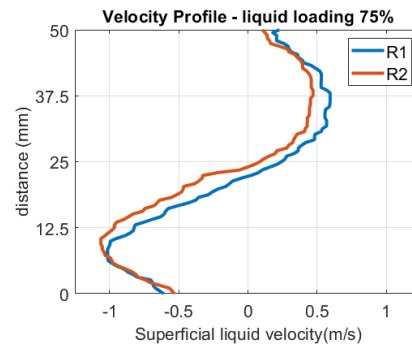


Figure 8: Comparison of velocity profiles for the equivalent behaviour regions R1 and R2.

Figure 8 and Figure 9 highlight the velocity profile lines plotted at the rear part of the slug bubble, where it is possible to see the changes in velocity direction between liquid film and slug body. This is due to the high turbulence and mixing factor at the bubble tail.

As the proposal is to estimate the shear rate at the end of the bubble, the pair of positions R1-R2 and R3-R4 were selected. The behaviour in both cases follows the aforementioned results, demonstrating acceptable repeatability.

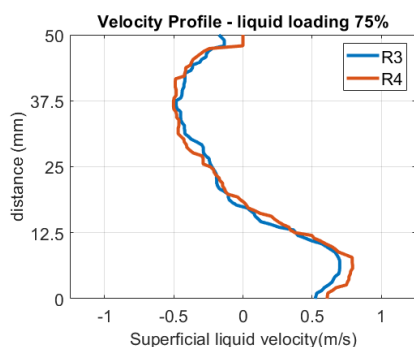


Figure 9: Comparison of velocity profiles for the equivalent behaviour regions R3 and R4.

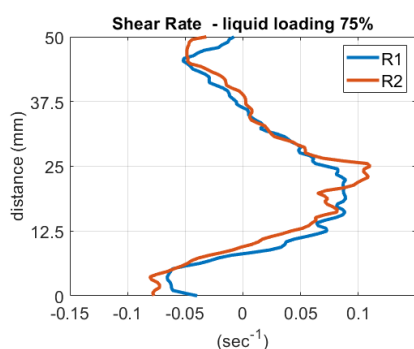


Figure 10: Comparison of the shear rate parameter for the equivalent behaviour regions R1 and R2.

It is interesting to note that the shear rate, at the positions selected, reaches a peak in magnitude at the inflection point portion of the flow, where the velocity fields change direction, which occurs approximately at 25 mm for regions R1 and R2 (Figure 10), and at 12.5 mm for regions R3 and R4 (Figure 11), respectively.

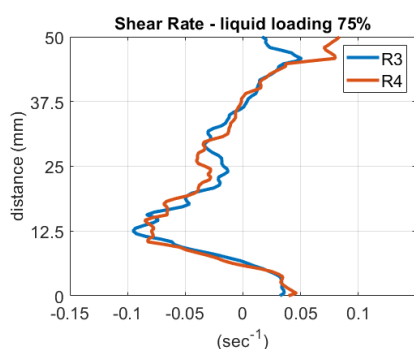


Figure 11: Comparison of the shear rate parameter for the equivalent behaviour regions R3 and R4.

4. Summary

In this work, we presented a novel and insightful application for the Ultrasonic Doppler Velocimetry technique. We could instrument a Rock-Flow Cell, an innovative laboratory-scaled flow generator, and analyze two different flow patterns.

From the results, we found that the UDV technique was able to successfully characterize the stratified-wavy and slug flow patterns in terms of phase interface identification and velocity field distribution. Through further analysis of

the velocity profiles and velocity maps we could qualitatively and quantitatively describe the velocity behavior in different structures for both flow patterns. Thus, some overall and conclude remarks can be drawn:

- For the stratified-wave flow, the velocity profiles are similar in shape and magnitude, in both directions, as expected, and the velocity field distribution magnitude is higher at the rear part of the wave structure, which we believe is due to the increasing flow momentum. The shear rate was found to be slightly greater at the phase interface.
- With the slug flow pattern the observations were that we have two well defined velocity fields on each slug structure. One is at the liquid film portion, and the other is at the slug bubble tail, which is also a highly turbulent and mixing region, and the velocity fields develop in opposite directions. This behaviour is also highlighted and confirmed with the velocity profiles. The highest level of shear rate occurs at the intersection of the two velocity regions of the slug unit

Acknowledgements

The authors would like to acknowledge the support from the following agencies: ANP, FINEP and MCT, through the Human Resources Program of ANP for the oil and gas sector. Also, to PETROBRAS for the rock-flow cell project funding and CNPq.

References

- [1] Y. Takeda, Ultrasonic Doppler Velocity Profiler for Fluid Flow, vol. 101. 2012.
- [2] C. Tan, *et al.*, "Ultrasonic Doppler Technique for Application to Multiphase Flows: A Review," *Int. J. Multiph. Flow*, vol. 144, no. August, p. 103811, 2021, doi: 10.1016/j.ijmultiphaseflow.2021.103811.
- [3] C. Y. Ofuchi, *et al.*, "Evaluation of an extended autocorrelation phase estimator for ultrasonic velocity profiles using nondestructive testing systems," *Sensors (Switzerland)*, vol. 16, no. 8, 2016, doi: 10.3390/s16081250.
- [4] X. Liu, *et al.*, "Experimental investigation on the process of hydrate deposition using a rock-flow cell," *Fuel*, vol. 305, no. August, p. 121607, 2021, doi: 10.1016/j.fuel.2021.121607.
- [5] E. O. Straume, *et al.*, "Experimental study of the formation and deposition of gas hydrates in non-emulsifying oil and condensate systems," *Chem. Eng. Sci.*, vol. 155, pp. 111–126, 2016, doi: 10.1016/j.ces.2016.07.046.
- [6] Y. Liu, *et al.*, "Experimental study on the gas hydrates blockage and evaluation of kinetic inhibitors using a fully visual rocking cell," *J. Nat. Gas Sci. Eng.*, vol. 96, no. October, p. 104331, 2021, doi: 10.1016/j.jngse.2021.104331.
- [7] C. Yu, *et al.*, "Screening Hydrate Antiagglomerants for an Oil-Gas-Water System from Various Commercial Chemicals Using Rocking Cells," *Energy and Fuels*, vol. 36, no. 18, pp. 10685–10701, 2022, doi: 10.1021/acs.energyfuels.2c01285.
- [8] Y. Murai, *et al.*, "Ultrasonic detection of moving interfaces in gas – liquid two-phase flow," *Flow Meas. Instrum.*, vol. 21, no. 3, pp. 356–366, 2010, doi: 10.1016/j.flowmeasinst.2010.03.007.
- [9] C. Y. Ofuchi, *et al.*, "Extended Autocorrelation Velocity Estimator Applied to Fluid Engineering," in *ISUD*, 2014, pp. 109–112.

Ultrasonic sediment flux profiling with ACVP Technology: application to sediment-laden Boundary Layer flows

David Hurther¹, and Giovanni De Cesare²

¹ Lab. of Geophysical and Industrial Flows (LEGI), University Grenoble Alpes, CNRS, Grenoble-INP, 1009 rue de la Piscine, 38041 Grenoble

² Ecole Polytechnique Fédérale de Lausanne (EPFL), Platform of Hydraulic Constructions (PL-LCH), Station 18, CH-1015 Lausanne, Switzerland

Sediment transport in geophysical boundary layer flows has relevance to a broad spectrum of sciences ranging from the physical and chemical, to the biological, ecological and geological. Advances in sediment transport modelling and prediction strongly suffer from lack of space and time-resolved sediment flux measurements due to sediment induced flow opacity hindering the utilization of standard optical flow measurement tools known as LDV, LDA, PIV or PTV technologies. This lack of high-resolution measurements in sediment transport flows strongly limits the identification and quantification of the key boundary layer interaction processes between the (generally highly turbulent) fluid phase, the entrained sediment phase and the underlying flow bed, commonly defined as the dynamic sediment transport process triad [1]. The first part of this study describes the basic measurements principles and methods of (a) ultrasound 1D-2C/3C Doppler velocity profiling, (b) ultrasound spectrometry for sediment concentration profiling. The combination of these two methods into the multi-frequency measurement system as the Acoustic Concentration & Velocity Profiler (ACVP) technology, provides time-resolved profiles of multi-component sediment fluxes across both the suspension and bedload layers at rates resolving small turbulent flow scales. Its application to mean and time-resolved flow quantity measurements is shown in sediment-laden open-channel flow experiments carried out in the LEGI tilting flume facility. Measurement uncertainty in net sediment transport rate is quantified over a wide range of open-channel flow conditions for two sediment sizes.

Keywords: Ultrasound Doppler, Ultrasound spectrometry, Sediment transport, Sediment flux profiling, ACVP

1. Introduction

Reliable predictions of sediment transport flow rate defined as the flow cross-section averaged product of sediment velocity and concentration, remains nowadays a scientific complex and challenging modelling task, particularly for flows in climatic energetic conditions such as during river floods. Concerning the flow velocity modelling, there is still debate on the universality of the value of the von Karman constant κ . [2] argued that the universal value ($\kappa = 0.41$) provides good results, if the wake coefficient due to free-surface flow effects is properly evaluated. However, its reduction in sediment-laden flows has been reported in early studies [3] and more recently based on experimental [4, 5] and numerical evidence [6]. Another challenge concerns the modelling and prediction of sediment concentration profile. Although the Rouse profile for the suspended sediments is a physical process based model, it is often subject to parameter tuning such as for the turbulent Schmidt number value as the ratio between sediment and momentum diffusivities [2].

With the aim of addressing these questions, this study describes a new dataset of sediment transport experiments with two sizes of inertial sediments using the Acoustic Concentration & Velocity Profiling (ACVP) technology as the main flow measurement tool. How sediment flux profiles and net sediment transport rates are measured with this ultrasonic measurement tool is reviewed [7, 8, 9, 16]. Measurement performance is first shown in a mobile bed

open-channel flow experiment carrying sediments in the sheet flow regime [4, 5]. Mean and time-resolved profile measurements are presented and discussed revealing the ACVP's potential for in-depth studies of turbulent particle transport processes in energetic boundary layer flows. Second, the accuracy in sediment transport rate measurement is evaluated over a wide range of sediment-laden flow conditions. For this purpose, new experiments and the one of [10] are used covering three hydraulic conditions (low, medium and high bed friction velocity) with two sediment sizes (3mm and 1mm). Conclusions on the potential of ultrasound flow measurements in sediment-laden boundary layer flows are given.

2. Ultrasonic sediment flux profiling

Sediment flux measurement consists in the simultaneous time-resolved profiling along the streamwise normal flow axis (usually defined as the vertical z-axis direction) of co-located particle velocity and sediment mass (or volume) concentration at a spatio-temporal rate resolving the turbulent flow scales. Standard optical (image and Laser) velocimetry tools known as PIV, PTV, LDA, LDV are not adapted to energetic sediment-laden water flows because of the particle-induced flow opacity. Ultrasonic flow measurements transmitting short acoustic pulses in the MHz frequency range are much better suited to dense sediment-laden flows as long as particle scattering induced attenuation of the pressure signal over the pulse travel-path remains smaller than the magnitude of the flow entering

pressure signal.

Co-located profiling of both particle velocity and concentration is still limited worldwide, to very few acoustic measurement systems implementing two technologies in the same instrument: (i) the Acoustic Doppler Velocity Profiler (ADVP) technology, for the pulse-coherent Doppler velocity profile measurement. (ii) The Acoustic Backscattering System (ABS) technology for sediment size and concentration profiling which applies ultrasonic particle scattering spectrometry [1, 11].

Table 1. Hydraulic parameters

d_p (mm)	w_s (cm/s)	u_* (m/s)	θ (-)	S (-)	Q (m ³ /s)	S_0 (-)	U (m/s)	H_c (m)	Re (-)	Fr (-)	Re* (-)	q_b (m ² /s)	C	Experiment type
3	5.59	0.05	0.4	1.1	0.031	0.005	0.53	0.17	0.9×10^5	0.19	375	7×10^{-4}	7×10^{-3}	1 mobile bed run, at full-capacity
3	5.59	0.043	0.33	1.3	0.032	0.0023	0.60	0.15	1.9×10^5	0.49	323	0.0	0.0	8 CW clear-water runs
												6×10^{-5}	5×10^{-4}	3 LOW concentration runs
												2×10^{-4}	2×10^{-3}	3 MED concentration runs
												3×10^{-4}	3×10^{-3}	3 SAT full-capacity runs
3	5.59	0.056	0.56	1.0	0.041	0.0040	0.79	0.15	2.5×10^5	0.65	421	0.0	0.0	8 CW clear-water runs
												7×10^{-5}	6×10^{-4}	3 LOW concentration runs
												2×10^{-4}	2×10^{-3}	3 MED concentration runs
												6×10^{-4}	5×10^{-3}	3 SAT full-capacity runs
3	5.59	0.068	0.81	0.8	0.049	0.0061	0.96	0.15	3.0×10^5	0.80	509	0.0	0.0	8 CW clear-water runs
												9×10^{-5}	6×10^{-4}	3 LOW concentration runs
												3×10^{-4}	2×10^{-3}	3 MED concentration runs
												9×10^{-4}	7×10^{-3}	3 SAT full-capacity runs
1	1.89	0.030	0.48	0.62	0.0186	0.0007	0.37	0.14	1.2×10^5	0.32	105	0.0	0.0	3 CW clear-water runs
												3×10^{-5}	6×10^{-4}	3 LOW concentration runs
												6×10^{-5}	1×10^{-3}	3 MED concentration runs
												1×10^{-4}	2×10^{-3}	3 SAT full-capacity runs
1	1.89	0.035	0.64	0.54	0.026	0.0016	0.54	0.14	1.7×10^5	0.47	121	0.0	0.0	5 CW clear-water runs
												7×10^{-5}	6×10^{-4}	3 LOW concentration runs
												2×10^{-4}	2×10^{-3}	3 MED concentration runs
												6×10^{-4}	5×10^{-3}	3 SAT full-capacity runs
1	1.89	0.043	0.96	0.44	0.032	0.0023	0.63	0.15	2.0×10^5	0.53	149	0.0	0.0	8 CW clear-water runs
												9×10^{-5}	6×10^{-4}	3 LOW concentration runs
												3×10^{-4}	2×10^{-3}	3 MED concentration runs
												9×10^{-4}	7×10^{-3}	3 SAT full-capacity runs

d_p : sediment median diameter; w_s : still water particle settling velocity; θ : Shields number; S: suspension number; S_0 : Slope of the channel; U: bulk mean velocity; H_c : water depth; ν : kinematic viscosity of water; u_* : friction velocity and g is the gravitational acceleration; Re, Fr, Re* are dimensionless bulk Reynolds, Froude, roughness Reynolds numbers; q_b and C are respectively, the sediment volume transport rate per unit meter flume width and the flow cross-section averaged volume sediment concentration.

The ADVP technology as implemented in the present ACVP system was originally developed by [15] for multi-bistatic velocity profiling at turbulent flow scales.

The first sediment flux profiling system was proposed by [12] as the Acoustic Sediment Flux Profiler (ASFP) followed by the development of the Doppler Profiler (Dopbeam) by [13]. Both systems offered the first direct measurement of time-resolved sediment flux profiles at turbulent flow scales, with different piezo-electrical sensor setups, slightly different vertical resolutions (6mm for the ASFP, 6.9mm for the dopbeam), profiling ranges (40cm for the ASFP, 50cm for the dopbeam), similar temporal resolutions (1/25Hz), different acoustic intensity inversion methods (Least Mean Square compensation method for the ASFP and iterative implicit method for the dopbeam) and the same pulse-coherent Doppler velocimetry method (pulse-pair algorithm of [14]). The most important limitation of both systems concerned the measurable sediment concentration range. For the ASFP and dopbeam systems, a maximal volumetric sediment concentration of 10% and 20%, respectively, could be reached before particle scattering induced attenuation of the acoustic signal hindered reliable concentration estimation. This

limitation restricted the application of both instruments to suspended sediment transport studies. Nevertheless, this technology offered unprecedented possibilities in experimental sediment transport research both in fluvial flows and coastal ocean flows.

A considerably improved sediment flux profiling technology was developed by [7] as the Acoustic Concentration & Velocity Profiler (ACVP) technology. Compared to the original ASFP and dopbeam instruments, this system offered increased spatial (1.5mm) and

temporal resolutions (1/80Hz) allowing typically the resolution of the Taylor micro-scale in boundary layer open-channel flows with bulk Reynolds numbers up to $0(10^6)$. Furthermore, the instrument's multi-frequency performance was designed to transmit acoustic pulses between 500KHz and 5MHz. This capability allowed the most important measurement improvement compared to the original ASFP and dopbeam instruments, the vertical profiling across both the suspension and the dense bedload layer down to the undisturbed granular flow bed. This required the

development of a new dual-frequency inversion method [7] avoiding the data inversion instability encountered with the standard iterative implicit and explicit inversion methods [1]. Furthermore, the implementation of a novel Acoustic Bed Interface Tracking (ABIT) method [8, 9] in the ACVP system permitted for the first time, to decompose the measured total sediment transport rate (as the vertically integrated sediment flux profile) into bedload and suspended load transport rates. These unprecedented sediment transport rate measurement performances initiated the deployment of the ACVP technology in many fluvial and coastal sediment transport process studies.

3. Experimental setup & flow conditions

In the present study, sediment-laden open-channel flow experiments using low density (1192kg/m³) plexiglas (PMMA) particles with median diameters $d_p=1$ mm (dp1) and $d_p=3$ mm (dp3) were carried out in the LEGI tilting flume. The flume is 10m long, 0.35m wide and 0.5m deep.

Two types of experiments were carried out, the first type (first row in Table 1) corresponds to a full capacity

sediment transport flow over a thick (15cm) granular flow bed subject to erosion and transport by the overflowing water current. Only dp_3 sediments were used for this type of experiments. All other experiments in Table 1 (second to last row) use a standard conveyor belt injection of a sediment load falling into the water flow at 1m downwards the flume inlet. Details of the experimental protocols can be found in [4] and [10].

For all experiments, the flow regime was highly turbulent,

concentration $C=qs/Q$ where qs corresponds to the sediment rate injected by the conveyor belt.

4. Results

Figure 1 shows vertical profiles of mean flow quantities measured with the ACVP for the mobile bed experiments (first row in Table 1). Figure 1a and the panel below are pictures taken in these energetic sediment-laden open-channel flows. As expected, the sediment concentration is

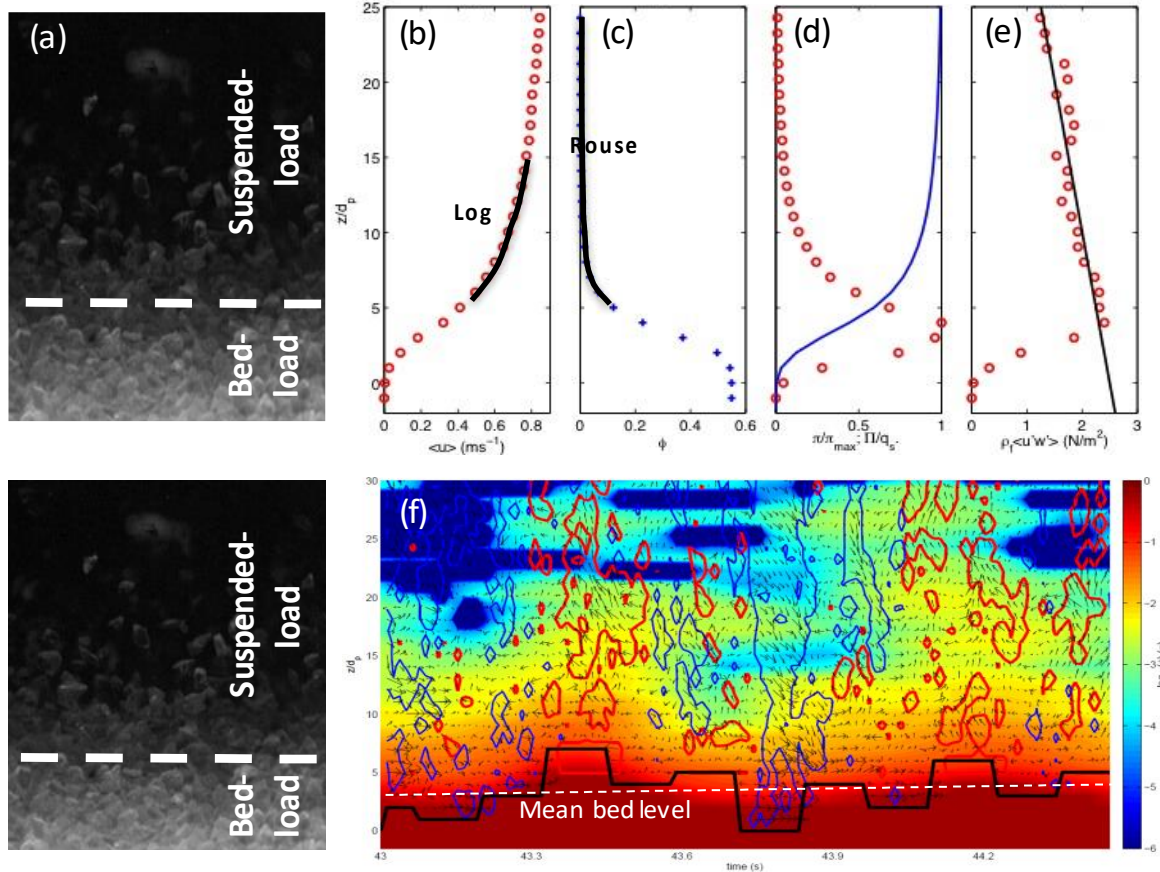


Figure 1: (a) Photograph of the sediment-laden open channel flow. ACVP measured vertical profiles of (b) mean streamwise velocity, (c) mean sediment concentration, (d) mean streamwise sediment flux, (e) mean Reynolds shear stress. Grey zones demarks the bedload layer. (f) Time-resolved sediment concentration colormap, 2C-xz turbulent velocity vector field and coherent flow structures as ejection- and sweep-type events. The black solid and white dashed curves represents the time-resolved and time-averaged flow

hydraulically rough and subcritical (Table 1). To assure the full development of the turbulent shear boundary layer, a honey comb at the flume inlet is used and the test section was placed 7m downwards the flume inlet.

The sediment-injected experiments (2nd to last row in Table 1) are performed in sequences of at least two runs, consisting of one clear-water flow for reference, followed by 1 to 3 sediment-laden flow runs, each with a duration of 300s, to guaranty low statistical bias of the measured mean flow quantities. Three flow conditions for each particle diameter were studied for the sediment-injected experiments. For each forcing condition, one clear-water and three solid transport conditions are investigated. This is repeated three times for experiment repeatability purposes. The full-capacity conditions were defined empirically, when a thin sediment layer was deposited over the flume's rigid bed. The two other transport conditions were fixed as a function of the mean sediment

seen to increase with vicinity to the granular flow bed. Figure 1b represents the vertical profile of mean horizontal velocity. The solid black curve reveals the presence of a logarithmic profile shape starting above the top of the bedload layer. Inside the bedload layer, the profile deviates strongly from a log profile and vanishes to zero over a height of about $5 dp$. The interface between the (dense) bedload layer and the above lying (dilute) suspension layer is defined at the height where the time-averaged sediment concentration profile (Figure 1c) is equal to 8%. Below this height the mean concentration increases rapidly until a fairly constant value around 55% which corresponds well to the typical value of a packed granular bed at rest. Furthermore, the position where this saturation value is reached corresponds well to the height where the flow velocity becomes negligibly low. The black solid curve in the suspension layer corresponds to a best-fitted Rouse profile supporting the turbulent mixing controlled transport of sediments in this layer. Figure 1d shows the

horizontal sediment flux as the time-averaged product of time-resolved velocity and sediment concentration profiles. It can be seen that a maximum in sediment flux is found inside the bedload layer. The blue curve in this Figure shows the cumulative transport towards the free-surface. It can be deduced that at the top of the bedload layer, more than 50% of the transported sediment load is reached revealing the dominant contribution of bedload transport for this flow condition (confirmed by the suspension number value $S=1.1$ in Table 1). Figure 1e represents the vertical profile of mean Reynolds shear stress as the relevant flow quantity for sediment transport. As expected under uniform steady open-channel flow conditions, the profile follows a linear trend with height (solid black curve) in the suspension layer. The maximum value is found inside the bedload layer below its top end. Inside the bedload layer, fluid Reynolds stress gradually decreases towards a zero-value reached at the non-moving granular flow bed. This supports the gradual transfer to grain stresses inside the granular rheology controlled bedload layer.

Time-resolved measurement performances of the ACVP technology is shown in Figure 1f. by the representation of the two-component (xz) turbulent velocity vector field $V'(u'w')$, the sediment concentration colormap and the turbulent coherent flow structures as ejection-type (red contours) and sweep-type (blue contours) flow eddies. Time averaged and time-resolved flow-bed position is represented by the dashed white and solid black lines. It can be seen that sediment entrainment into the suspension layer are associated with turbulent ejection-type flow structures and that bed erosion sequences are due to turbulent sweep-type events. The quality of these high-resolution ACVP measurements open new perspectives in the study of turbulent transport processes in energetic sediment-laden flows.

Figure 2 compares the ACVP measured sediment transport rate to the injected sediment load rate used a ground truth reference values in the sediment-injected experiments. Blue circle and black square symbols represent the dp3 and dp1 data, respectively. Mean relative error over the 27 different experiments are 4.7% and 10% for dp3 and dp1 experiments, respectively.

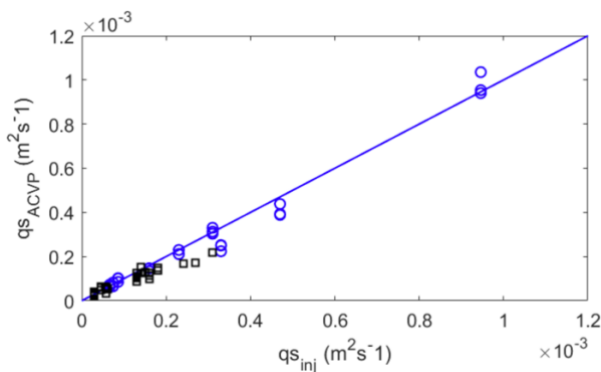


Figure 2: ACVP measured sediment transport flow rate versus flow injected sediment transport rate

5. Conclusion

ACVP profiling performance was shown for mean and time-resolved velocity, Reynolds shear stress, sediment concentration and sediment flux in energetic sediment-laden boundary layer flows generated in gravity-driven tilting flume experiments. Measurement accuracy in sediment transport flow rate was found to remain below 10% over a wide range of sediment-laden open-channel flow conditions. ACVP flow measurement technology offers new potential in process-oriented studies and modelling of sediment transport in highly turbulent flows.

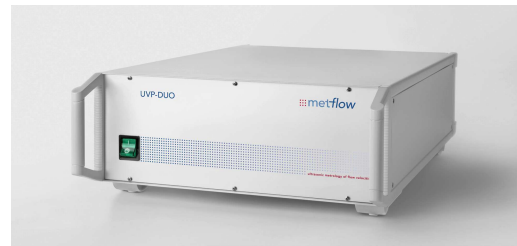
References

- [1] Thorne, P. D., & Hanes, D. M. (2002). A review of acoustic measurement of small-scale sediment processes. *Continental shelf research*.
- [2] Cellino, M., and W. H. Graf. (1999). Sediment-Laden Flow in Open-Channels under Noncapacity and Capacity Conditions. *J. Hydraul. Eng.*
- [3] Vanoni, V. A. E. J. 1946 Transportation of suspended sediment by running water. *Trans. Am. Soc. Civ. Eng.* 111, 67–133.
- [4] Revil-Baudard, T., Chauchat, J., Hurther, D. and Barraud, P.-A. (2015). Investigation of sheet-flow processes based on novel acoustic high-resolution velocity and concentration measurements. *Journal of Fluid Mechanics*.
- [5] Revil-Baudard, T., Chauchat, J., Hurther, D. and Eiff, O. (2016). Turbulence modifications induced by the bed mobility in intense sediment laden flows. *Journal of Fluid Mechanics*.
- [6] Cheng, Z., Hsu, T. J., & Chauchat, J. (2018). An Eulerian two-phase model for steady sheet flow using large-eddy simulation methodology. *Advances in Water Resources*.
- [7] Hurther, D., Thorne, P. D., Bricault, M., Lemmin, U., & Barnoud, J. M. (2011). A multi-frequency Acoustic Concentration and Velocity Profiler (ACVP) for boundary layer measurements of fine-scale flow and sediment transport processes. *Coastal Engineering*.
- [8] Hurther, D., & Thorne, P. D. (2011). Suspension and near-bed load sediment transport processes above a migrating, sand-rippled bed under shoaling waves. *Journal of Geophysical Research: Oceans*.
- [9] Fromant, G., Mieras, R. S., Revil-Baudard, T., Puleo, J. A., Hurther, D., & Chauchat, J. (2018). On Bedload and Suspended Load Measurement Performances in Sheet Flows Using Acoustic and Conductivity Profilers. *Journal of Geophysical Research: Earth Surface*.
- [10] Guta, H., Hurther, D., & Chauchat, J. (2022). Bedload and Concentration Effects on Turbulent Suspension Properties in Heavy Particle Sheet Flows. *Journal of Hydraulic Engineering*.
- [11] Thorne, P. D., and Hurther, D. (2014). An overview on the use of backscattered sound for measuring suspended particle size and concentration profiles in non-cohesive inorganic sediment transport studies. *Continental Shelf Research*.
- [12] Shen, C., & Lemmin, U. (1997). A two-dimensional acoustic sediment flux profiler. *Measurement Science and Technology*, 8(8), 880.
- [13] Zedel, L., & Hay, A. E. (1999). A coherent Doppler profiler for high-resolution particle velocimetry in the ocean: Laboratory measurements of turbulence and particle flux. *Journal of Atmospheric and Oceanic Technology*.
- [14] Lhermitte, R., & Serafin, R. (1984). Pulse-to-pulse coherent Doppler sonar signal processing techniques. *Journal of Atmospheric and Oceanic Technology*.
- [15] Lemmin, U., & Rolland, T. (1997). Acoustic velocity profiler for laboratory and field studies. *Journal of Hydraulic Engineering*.
- [16] Saugy J.-N., Amini A. and De Cesare G. (2022). Flow structure and grain motion assessments of large river widening in a physical model using ultrasonic Doppler velocity measurements, *Experiments in Fluids*.

metflow UVP-DUO-MX Ultrasonic Velocity Profiler

Main features of UVP-DUO

- High velocity, space and time resolutions
- Accuracy below 1%
- Stable performances over time
- Wide velocity, distance, time measuring ranges
- Control up to 20 transducers
- Remote-controlled by a standard PC via Ethernet
- Compact and sturdy design, low power consumption



UVP-DUO-MX

Main features of standard transducers TX line

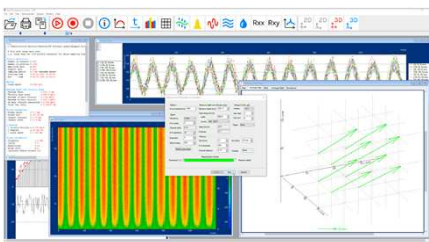
- High sensitivity
- Accurate acoustic signals generation for optimized spatial resolution
- High mechanical and pressure resistance
- Compact and sturdy stainless steel casing with precise finish
- Tough and low-loss shielded cable
- Robust cable attachment to the transducer body
- Robust standard BNC connector
- RoHS compliant



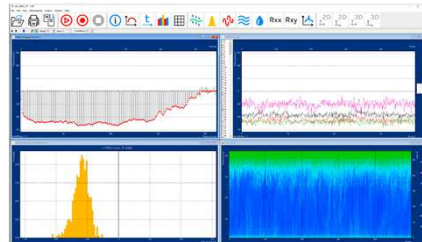
Standard transducers TX line
(8 / 4 / 2 / 1 / 0.5MHz)

Main features of UVP-DUO software

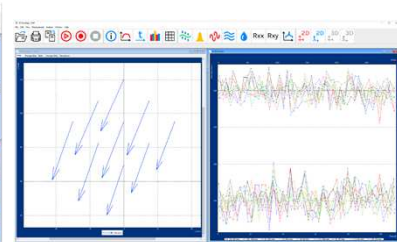
- Data acquisition and analysis in a single program, wide range of analysis tools
- Real-time 2D/3D flow mapping modules, on-line transducer grid editor
- Data export to: Clipboard, MS Word, Excel, Tecplot, MATLAB, with batch export function



New 3D displays of a
3D-3C UVP measurement



Velocity profile measurement of
a channel flow with gravel bed



2D Flow Map & Time series
of a channel flow

Application

- Measuring of velocity profiles in almost any liquid, either transparent or opaque : water, slurry, oil, food, liquid metal and more.
- For the academic and industrial research field of environmental hydraulics, hydraulics engineering, processes, liquid metals, fundamental fluid etc.

Manufacturer

metflow sa

Chemin Auguste-Pidou 8 - 1007 Lausanne,
Switzerland
www.met-flow.com

The exclusive agent in Japan



KYOKUTO BOEKI KAISHA, LTD.

Material Solutions Group
TEL : 03-3244-3703 E-mail : msg_sales01@kbk.co.jp
www.kbk.co.jp/en/

UVP-DUO の特徴

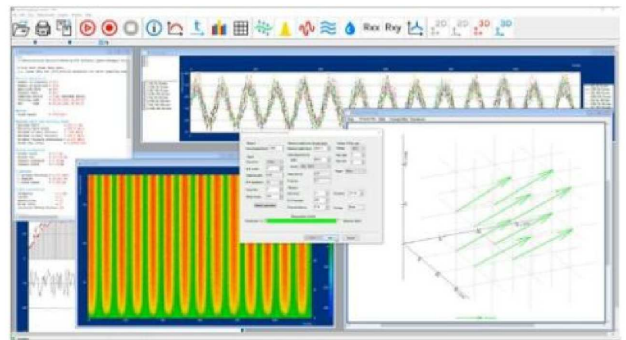
- ・ 液体が透明、不透明に関わらず、水、スラリー、油、食品、液体金属等、ほとんどの液体の流速分布を測定することが可能です。
- ・ 速度分布を測定し、リアルタイム表示が可能です。UVP 測定によって、直接的に流れを最適化したり、技術的な工程のフィードバックをオンラインで得ることが可能です。
- ・ 速度分布の時間軸から、乱流統計、空間相関、パワースペクトラム、ヒストグラム、伝達距離を計算することが可能です。
- ・ UVP-DUO を用いた測定は、様々な環境に使用可能な柔軟性があります。速度分布は、2 から 2048 までの測定点を設定することが可能で、幅広い速度範囲及び距離範囲に対応しています。
- ・ UVP ActiveX Library は、特注設計で取得したソフトウェアをプログラムする機能を有しています。復調したエコーにアクセスすることも可能です。

統合されたマルチプロセッサ

1本のトランスデューサーを用いた場合、そのトランスデューサー軸上の流速を測定することが可能です。非常に速い測定及びその評価のため、UVP-DUO-MX は、20本のトランスデューサーを同時に使用することが可能であり、ほとんどの流速測定において十分な解像度をもたらします。各トランスデューサーは、UVP-DUO-MX 本体裏側の BNC コネクタに接続します。

統合された流動場マッピング機能

複数本のトランスデューサーを、各トランスデューサー軸が交わる様グリッド上に配置することで、2次元流動場マッピング機能を使用することが可能です。トランスデューサー軸上の各々の投影から、それぞれの交点における2次元の速度ベクトルを、測定後表示することが出来ます。3D 測定についても、3つ目の速度成分及び同じ原理を用いることで、測定することが可能です。



UVP-DUO のユーザー

正確な流速分布の測定に興味がある、学術分野及び産業分野の研究者及び科学者に UVP-DUO が用いられています。主に以下のような研究分野で使用されています。

- ・ 環境水理学：堆積物、河川、波、排水の流れ
- ・ 水理工学：建築、輸送
- ・ 工程：食品、化粧品、紙、油、炭鉱、化学などの産業分野
- ・ 液体金属：冶金、地学、化学反応など
- ・ 基礎的な流体力学：乱流、磁場の流れ、対流

(お問合せは)

極東貿易株式会社

マテリアルソリューショングループ

TEL : 03-3244-3703

E-mail : msg_sales01@kbk.co.jp

www.kbk.co.jp

UBERTONE

Ultrasonic measurement in liquids
Monostatic and bistatic acoustic profilers for the lab and the field



Environmental Monitoring & Study

- accurate flow rate measurement
- sediment transport studies (SSC)
- open channel flow characterisation
- sewer network diagnosis



Scientific Research

- accurate velocity field acquisition
- hydraulic model instrumentation
- turbulence measurements
- fluid mechanics investigation



Industrial Process Control & Optimisation

- in-line measurement and quality control
- batch mixing optimisation
- CRD input and validation
- pump and turbine optimisation



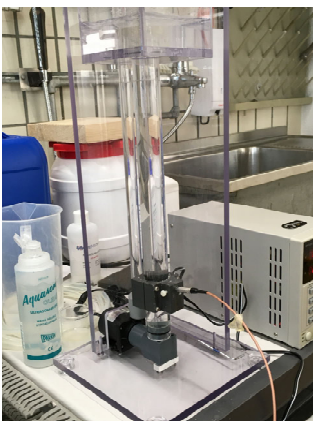
www.ubertone.com
UBERTONE SAS, FRANCE



FlowBiz

since 1998

Preparing for eUVP



Contact : kt@flowbiz.jp

Ultra high power & Multi-waves

Ultrasonic Pulser & Receiver

Rich features and good operability



JPR-600C
(Standard model)



NEW

JPR-50SD
(High Freq. & Compact)



JPR-10C-8CH
(8 Channels)



MUX-64
(64ch Multiplexer)

Pulser & Receiver for single / multi channel with PC Control
Optimum & powerful burst wave mode

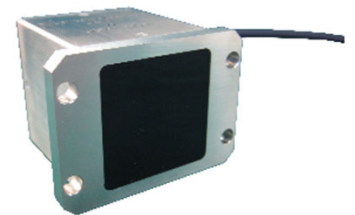
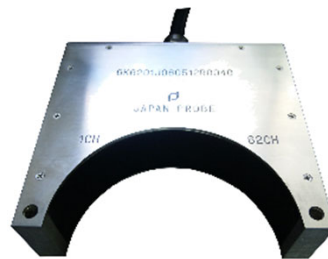
User-customizable

Ultrasonic Probe / Ultrasonic Array Probe

We manufacture variable transducers as you request



Single
Immersion Probe



Array Probe
1D Linear Elements / 1D Concave Elements / 2D Matrix Elements

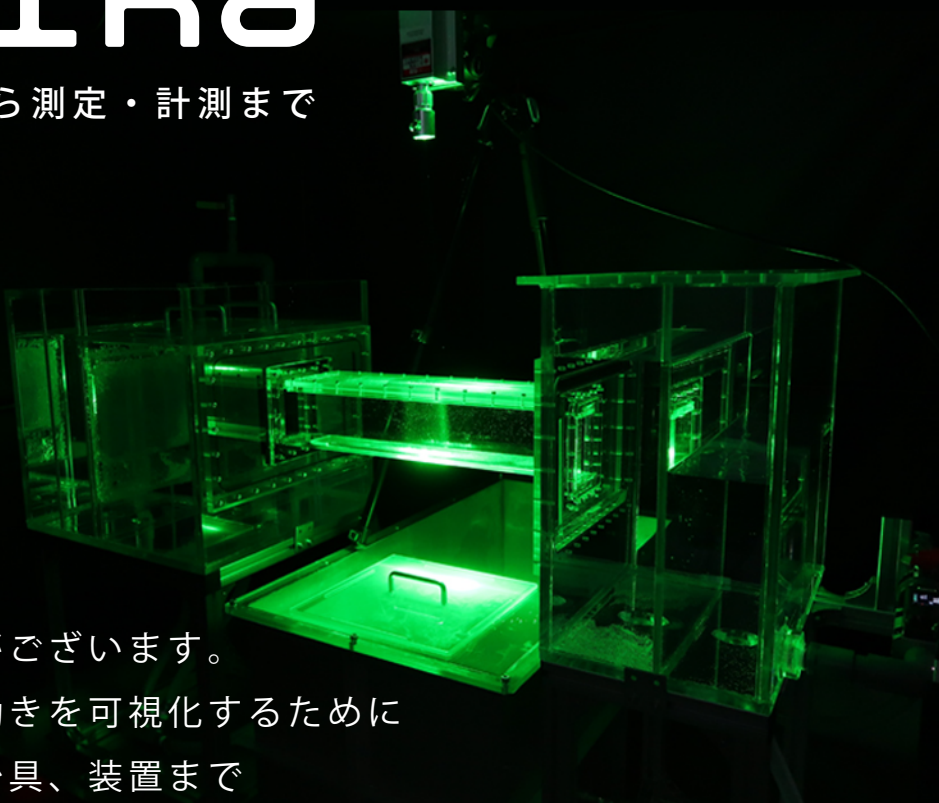
We use our extensive know-how to manufacture the optimum probes
Please ask us the specification of probe you want



KASHIKA

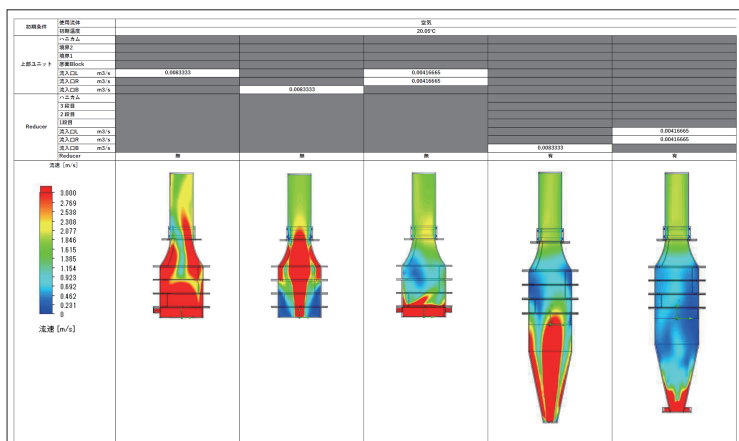
可視化部品・装置の製作から測定・計測まで

当社には年間 200 件以上の
透明可視化に関するご依頼がございます。
目に見えない気流・水流の動きを可視化するために
必要な加工品から、器具・治具、装置まで
ご提供いたします。



循環水槽 PIV デモ撮影の様子

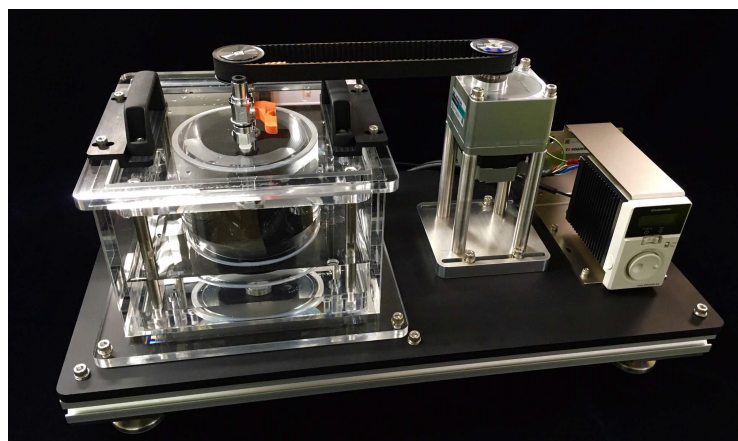
熱流体解析



液体やガスの流れが与える影響を設計段階でご提案することが可能です。

試作前に課題を診断する事で、設計や工程の検討(最適化)を行う事ができます。設計や製作後の手戻りが削減でき、開発期間の短縮に繋がります。

透明可視化支援



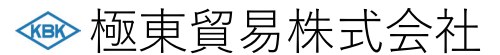
特注で可視化部品が欲しい、測定・計測できる形状を相談したいなど、お客様に必要な可視化研究を様々な角度からご支援させていただいております。水、オイル、空気など可視化したい内容に合わせた部品の製作から周辺機器の設計、データ集計まで幅広くご対応いたします。

HPのお問合せフォーム、お電話等でお気軽にお問合せ下さい





SPONSORS



SUPPORT

OFFICIAL TRAVEL GUIDE OF
— KOBE —

